AERODYNAMIC ANALYSIS OF FLAPPING WING ACTUATED WITH PZT MATERIAL INCLUDING AEROELASTIC DEFORMATION

A THESIS SUBMITTED TO
THE GRADUATE SCHOOL OF NATURAL AND APPLIED SCIENCES
OF
MIDDLE EAST TECHNICAL UNIVERSITY

BY

FADILE YUDUM COMEZ OZGUN

IN PARTIAL FULFILLMENT OF THE REQUIREMENTS
FOR
THE DEGREE OF DOCTOR OF PHILOSOPHY
IN
AEROSPACE ENGINEERING

JANUARY 2024

Approval of the thesis:

AERODYNAMIC ANALYSIS OF FLAPPING WING ACTUATED WITH PZT MATERIAL INCLUDING AEROELASTIC DEFORMATION

submitted by **FADİLE YUDUM ÇÖMEZ ÖZGÜN** in partial fulfillment of the requirements for the degree of **Doctor of Philosophy in Aerospace Engineering, Middle East Technical University** by,

Prof. Dr. Halil Kalıpçılar
Dean, Graduate School of **Natural and Applied Sciences** _________________

Prof. Dr. Serkan Özgen
Head of the Department, **Aerospace Engineering, METU** _________________

Prof. Dr. Dilek Funda Kurtuluş
Supervisor, **Aerospace Engineering, METU** _________________

Prof. Dr. Nevsan Sengil
Co-Supervisor, **Aerospace Engineering, THKU** _________________

Examining Committee Members:

Prof. Dr. Altan Kayran
Aerospace Engineering, METU _________________

Prof. Dr. Dilek Funda Kurtuluş
Aerospace Engineering, METU _________________

Prof. Dr. M. Haluk Aksel
Aeronautical Engineering, THKU _________________

Assoc. Prof. Dr. Ali Emre Turgut
Mechanical Engineering, METU _________________

Asst. Prof. Dr. Kutluk Bilge Arıkan
Mechanical Engineering, TEDU _________________

Date:15.01.2024

I hereby declare that all information in this document has been obtained and presented in accordance with academic rules and ethical conduct. I also declare that, as required by these rules and conduct, I have fully cited and referenced all material and results that are not original to this work.

Name, Last name: Fadile Yudum, Çömez Özgün

Signature:

ABSTRACT

AERODYNAMIC ANALYSIS OF FLAPPING WING ACTUATED WITH PZT MATERIAL INCLUDING AEROELASTIC DEFORMATION

Çömez Özgün, Fadile Yudum
Doctor of Philosophy, Aerospace Engineering
Supervisor: Prof. Dr. Dilek Funda Kurtuluş
Co-Supervisor: Prof. Dr. Nevsan Şengil

January 2024, 150 pages

In this thesis, both experimental and computational methods are proposed as a solution to understand how aerodynamic forces and structural deformations of flexible flapping wings interact utilizing unsteady conditions. In the first part of the experiments, the structural properties (e.g., Young’s modulus, Poisson’s ratio, density) of the wing material are investigated and the wing models are fabricated from thin aluminum material. To conduct the experiments, one flexible rectangular wing and one Rufous hummingbird wing are selected. These wings are manufactured from a flat aluminum plate without replicating the vasculature structure found in flying creatures of nature. Throughout these experiments, the wings are induced to flapping motion using piezoelectric actuators. Force measurements are obtained by the ATI Nano 17 force/torque sensor and the wing deformations are collected by the DIC high-speed camera system. The displacement values obtained from the Digital Image Correlation (DIC) system provided inputs to the numerical model. The simulations of the laminar flow conditions at low Reynolds numbers are conducted using Ansys Fluent software. Consequently, the impact of deformations captured by the high-speed camera system on the wing's flow is observed. Thus, the effect of structural deformations on the flow is observed, and their impacts on the flow due to structural deformations are determined. The combined use of experimental and numerical methods was facilitated rather than employing lengthy and intricate analysis methods.

Keywords: Butterfly Flapping Wings, PZT Material, Aeroelastic Analysis, Experimental Methods, Computational Methods.

ÖZ

PZT MALZEME İLE HAREKETE GEÇİRİLEN ÇIRPAN KANADIN AEROELASTİK DEFORMASYONLU AERODİNAMİK ANALİZİ

Çömez Özgün, Fadile Yudum
Doktora, Havacılık ve Uzay Mühendisliği
Tez Yöneticisi: Prof. Dr. Dilek Funda Kurtuluş
Ortak Tez Yöneticisi: Prof. Dr. Nevsan Şengil

Ocak 2024, 150 sayfa

Bu tezde, aerodinamik kuvvetlerin ve esnek çırpan kanatların yapısal deformasyonlarının kararsız koşullar altında nasıl etkileşime girdiğini anlamak için hem deneysel hem de hesaplamalı yöntemler bir çözüm olarak önerilmektedir. Deneylerin ilk bölümünde kanat malzemesinin yapısal özellikleri (Young modülü, Poisson oranı, yoğunluk gibi) araştırılmış ve kanat modelleri ince alüminyum malzemeden üretilmiştir. Deneyleri gerçekleştirmek için bir adet esnek dikdörtgen kanat ve bir adet Kızıl sinekkuşu kanadı seçildi. Bu kanatlar, doğadaki uçan canlılarda bulunan damar yapısı taklit edilmeden, düz bir alüminyum plakadan üretilmektedir. Bu deneyler boyunca kanatlar, piezoelektrik tetikleyiciler kullanılarak kanat çırpma hareketi verilerek tetiklenmektedir. Kuvvet ölçümleri ATI Nano 17 kuvvet/tork sensörü ile ölçülmektedir ve kanat deformasyonları DIC yüksek hızlı kamera sistemi ile toplanmaktadır. Dijital Görüntü Korelasyonu (DIC) sisteminden elde edilen yer değiştirme değerleri sayısal modele girdi sağlamıştır.

Düşük Reynolds sayılarında laminer akış koşullarının simülasyonları Ansys Fluent yazılımı kullanılarak gerçekleştirilir. Sonuç olarak, yüksek hızlı kamera sistemi

tarafından yakalanan deformasyonların kanat akışı üzerindeki etkisi gözlemlenmektedir. Böylece yapısal deformasyonların akış üzerindeki etkisi gözlemlenir ve yapısal deformasyonlardan dolayı akışa etkileri belirlenir. Uzun ve karmaşık analiz tekniklerinin kullanılması yerine deneysel ve sayısal yöntemlerin bir arada kullanılması araştırmayı kolaylaştırmıştır.

Anahtar Kelimeler: Kelebek Kanadı, Çırpan Kanat, Aeroelastik Analiz, Piezoelektrik Malzeme, Deneysel Yöntemler, Bilgisayar Tabanlı Yöntemler.

To my dearest parents Güler and Vedat Çömez, and my love Muharrem Özgün…

ACKNOWLEDGMENTS

I would like to express my deep and sincere gratitude to my supervisor Prof. Dr. D. Funda Kurtuluş, whose kindness, patience, academic experience, and knowledge are invaluable to me at all steps of this thesis study. Without her enthusiasm, energy, and support, I would not have completed this study. I am truly honored and fortunate to have had the privilege of working under her supervision.

I am deeply grateful to my co-supervisor Prof. Dr. Nevsan Şengil for his invaluable guidance, unwavering support, and scholarly insights throughout the entire journey of completing this thesis.

I would like to thank my thesis advisory committee members Prof. Dr. Altan Kayran and Assoc. Prof. Dr. Ali Emre Turgut for their contributions during semiannual meetings. Their dedication, expertise, and constructive feedback significantly contributed to shaping the direction and quality of this work. I am thankful for their mentorship, and continuous encouragement, which played a pivotal role in enhancing the depth and rigor of this research.

I want to express my eternal gratitude to my husband Muharrem and my parents. Their boundless love, endless encouragement, and sacrifices have been the cornerstones of my success. Their unwavering support and belief in my dreams have inspired and motivated me to overcome challenges and pursue my academic aspirations. Their love and support have been the guiding light that has enabled me to reach this significant milestone in my life, and for that, I am forever thankful.

I express my gratitude to the METU Center for Wind Energy (METUWind, RÜZGEM) for facilitating the utilization of experimental tools. Special thanks are extended to Prof. Dr. Oğuz Uzol, the director of RÜZGEM, for his invaluable support in conducting various experiments and projects.

This work is partially funded by the Scientific and Technological Research Council of Turkey under grant number TUBİTAK 116M273.

Computing resources used in this work are partially provided by the National Center for High-Performance Computing of Turkey (UHeM) under grant number 4011792022.

ATATÜRK'ÜN GENÇLİĞE HİTABESİ

"Ey Türk gençliği! Birinci vazifen; Türk istiklalini, Türk cumhuriyetini, ilelebet muhafaza ve müdafaa etmektir.

Mevcudiyetinin ve istikbalinin yegâne temeli budur. Bu temel, senin en kıymetli hazinendir. İstikbalde dahi seni bu hazineden mahrum etmek isteyecek dâhilî ve haricî bedhahların olacaktır. Bir gün, istiklal ve cumhuriyeti müdafaa mecburiyetine düşersen, vazifeye atılmak için içinde bulunacağın vaziyetin imkân ve şeraitini düşünmeyeceksin. Bu imkân ve şerait, çok namüsait bir mahiyette tezahür edebilir. İstiklal ve cumhuriyetine kastedecek düşmanlar, bütün dünyada emsali görülmemiş bir galibiyetin mümessili olabilirler. Cebren ve hile ile aziz vatanın bütün kaleleri zapt edilmiş, bütün tersanelerine girilmiş, bütün orduları dağıtılmış ve memleketin her köşesi bilfiil işgal edilmiş olabilir. Bütün bu şeraitten daha elim ve daha vahim olmak üzere, memleketin dâhilinde iktidara sahip olanlar, gaflet ve dalalet ve hatta hıyanet içinde bulunabilirler. Hatta bu iktidar sahipleri, şahsi menfaatlerini müstevlilerin siyasi emelleriyle tevhit edebilirler. Millet, fakruzaruret içinde harap ve bitap düşmüş olabilir.

Ey Türk istikbalinin evladı! İşte, bu ahval ve şerait içinde dahi vazifen, Türk istiklal ve cumhuriyetini kurtarmaktır. Muhtaç olduğun kudret, damarlarındaki asil kanda mevcuttur."

Mustafa Kemal Atatürk

20 Ekim 1927

TABLE OF CONTENTS

LIST OF TABLES

TABLES

LIST OF FIGURES

FIGURES

LIST OF ABBREVIATIONS

ABBREVIATIONS

3D	Three Dimensional
AOA	Angle of Attack
CFD	Computational Fluid Dynamics
DIC	Digital Image Correlation
DOF	Degrees of Freedom
FEM	Finite Element Method
FOV	Field of View
FWMAV	Flapping Wing Micro Air Vehicle
MAV	Micro Air Vehicle
NS	Navier Stokes
PIV	Particle Image Velocimetry
RMS	Root Mean Square
RANS	Reynolds Averaged Navier-Stokes Equation
SIMPLE	Semi-Implicit Method for Pressure-Linked Equations
UDF	User-Defined Function

LIST OF SYMBOLS

Symbols

c	Chord length
C_D	Drag coefficient
C_L	Lift coefficient
C_p	Pressure coefficient
P	Pressure
q	Dynamic pressure
R	Length
Re	Reynolds number
S	Area
t	Time
Δt	Time step
i, j, k	Cartesian coordinates
u, v, w	Velocity components
$x, y; z$	Spatial Cartesian coordinates
U	Velocity
V	Volume
ɵ	Flap angle
μ	Dynamic viscosity
ρ	Density
ω	Angular velocity of flapping wing motion
θ	Flapping angle in radian

Subscripts

∞	Free-stream values
tip	Wing-tip

CHAPTER 1

INTRODUCTION

1.1 Background of Study

Last three decades unmanned aerial vehicles (UAVs) have attracted researchers' attention due to their capabilities in high-risk environments. Therefore, there is no requirement for pilot control on the vehicle for operation or safety risks. Over recent years, widespread usage of UAVs has occurred in military and civilian sectors. Unmanned micro air vehicles (MAVs) with smaller sizes, robust materials, and lower prices of electronic devices substitute the high cost of the vehicles. The first known MAV definition was given by the Defense Advanced Research Projects Agency (DARPA) in the late 90's. The vehicle has dimensions less than 15 cm (6 inches), a maximum takeoff weight limit that does not exceed 100 grams, and a flight endurance of 60 minutes. This size definition refers to a category of vehicle that is at least ten times smaller than any missionized UAV created thus far.

Figure 1.1 shows a class of both natural and man-made flying vehicles schematically depicted in terms of their mass and size versus Reynolds number. The novelties of MAVs are relatively inexpensive when compared with traditional vehicles in terms of manufacturing and operating them during several mission roles. At MAVs' flow regime, lift producing is inherently unsteady and vortex-dominated. Flapping flight is considerably understood, and general limits, advantages, and disadvantages of unsteady mechanisms are identified.

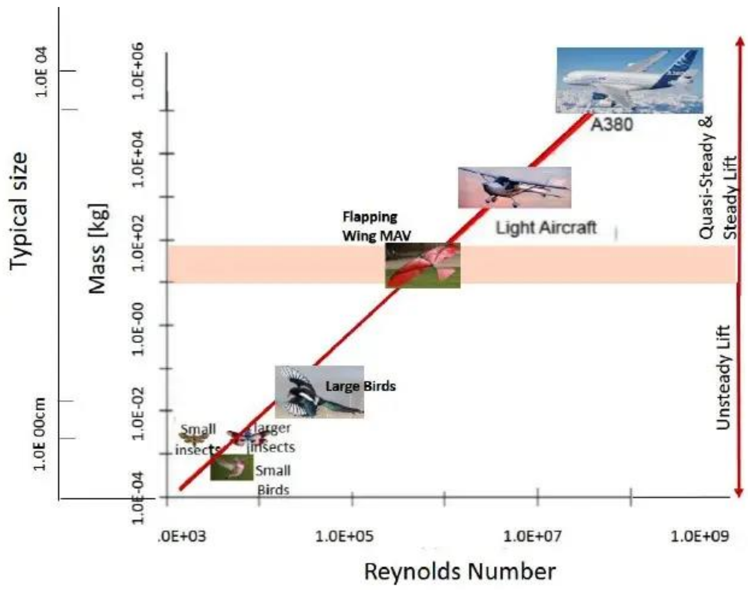

Figure 1.1 The systematic design of MAV in the order of scale as fliers [1].

There are three generations of MAVs: Fixed-wing, rotating wings (like helicopters) and micro technology (MEMS, flapping or vibrating wings). As a first type of MAVs, the fixed wings typically have very few moving parts to achieve appropriate flight conditions, and that is their primary benefit. In addition, fixed-wing MAVs are prone to produce more efficient aerodynamic characteristics when other configurations are compared to them. In contrast, a fixed-wing MAV has less sustainability characteristics towards forward speed to keep in flight. Also, this configuration is not capable of hovering. The second member of small, unmanned aircraft systems (sUAS) is rotary wings. The wings are created lift by constant rotation of surfaces. Their designs allow them to hover flight and sustainability of control at low forward speeds. Rotary-wing MAVs are typically more maneuverable than fixed-wing designs. On the other hand, the only drawback is lower efficiency regarding the generation of lift force. The rotary wings have subcategories. They can be exemplified as single-rotor, coaxial-rotor, and multi-rotor designs.

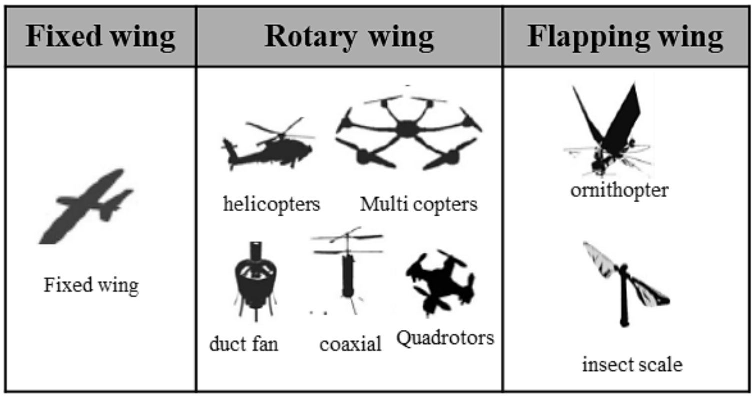

Figure 1.2 Classification of air vehicles.

Thirdly, flapping flight imitates a mode of transport motion widely adopted by natural fliers, and several unique characteristics have been captured by biologists and engineers. Hence, the flapping flight can be evaluated as an alternative flight type due to its requiring less energy consumption compared to traditional aircraft propulsion. In addition, the maneuverability and controllability of flapping wing vehicles are able to show notable flying capabilities even with constraints on cruise way. Wing kinematics, the interaction between structural response and fluid around the wing, power consumption, and aerodynamics of flapping flights are worth exploring. Particularly the interaction of the flapping adjoint parts (tails, body, fore-hinge wings, body e.g.) with the surrounding air leads to the generation of vortices and these vortices can improve flight performance.

1.2 Literature Survey

In the last two decades, micro air vehicle (MAV) studies have been accelerated to understand the unsteady dynamics of both natural fliers and ornithopters at low Reynolds. Although the complex flight kinematics of these fliers require broad investigation due to efficiency factors, there are some stunning studies on hovering and forward flights of MAVs.

In-depth investigations into Micro Air Vehicles (MAVs) have been carried out by the Aerospace Engineering Department at METU through previous experimental and numerical studies on symmetric airfoils at low Reynolds numbers [52]-[60]. Additionally, the department has explored various 3D wing models in the realm of bioinspired flapping wings, particularly at low Reynolds numbers [61]-[63].

This thesis is inspired by natural flyers and their wing shapes, materials, and secrets of aerodynamics. Additional investigations are required about interconnected analyses, namely, aerodynamic forces and structural deformations. Examples consist of clap-and-fling motion, leading-edge vortex (LEV) structures, rotational lift generation, wake capture, wing-wing interactions, body-wing interactions, and wing-fluid interactions.

1.2.1 Bioinspired Wings and Related Studies

Bioinspired studies can be divided into several categories and there are primary features to consider when making this distinction. The lightweight, small size and propulsion efficiency are some key points that should be worth reckoning with their effects. Some effective models have already existed. These models can be classified as the following sub-sections:

Motor-driven insect-inspired FW-MAVs with tails capable of free-controlled flight:

In Figure 1.3, a Smart Bird study is revealed in 2012 by Send et al.[2] A complete (twin wing, body, and tail) ornithopter with a 2 m span, 0.5 m^2 planform area, 0.25 m mean chord length, and 0.48 kg weight including the battery is introduced in the study. The system operated at 5 m/s speed, 2 Hz flapping frequency, and 23 W average energy consumption. The bird is capable of active torsion periodically actuated by a servo motor and a combination of flapping motion generates partially linear forward flight. Also, the flapping drive leads to bending mode to generate lift.

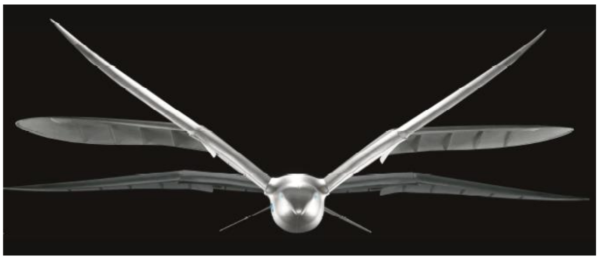

Figure 1.3 Smart Bird [2].

In Figure 1.4 Robo Raven V from [3] is shown during untethered forward flight. Robo Raven V is developed as the last model after a set of optimizations on it. The most worthwhile contribution is to the investigation of flapping frequency limit determination under aeroelastic effects. Flexible wing mammalian model insect size Robo Raven V is a propeller added MAV, especially can fly outdoors with low airspeeds, thus, flapping, and propulsive modes can increase both lift (payload capacity) and thrust of the vehicle during operating at outdoor places. The ascent values are possible only for the most optimal propeller positions on MAV.

Figure 1.4 Robo Raven V [3].

Figure 1.5 A 3.2 g flapping-wing platform from Harvard University (left) [4] and H2Bird ornithopter from the University of California, Berkeley (right) [5].

An untethered vehicle weighing 3.2g, designed for both active (flapping) and passive (gliding) flight, has been developed and validated for conducting energetics studies. The development and validation of a lightweight flapping wing vehicle for conducting energetics studies has been carried out. Modulation of the duty cycle for various flight experiments can be easily achieved by robots. Movement data from integrated sensors is successfully collected and wirelessly streamed by the robot.

Furthermore, plans include the addition of actuated control surfaces to the tail, along with the capability to adjust the tail angle during flight. This will grant the ability to perform more complex maneuvers and stabilize the vehicle. There is also a prospect of implementing a split-wing design, allowing independent flapping of the wings to achieve greater control authority [4].

A comparison between the predicted behavior of an ornithopter based on a wind tunnel dataset and the measured free-flight equilibrium conditions has been conducted. The robotic platform employed for this purpose is the H2Bird, recognized as a flapping-winged Micro Air Vehicle (MAV). Featuring a custom-built structure made of carbon fiber, the H2Bird is equipped with clap-fling wings and a reinforced tail, utilizing the Silverlit i-Bird RC flier power train. Its wingspan measures 26.5 cm, and it weighs 13.6 grams. Yaw and pitch control are facilitated through a servo-controlled elevator and a tail-mounted propeller, respectively. For control and sensing functions, the H2Bird relies on an onboard ImageProc 2.42 controller housing a 40 MIPS microprocessor, a 6 Degree of Freedom Inertial Measurement Unit (IMU), an IEEE 802.15.4 radio, and motor drivers. These systems are powered by a 90 mAh lithium polymer battery.

Motor-driven insect-inspired tailless FW-MAVs capable of free controlled flight:

As an example, the tailless flapping wing robot with a low aspect ratio is proposed as in butterfly-inspired shape by Chi et al. [6]. The lightweight design is supported by thin membrane material for wings, ultra-high-modulus carbon rods as stiffeners, and light micro servo motors for actuation. The study is also contributed with computational fluid dynamics software. The tailless butterfly-type flapping wing aircraft has a low aspect ratio, and it operates based on the natural butterfly frequency limit. Two actuators directly control the wing stroke amplitude, which changes in the range of +70º to -30º during forward flight. Total weight of MAV is 38.6 g and of wingspan is 64.8 cm. The butterfly is operating at 2Hz frequency which corresponds to 1.5m/s flight speed. During the study, both rigid and flexible wing butterflies are simulated as computational domains, and the deformation of flexible wings shows an important development in lift generation.

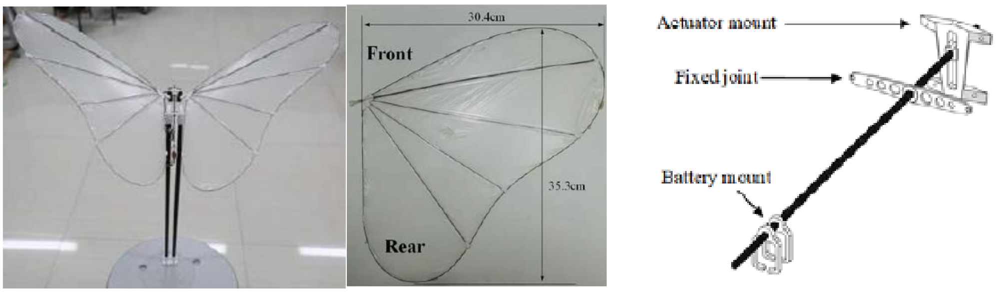

Figure 1.6 Butterfly-type Ornithopter was developed by Beihang University [6].

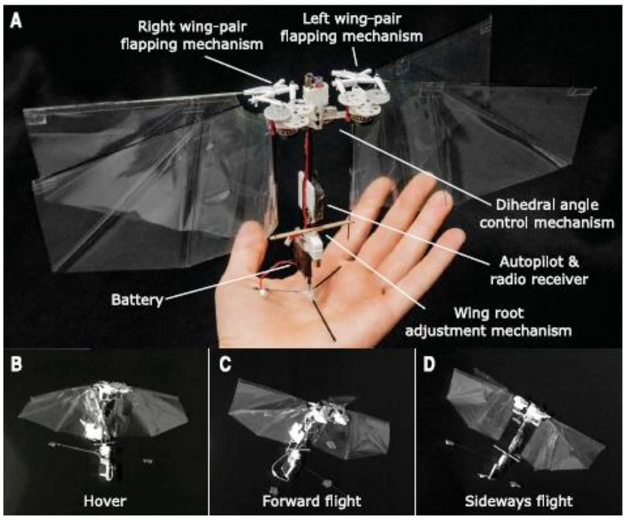

Figure 1.7 An insect-inspired free-flying robotic platform is controlled through its two pairs of independently flapping wings. (A) The robot's components. High-speed camera frames capture the robot in hover (B), forward flight (C), and sideways flight (D) [7].

A programable fruit fly vehicle is magnified as 55 times real insect size and has an agile autonomous free-flying controlled by motion changes of its flapping wings. The fruit fly robot has the capability of the rapid escape maneuvers of fliers including yawing rotations, pitching control with torque, and flapping motions. When the yaw control of the flier is turned off, there is an aerodynamic coupling between the yaw torque and the roll and pitch torques produced throughout the maneuver. In Figure 1.7 [7], high-speed camera images are captured to see hovering, forward flight, and sideway flights. A detailed CAD drawing is given in Figure 1.8 the motion control mechanisms can be seen.

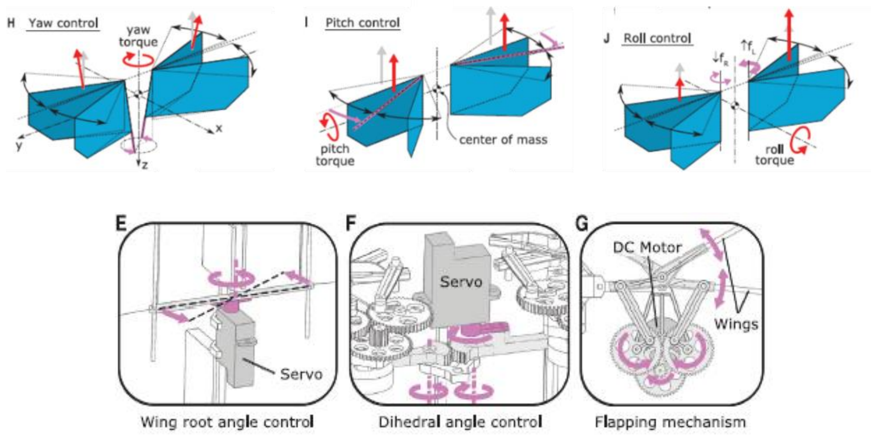

Figure 1.8 Wing motions are controlled by servo and DC motors [7].

The weight is one of the trickiest issues about MAVs. Therefore, researchers seek many different actuation systems that can create reusable energy sources and allow untether motion for independent motion.

Examples of insect-inspired FWAVs driven by piezoelectric actuators:

Electromagnetic motors and piezoelectric actuators are top-ranking actuation sources to alleviate weights pulling down below the level of the gram in flapping-wing micro air vehicles (FWMAVs). One of the piezoelectric actuators driven dual wings honeybee-sized insect scale with flapping motion is studied by James et al. [8]. The flapper is only 190 mg as a whole system. To take off the flapping vehicle, a laser source is placed on top of the system, which triggers the system and results in a source wirelessly to the vehicle actuation. This solar cell provides a one-way conversation between optical power and electrical power. The power obtained from the laser trigger is finally used to run the microcontroller which produces sinusoidal voltage outputs. Thus, two piezo-electric actuators, which induce flapping control, can convert the electrical inputs to mechanical motion. The microcontroller to flap is programmed with a single driver circuit and the continuous maximum flap amplitude is reached at 170 Hz frequency value to create the maximum lift. Early experiments are performed with a 130 mg dummy load and the system is driven by a 190 $V_{p\text{-}p}$ sinusoidal voltage. The altitude of the flight will remain in future experiments and tethered flight is preferred at this level. The breakthrough is shown in successive takeoffs without wire.

Figure 1.9 Full insect scale robotic fly placed on a US penny for scale [8].

Ozaki et al. [9] study the tethered flight of direct-driven wings by using unimorph piezoelectric actuators. The two-wing prototype is powered by an external power source and lifted off with a 1 DOF constraint. The total wingspan is 114 mm, and the total mass of the prototype is 598 mg. At 100 V operating voltage, the lift force is measured as 665 mgf. In direct-driven piezoelectric actuators, one of the major problems is their small displacement production under the piezoelectric effect. Therefore, for flapping wing micro air vehicle systems mostly propose different lever mechanisms with optional materials and structures to amplify the displacements. In this study, the system consists of a wing actuated by a trapezoidal piezoelectric unimorph actuator. To feed the lift force generation, the wing materials are cautiously specified, which is constituted by Ti at the leading edge, Ti/polyimide (PI) at veins, and polyester at the surfaces. The unimorph piezoelectric actuators are driven by a cyclic voltage at the resonant frequency which generates large stroke amplitude and due to the stroke motion pitching motion passively occurs via the air pressure around the wing and inertial forces of the wing. During experimental measurements, an electric balance is used for average lift force data and a camera simultaneously records the motion of the tethered system. Thus, the stroke angle can be captured to this end. By combining measured the frequency responses of the stroke amplitude and lift forces are used to determine the resonant frequency of the wings. The maximum stroke and pitch angles are investigated as 25.9° and 66.2°, respectively.

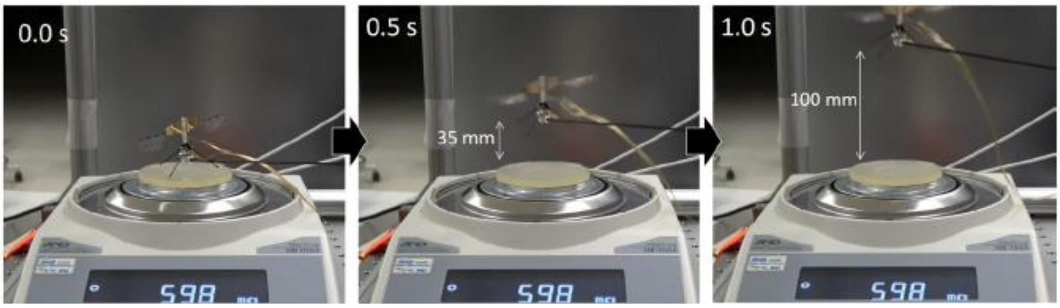

Figure 1.10 Frames captured during takeoff of a two-wing robot (V_{pp} = 90 V) [9].

The bio-inspired flapping wing imitates a drone fly Eristalis tenax [10]. The bioinspired robot has four-bar systems with flexible hinges designed to serve as the transmission. The wing consists of veins that are built from 60 μm thickness carbon fiber due to its intrinsic high modulus and lightweight. Thus, the system weighs 84 mg, and the wingspan is 35 mm. The resonant frequency to take off is 100 Hz generating sufficient thrust with an approximate ±60° flapping angle. The passive rotation is derived from the inertia and the aerodynamic forces by a flexible hinge at the wing root thereby generating lift. The first take-off is one degree of freedom constraint by supporting a pair of vertical guide rails. During experiments tip displacement is measured by a laser displacement sensor and the resonant frequency of the actuator is determined as measured the peak-to-peak value of the driving signal is set to 250 V under 100 Hz sweep-frequency. The experiment succeeded around ∼100 Hz the resonant frequency with a flapping amplitude of approximately ±60° and ±380 μm vibration amplitude.

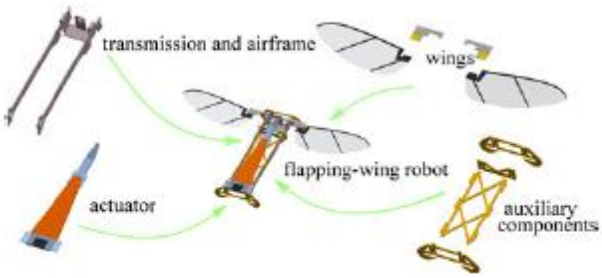

Figure 1.11 CAD model of the whole robot and all its components [10].

Examples of insect-inspired FWAVs driven by electromagnetic actuators:

Compared with piezoelectric actuators, the following actuator type is an unusual driving scheme example provided by much lower operation voltage for the insect scale FMAVs. Instead of generating rotary motions with motor-driven systems, piezoelectric actuators produce vibratory motions and transform this vibration into artificial flapping wings with simple structures such as cantilevers or directly driven wings. However, these systems have some drawbacks to high operation voltages, the vibratory electromagnetic actuator provides feasible low voltage and simple structure to drive the insect scale FMAVs.

Liu et al. [11] present a new type of vibratory electromagnetic actuator with a low voltage of 5.5 V. The actuator can generate potential flapping motion for insect scale artificial wings FMAVs. To identify the resonant frequency and amplitude of the dynamic system, the experimental setup is produced, in addition, a simplified lumped mass model is proposed to analyze the magnetic Lorentz force. In the prototype designs and tests with long cantilever beam structure, small magnets, and larger magnets (Figure 1.12). Furthermore, from studies low-voltage electromagnetic actuators could broaden the driving mechanisms for insect scale FMAVs.

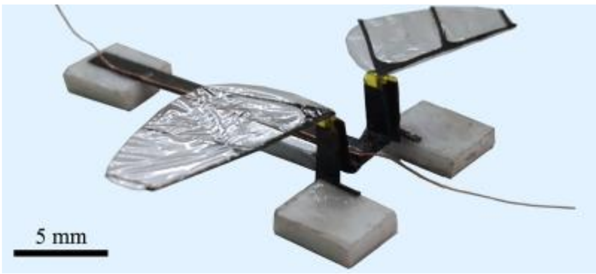

Figure 1.12 The prototype uses a cantilever plate with a transmission mechanism to drive a pair of artificial wings [11].

This study is investigated by Zou et al. [12] differently interpreted from the version of the laser-triggered piezoelectric actuation bio-inspired flapper which is depicted in Ref. [10]. The research group investigates an electromagnetic actuation system via the same self-lifting, sub-100-mg, insect-inspired flapping-wing micro aerial vehicle. This electromagnetic actuator system is able to lift off by controlling the flapping amplitude and creating passive wing rotation. Flapping motion and passive rotation motion result in two degrees of freedom systems on flapping wing micro air vehicles. A planar four-bar system is in charge of flapping motion and the wing rotations result from the inertia and aerodynamic forces during the stroke reversal. The whole system consists of an electromagnetic actuator including a coil and a magnet, double planar four-bar systems, an airframe, and double wings. The actuator produces instantaneous forces by a cantilever beam integrated with a laser displacement sensor. Kinematics of the wing images are collected by high-speed cameras. The total system is compromised from a weight of 80 mg, and a wingspan of 3.5 cm. The flapping wing beat frequency is 80 Hz, the flapping amplitude is approximately ±70°, and the rotation amplitude is about ±60°. Thus, this system is the smallest known example of electromagnetically driven FWMAVs.

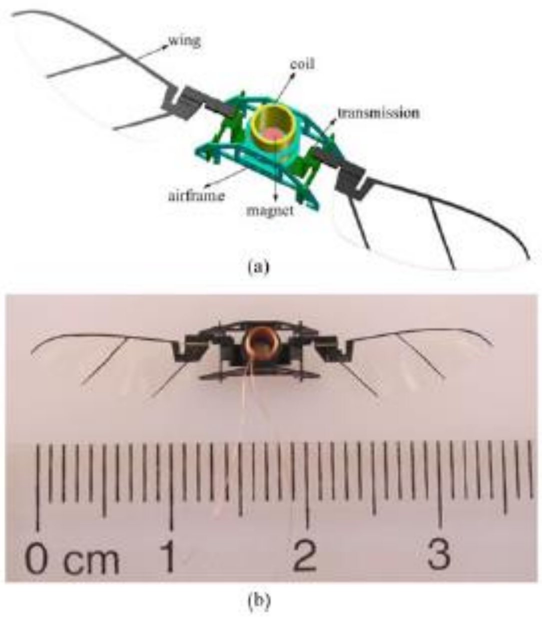

Figure 1.13 (a) CAD model of the robotic insect. (b) Prototype flapping-wing robot [12].

1.2.2 Bio-inspired flexible wings aeroelastic analysis

The unsteady aerodynamic force enhancement in bio-inspired flight mechanisms consists of leading-edge vortex generation and shedding, wake capture, and clap and fling. The efficiency of such unsteady mechanisms might be affected by morphological variation in the wings (shape, vein architecture, or flexibility) [13]-[15]. Flexible wings generate higher lift in particular via leading-edge vortices compared to rigid counterparts even though both have the same mechanical actuation systems. As the flapping motion mechanism creates sufficient unsteady aerodynamic forces, flexible wings with airflow around them generate structural deformations on wings. Thus, a coupled relation increases the efficiency of the micro air vehicle and decreases the power consumption of the system. Therefore, an aeroelastic analysis should be taken into account to light the secrets of the bio-inspired fliers. There are several active components to comprehend the nature of the wings, namely, the anisotropy due to the membrane and veins, and hinges endurance materials which result in the spanwise and the chordwise wing flexibility, and also the dorsal (upper side) and the ventral (underside) flexibilities of the wing. Since the wing shape and wing deformation play a crucial role in lift generation during wingbeat [15].

Butterflies are insect-sized flapping wings that are mostly anteromotoric (being driven primarily by the forewings) flyers though two wing pairs (fore and hinge wings) possess during flights. The two wing pairs overlap without a mechanical connection, especially during gliding flight, and these pairs form a continuous aerodynamic surface. Through a forewing-hindwing pair, the power is contributed during rapid maneuvers in flapping flight. Fore- and hindwing shape is considered as a single-wing planform when the effect of wing shape is investigated [13, 16, 17, 18, 19]. The effective shape of the butterfly's wings is planar and hardly cambered even at rest. The elastic texture of the butterfly wings has considerably obvious deformations in spanwise and chordwise directions. These deformations might be aerodynamically advantageous, as they can allow dynamic adaptation to the fluctuant requirements of force generation over the wingbeat path [20].

Satapanapituggit et al. conducted a numerical unsteady flow analysis [16] with two butterfly-like flapping wings. The characteristics of hover and translate motions are considered semi-rigid multi-body systems and so investigated with limited flexibility of their wings. The average Reynolds number is calculated as Re ~ 500 in this study for both hover and translation. The main aim of the study is the fluid-structure interaction of the rigid butterfly wings. The assumption of the limited flexibility or rigidity of the wing results in no deformation of the wings. Thus, computations are simplified by assumptions. In addition, when the wings flap in one fixed stroke plane, perpendicular to the body axis during both up and down, the point where a mid-way can be defined at $\alpha = 0°$ as a reference for comparison.

Twigg et al. [21] studied flapping butterfly wing (Monarch) flight enhancement presumed fluid-structure interactions provide sufficient conditions. In this study flow characteristics are not investigated by the authors. Before mimicking the characteristics of the monarch butterfly wings, they evaluate the aeroelastic performance of real monarch fore wing and then apply natural measured values to produce an artificial wing. First, force-deflection measurements by a motion capture camera system force transducer, and a finite element solver are conducted by using a micro-CT scan to determine the density and elastic modulus. After, a membrane wing with 3D-printed vein structures is produced by using these structural parameters. From this study, both spanwise and chordwise deflections are investigated, and also flapping frequencies with the peak force values are determined for both real and artificial wings. It should be noted that the obtained frequency and force values show that are in close correlation with each other. Real right forewings performed optimally at approximately 10 Hz, the flapping frequency of a live monarch butterfly, with a peak force of 4 mN. The artificial wing performed optimally at approximately 8 Hz with a peak force of 5 mN.

In literature, there are considerable studies on the structural deformation effects in the flow field of flapping wings. Senda et al. [22] studied the effects of the structural flexibility of the wings of the Parantica sita niphonica butterfly in flapping flight. Experiments with live butterflies are conducted in low-speed wind tunnel to verify the proposed dynamics models and to find the required parameters. Force data are collected by strain gauge force/torque sensor. The sensor is tethered with wire to the butterfly. A simultaneous measurement for the trajectory of flapping flight is constructed with an optical measurement system by three high-speed cameras. In experiments, it is seen that the wing deformations can be only observed quantitively, and numerical simulations differ from the experiments due to the rigid wing's hypothesis. Therefore, the structural flexibility of wings is required to be added as a model to evaluate the effects. In this study, two models are proposed to integrate two aspects of wing deformation. One model for aerodynamic forces which are calculated by the panel method. To clarify the aerodynamic forces, that model is called the bending model. In the second model, the structural flexibility of the flat wing is obtained by passive wing torsion caused by the wing twists due to the aerodynamic disturbances. Using these models, both the aerodynamic efficiency and the flight stability can be improved for live butterfly which have structurally flexible wings.

A comprehensive study of elastic deformation and flow field determination is conducted by Truong et al. [23]. In this study, the main challenge in the artificial wings is pointed to imitating the camber deformation and wing twisting. The elastic materials at the wing root vein are used to bend in the spanwise direction towards upward and inward. Thus, an angle of attack, camber, and twisting deformation can be generated during 1 DOF flapping motion via aerodynamic forces acting on the wing. The flapping wing equipment for multidisciplinary experiments is appointed to investigate the flexible wing kinematics and aerodynamics of real-size insect wings. In the experiments, the natural frequency, the force production, three-dimensional wing kinematics as well as the effects of wing flexibility are performed on the flexible wings in the hovering condition. Six wings were designed, fabricated, and tested with various venation models inspired by previous studies. The system is powered by a DC power supply in the flapping frequency of 10 to 25 Hz, and it reaches a maximum stroke amplitude of $92^{o.}$ The force measurement with a six-component force/torque sensor ATI Nano 17 is employed for the flapping mechanisms. To obtain the flow structures of unsteady aerodynamics of the three-dimensional flexible wings, a stereoscopic digital particle image velocimetry (SDPIV) is used. In addition, the natural frequency of the six designed wings is determined by using a Base-Excitation model testing by electro-mechanical shaker and laser vibrometer. Thus, the fluid-structure interaction of bio-flexible wing is investigated both quantitatively and qualitatively.

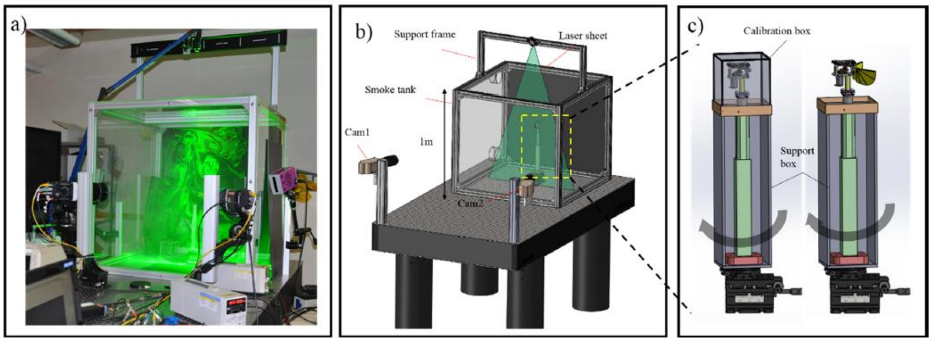

Figure 1.14 Experimental setup of Truong et al. [23].

Nguyen et al. [24] explore the effects of wing flexibility on several characteristics of flight, a numerical study is conducted based on the hawkmoth Manduca sexta like *Agrius convolvuli hawkmoth*. The power requirements, the trim conditions as well as the dynamic stability of an insect-like flapping-wing micro-air vehicle (FWMAV) are analyzed by the fluid-structure coupled method. For the fluid part of the analysis related to the body and the wings, a potential-based aerodynamic model coupling consisting of the unsteady panel method (UPM) and the extended unsteady vortex-lattice method (UVLM) is applied to compute aerodynamic forces. Meanwhile, the anisotropic wing structure is analyzed by using the finite-element method program ANSYS Mechanical APDL considering the mass and stiffness distributions of hawkmoth wings. The results of flexible and rigid Manduca sexta wings show that they differ considerably from each other in trim conditions. At flight speed is less than 3.0m/s, flexible wings require less power, and more stable lateral dynamics are observed from FWMAV. However, beginning at 4.0m/s flight speed, the flexible wing requires even more mechanical power than its rigid counterpart. The last findings can be sorted as follows: by using flexible wings, first, the flapping frequency is reduced at hover and when flight speed increases the reduction of frequency is a tendency to diminishment; the second is the pitch damping which is reduced by the flexibility of wing and inversely magnifies the body pitch oscillation up to at 3.0 and 4.0m/s flight speeds. Next, at hovering and low-flight speeds, flexible wings may reduce the use of mechanical power due to the increase in the stroke plane angle. However, at 4.0m/s and later speeds, an adverse effect of wing flexibility on flight efficiency is observed and this condition may require more power consumption. Finally, the effects of wing flexibility are investigated on the dynamic stability characteristics of longitudinal and lateral flights. The lateral dynamics during high-speed flight are also conservative. On the contrary, the lateral dynamic is enhanced significantly using the flexible wings.

Another study on flexible deformation impacts of flapping wings on aerodynamic performance and inertial forces is presented by Yang et al. [25]. A numerical method is proposed to simulate a dynamic fluid-structure interaction of both the structural deformation and the aerodynamic characteristics of flexible flapping wings for micro air vehicles (MAVs). The fluid-structure coupling consists of three-dimensional unsteady compressible Navier-Stokes equations and structural dynamic equations. Moreover, an interface data exchange method depending on the radial basis function is identified and the moving mesh generation method based on the infinite interpolation is applied in the coupling part. The numerical part is validated with low-speed wind tunnel experiments to keep the Reynolds number corresponding to the insect-size flier applications. The experimental results and the numerical simulations are compared, and the results show that there is quantitatively good agreement between the lift and the thrust coefficients. From the results, one of the assertions is about the induced chordwise twist angle due to structural flexibility which impacts the thrust. Another inference is on the inertial force which increases faster than the aerodynamic force regarding flapping frequency increase.

Monarch butterflies are one of the most recognizable butterfly species that immigrated along long distances. However, their aerodynamics and physics of mechanics have been already undetermined. Surrounding unsteady flow characteristics of the butterfly flight, comprising leading-edge vortex generation and shedding, wake-capture, and clap and fling [26],[27], enhance the aerodynamic lift. Therefore, the monarch butterfly has large wings but a thin body, the wing-body motion reduces the wing loading which leads to a noticeable saving power consumption [28] and short-term pitch stability during the forward flight [29].

Satapanapituggit et al. [16] conducted a numerical unsteady flow analysis with two butterfly-like flapping wings. The characteristics of hover and translate motions are considered semi-rigid multi-body systems and so investigated with limited flexibility of their wings. The average Reynolds number is calculated as Re ~ 500 in this study for both hover and translation. The main aim of the study is the fluid-structure interaction of the rigid butterfly wings. The assumption of the limited flexibility or rigidity of the wing results in no deformation on the wings. Thus, computations are simplified by assumptions. Besides, when the wings flap in one fixed stroke plane, perpendicular to the body axis during both up and down, the point where a mid-way can be defined at $\alpha = 0°$ as a reference for comparison.

According to Ortega Ancel et al. [13] focus on the aerodynamic evaluation of the wing shape and wing orientation of selected butterfly species. The fundamental importance of the fore-wing hindwing orientation is the gliding performance of the butterfly affected by maximizing the wingspan by extending the forewing. In both low-speed wind tunnel for different angles of attack, the aerodynamic force coefficients are measured, and results are compared with steady CFD simulations solved turbulence models on the wing boundary layer so similar results are obtained from the two studies. Numerical simulations revealed that forward forewing orientation gives a lower performance at low angles of attack but a better performance at high angles of attack.

Due to exciting aeroelastic characteristics and complex fluid-structure interaction features, Monarch butterflies are a favorable investigation tool and recently started to work on these issues often [30], [31]. Aeroelastic characters help us obtain how much real wings can deflect along with spanwise and chordwise directions under the point loads and what are the flapping-pitching amplitudes. After determining these characteristics, we can measure the forces produced by real wings in the concerning directions. Besides one of the important structural parameters, Young’s modulus (E) -characteristics of flexibility- is calculated based on the FEA, by this information an artificial wing can be produced concerning this value [30]. Furthermore, on the other hand, fluid-structure interaction properties can be investigated in the computational domain. The structural characteristics such as density, Young's modulus, and vein structures are applied to FEA and coupled with the fluid flow conditions. Thus, in every environment, the flight properties of Monarch butterflies can be determined [31].

1.3 The State of Art of Thesis and Problem Definition

This thesis is inspired by natural flyers and their wing shapes, materials, and secrets of aerodynamics. In recent years natural flyers have provided an understanding of flapping wing flight and expectations about the physics of MAVs. Flapping wing flight of natural flyers is a complex process involving many interdependent variables such as unsteady mechanisms including the leading-edge vortex, tip vortices, wake capture phenomenon, the clap-fling mechanism, and active/inactive upstrokes. At low Reynolds numbers, the unsteady aerodynamics of wings in a horizontal plane play an important role during flapping motion, especially in unsteady insect flight. Butterflies might be corresponding examples with their wing's flap kinematics by simply changing the usage of various unsteady mechanisms. In addition, flap motion, the importance of wing flexibility, and how it affects flight performance are required to be investigated in terms of the spanwise-chordwise wing stiffness.

The forewing and hinge-wing fully opened orientation of the butterfly, maximized the wing chord, is determined through the flow structures and around the fluid flow. The Monarch butterfly is used as a baseline case for further studies. The Monarch butterfly is well-known for its gliding flight and high capability of forward motion performance at high speed when its wings are lifted above the body. Based on the unsteady simulations and experiments, the aerodynamic coefficients, pressure, and 3D vortex core by velocity values and L/D ratio of the wing are compared with the literature. In addition, this study provides more detailed insight into the higher angle of attack and discussion on the aerodynamic coefficients of the wing model at those angles.

Figure 1.15 Monarch butterfly [32].

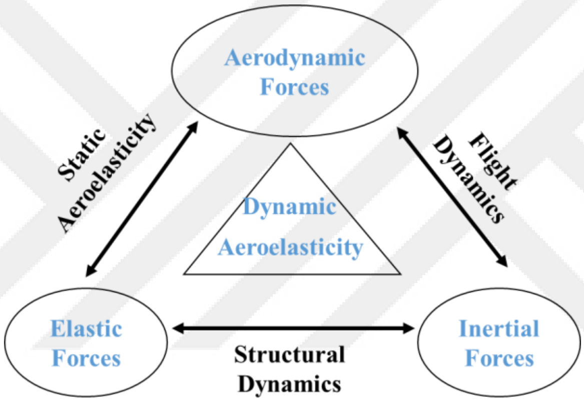

Figure 1.16 Collar diagram of dynamic aeroelasticity

Butterflies exploit the unsteady dynamics of their flights. However, by this time, the coupled wing-body dynamics, and the fluid-structure interaction of large and thin wings are underestimated by MAVs' researchers. Therefore, the main aim of this thesis is to analyze the aeroelastic effects of flexible butterfly wings by developing experimental and numerical methods. The study of aeroelasticity is the interactions between inertial, elastic, and aerodynamic forces presented when an elastic body is exposed to a fluid flow. Aeroelastic effects occur for flapping wings studied on a coupling between the wing fluid dynamics and structural dynamics. Several experimental and numerical studies are focused on flexible wings, to examine wing flexibility concerning wing performance and efficiency on their flights. In addition to aerodynamics, dynamic aeroelasticity plays a role in analyzing the deformations of the flexible flapping wings. Flexibility affects the production of aerodynamic and inertial forces.

In experiments, some complicated deformations are observed on the wing models, and these cause challenges that cannot be overcome by computational methods. Due to inaccurate simulation results, an alternative strategy is used to achieve the complexity of those deformations. Unique morphological data regarding the wing's deformation can be procured experimentally through DIC system techniques. These factual deformations are subsequently employed as inputs to incorporate aeroelastic effects within computational fluid dynamics (CFD) simulations. This method bypasses the need for detailed structural modeling since the wing's morphological data are acquired in advance.

1.4 Dissertation Organization

The 3D dimensional analyses are conducted to investigate the novelty of the method.

The thesis consists of five chapters and proceeds as follows:

- The experimental state-of-art is reviewed in Chapter 2.
- The numerical implementation of the wings is described in Chapter 3.
- Chapter 4 presents the outcomes of the unsteady aerodynamic analysis conducted on the stationary Monarch butterfly wing, along with the validation of the methodology through error sensitivity studies.
- Chapter 5 outlines the findings of the analysis on unsteady aeroelastic effects for wing models activated by piezoelectric materials. Additionally, the chapter explores the validation studies of the methodology.
- Finally, the effort spent on the current thesis and some important estimations of the methodology are concluded with recommended future work and possible improvements.

CHAPTER 2

EXPERIMENTAL TOOLS AND METHODOLOGY

In nature, the flapping motion of the biological wings consists of not only 1- DOF flap motion but also quite complex shapes with 3-DOF directions [33]. These motions could be investigated by filming the fliers and imitating various experimental methods. During the flight, one of the fundamental motions of biological fliers is flapping motion. Due to the contribution of the lift force to carry the weight and thrust for the translational move, the flapping motion is the most important motion that still requires detailed investigation by scientists and engineers.

Throughout the thesis, 1-DOF flapping motion is going to be taken into account which is actuated by the piezoelectric material. The deformation of the wing due to the flapping motion is going to be in the vertical direction (cartesian z-axis), simply up and down. In the following chapter bioinspired wing model selection, wing material, actuator selection, and experimental setups are going to be described in detail.

DIC system is combined with a force/moment sensor system to collect the aerodynamic forces of the wing. In the study, as preliminary experiments, the Rufous hummingbird model wing, and a rectangular wing model are selected for investigation.

Table 2. 1 Characteristics of the preliminary experimental wing models.

Parameter	Real Rufous Hummingbird [34]	Rufous Model Wing	Rectangle Model Wing
Chord	~ 16 mm	48-50 mm	48- 50 mm
Span	~ 50 mm	150 mm	150 mm
Flapping frequency, f	40-45 Hz	12.1 Hz	9.6 Hz
Thickness	-	0.4 mm	0.4 mm

The piezoelectric actuator of the wing models is fed by sinusoidal waveform and after repeated experiments the flapping frequencies. The data collected by force/torque sensor is analyzed by FFT and the frequency values are determined as 9.6 Hz for the rectangle wing and 12.1 Hz for the Rufous hummingbird wing as shown in Figure 2.2 and Figure 2.3, respectively.

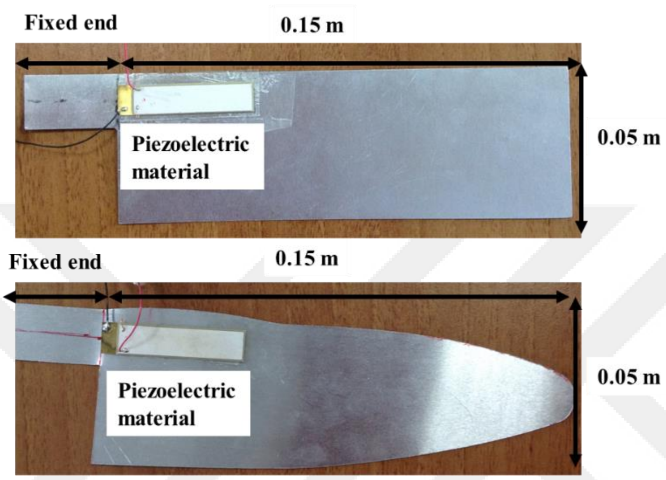

Figure 2.1 Wing models.

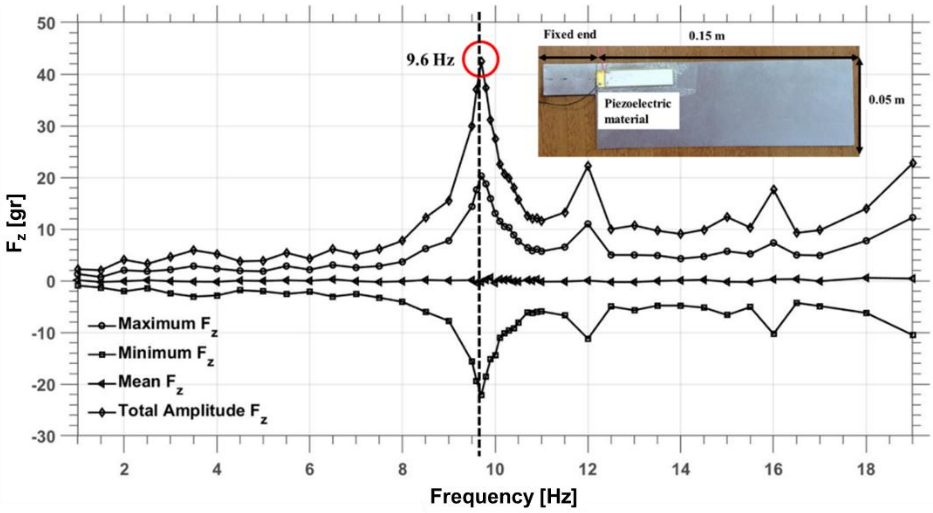

Figure 2.2 Rectangle wing natural frequency.

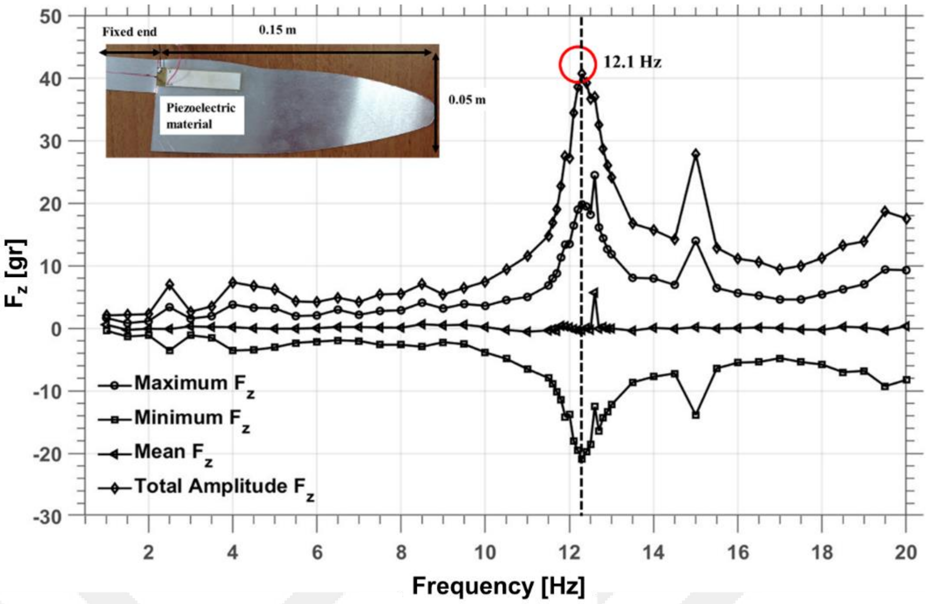

Figure 2.3 Rufous Hummingbird wing natural frequency.

2.1 Wing Materials Preparation for Experiments

At the beginning of the study, most of the materials were tested as shown in Figure 2.4, however, most available materials are not satisfied with the robustness against the electrical circuit outputs of the piezoelectric material such as temperature-long-time experiments. Because of the irreversible degradation observed in the material structures of potential candidates, the decision is made to opt for aluminum (Figure 2.1) as the wing material. Aluminum, being a lightweight metal with high flexibility, thinner and stronger, is an omnipresent material.

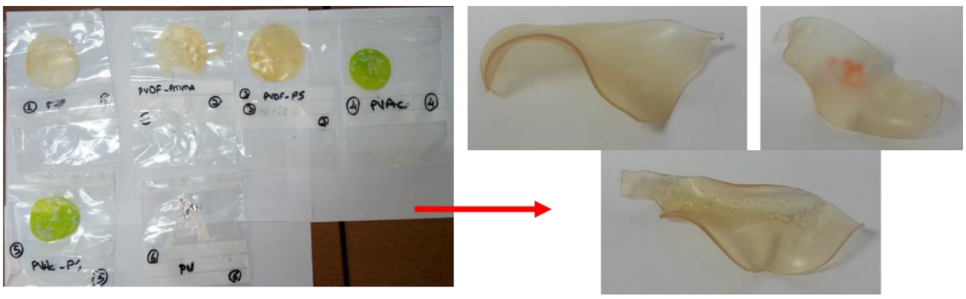

Figure 2.4 Some available wing materials (before experiment → after experiment).

Due to its advantages, it is a very suitable material for flapping wing experiments. Following the decision to utilize aluminum material, an assessment of its properties is conducted through a tension test. The specimen for the tension test was prepared by ASTM standards [35]. The solid model of the specimen prepared for the tension test is presented in Figure 2.5. Using the solid model, the aluminum plate is cut on a CNC machine, and subsequently, the Elasticity Modulus (Young's Modulus) and Poisson's ratio values are determined through the tensile test conducted using tension testing machines (Table 2.1). The aforementioned values are compared with previously obtained values for an aluminum plate, confirming that the obtained values fall within the range accepted in scientific circles.

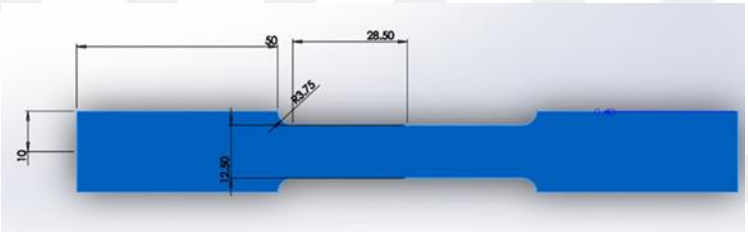

Figure 2.5 Model prepared for the tension test.

Table 2.1 Aluminum tension test results.

	Unit	**Aluminum**
Parameter		
Elasticity Modulus (Young's Modulus)	N/m^2	6.804×10^{10}
Length	m	0.15
Width	m	0.05
Thickness	m	0.0004
Density	kg/m^3	2700
Poisson's Ratio		0.354

2.2 Piezoelectric Actuator

It is important to emphasize that the flapping systems are of small size and their wings are capable of generating enough lift force to carry their weight. Piezoelectric actuators are very appropriate components, due to their lightweight and effective actuation capability. To perform the flapping motion of the wing models, a single piezoelectric material is stuck to the surface of the wing. To ensure electricity insulation, adhesive tape is used. During experiments, the dimension changeability of the piezoelectric material is used when subject to voltage.

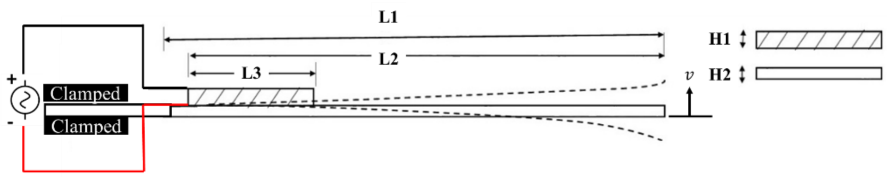

Figure 2.6 Schematic side view wing and piezoelectric material positions.

Table 2.2 Dimensions of wing models and a piezoelectric actuator.

Length of the wing with clamped end	L1=180mm
Length of wingspan	L2=150mm
Length of piezoelectric	L3=40mm
Thickness of piezoelectric	H1=0.5mm
Thickness of wing	H2=0.4mm

As described in Figure 2.6 shown above, a cantilever wing has one of its end points fixed to its base while the other end is allowed to move freely. A voltage load is applied to the piezoelectric material and the free end of the beam starts moving flapping motion. This is called the “converse piezoelectric effect" which denotes the alteration in the shape of piezoceramic resulting from changes in its electric poling induced by applying sufficient voltage. This effect involves a mechanical strain generated by a shift in polarization. The piezoelectric bending actuators can achieve displacements of several millimeters, responding within milliseconds.

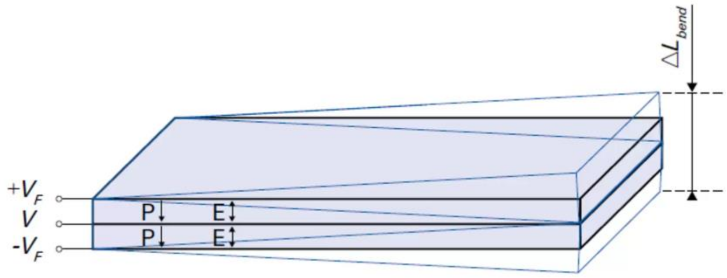

Figure 2.7 PI, PICMA Bender [36].

However, the piezoelectric displacement is intrinsically very small therefore some kind of motion amplification mechanism is required to achieve large deflection. Due to this reason, the wing models enlarged in size are shown in Figure 2.1.

To drive the piezoelectric actuators a function generator (Tektronix AFG3021B function generator) and a voltage amplifier (Active Control Experts (ACX) Quick pack Power Amplifier) are used shown in the following figure.

a) b)

Figure 2.8 Piezoelectric electric circuit components a) function generator, b) amplifier.

2.3 Force Measurements for Piezoelectric Actuated Wing Models

Force measurement involves the interdependence of numerous components. The subsequent subsections provide a detailed introduction to the experimental components employed in force measurement.

2.3.1 Force/Torque Sensor

During the experiments ATI Nano 17 force/torque sensor is used to measure the aerodynamic forces namely lift, drag forces additionally moments of the biomimicking wing models. The ATI Multi-Axis Force/Torque Sensor system measures all six components (measures the outputting forces and torques from all three cartesian coordinates x, y, and z) of force and torque. The system consists of a transducer, shielded high-flex cable, an intelligent data acquisition system, an Ethernet/Device Net interface, or F/T controller [37]. Its Maximum allowable overload values are 3.1 to 6.9 times rated capacities. Silicon strain gages provide a signal 75 times stronger than conventional foil gages [37].

Firstly, one piezoelectric material is stuck on the surface of the wing object as seen in Figure 2.10. To start measurements, the wing is clamped on the force sensor by the laser-cutting plexiglass tools. 3-layer tools are designed and cut for the attachment procedure.

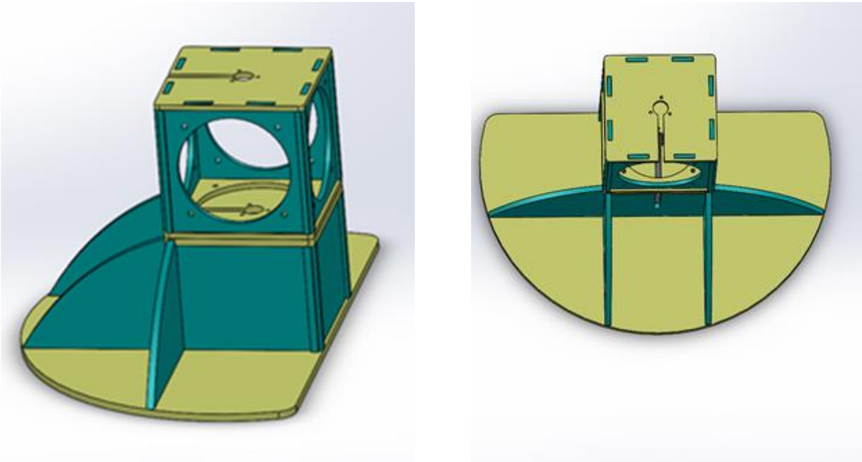

Figure 2.9 Different perspective view of plexiglass support force sensor support.

Additionally, a plexiglass support is drawn and cut for positioning and fixing the force sensor vertically (Figure 2.9). After all setup components are complete including the DAQ system of the sensor and computer connections to the NI system as shown in Figure 2.10, the piezoelectric material is started feeding with amplified voltages. To generate the flap motion, the shape of the voltage is adjusted to the sinus function. Initially, the frequency of the sinus function is increased by the step of one Hz then the wing reaches its natural frequency. Due to its flapping amplitude increasing as shown with bare eyes, the steps of the frequencies are decreased to 0.1 Hz, to investigate the changes in the force values of the flapping motion. The whole experimental sampling takes place between 0-20 Hz frequency intervals. The measured force values are recorded as a text file. At the end of data recording, all six components (measure the outputting forces and torques from all three Cartesian coordinates x, y, and z) of forces and moments are obtained by the sensor. To evaluate all obtained data, the instantaneous force graphics are plotted at all measured frequencies. The natural frequency of the rectangular-shaped wing, model is determined as 9.6 Hz since the maximum force value at the z-axis is 20 [gr].

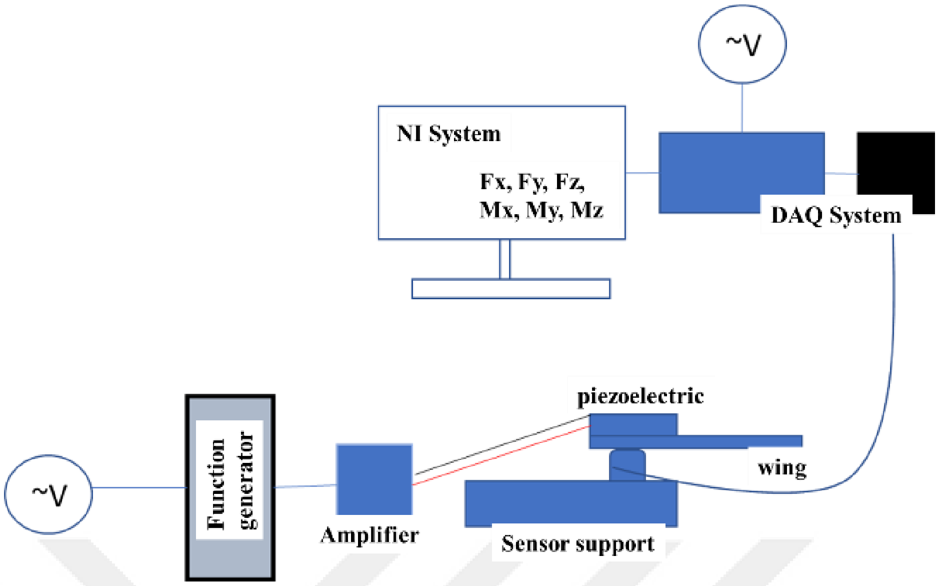

Figure 2.10 Flapping motion generation system with piezoelectric material amplification.

2.4 Displacement Measurements for Piezoelectric Actuated Wing Models

To capture the deformations of the flexible material wings, a high-speed camera system is preferred. During the study vertical displacement (z-axis) of the wing models is recorded and the image data is investigated by using image correlation.

In Figure 2.11b, the rectangular wing is shown in the DIC user interface. In the software, the speckling surface is tracked by high-speed camera shots. These images are recorded by the program and correlated for each timestep. After the post-process step, the deformations of the objects can be evaluated by the program.

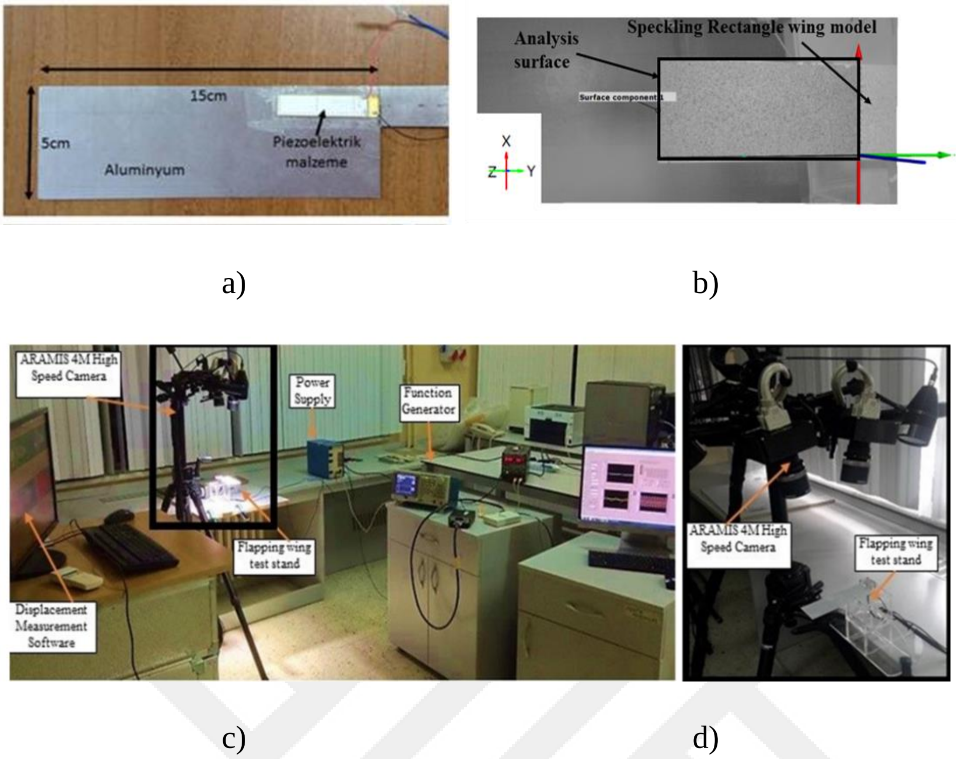

Figure 2.11 DIC system for a piezoelectric actuated aluminum wing. a) Rectangular wing, b) DIC system interface, c) ATI Nano 17 force/torque sensor system and DIC system setup, d) DIC system camera position on the wing test section.

2.4.1 ARAMIS 4M DIC system and lenses

Before obtaining measurements with a high-speed camera, there are significant preparatory steps to be taken. Among these, the most crucial is the calibration process to ensure precise measurements. Calibration is a procedure that is repeated each time according to the desired measurement volume. The measurement volume is contingent upon the surface area (height and length) of the object. If deformation is observed during the movement of the measured object, depth should also be considered as a third dimension. The specific features required for the calibration process, based on the volumes of the wing profiles, were selected from the table provided in the sensor configuration formats section of the ARAMIS 4M hardware user guide [37]. Additionally, hardware settings were adjusted in accordance with the 20 mm lens utilized in the experiment, as detailed in Table 2.3.

Table 2.3 ARAMIS 4M 20 mm lens properties [38].

Sensor	ARAMIS 4M rev03
Lens	Titanar 20 mm
Measuring volume [mm^2]	250 × 180
Min. camera support Length [mm]	500
Measuring distance [mm]	440
Slider distance [mm]	166
Camera angle [º]	25
Calibration object	CP20 250×200
Aperture-dependent depth of field [mm]	8 (aperture) >250

2.4.1.1 Calibration

The calibration process has been individually performed for each camera (Figure 2.12). To ensure accurate volume measurement, the CP20 250×200 calibration object, as outlined in Table 2.3, has been chosen. Table 2.3.

Table 2.3 is utilized to perform the three-dimensional (3D) calibration steps as outlined in the hardware user guide. Additionally, the ARAMIS GOM software provides sequential guidance for the calibration process, ensuring the ease of tracking the sequence of steps and when to execute them for each camera calibration. Figure 2.13 below illustrates how the object used for calibration appears in the right and left cameras before the commencement of processing. The purpose of this process is to perform focusing adjustment.

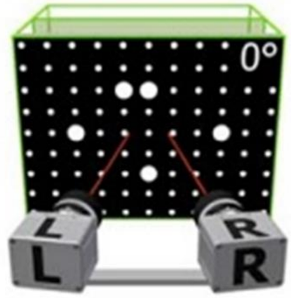

Figure 2.12 ARAMIS 4M calibration tool [38].

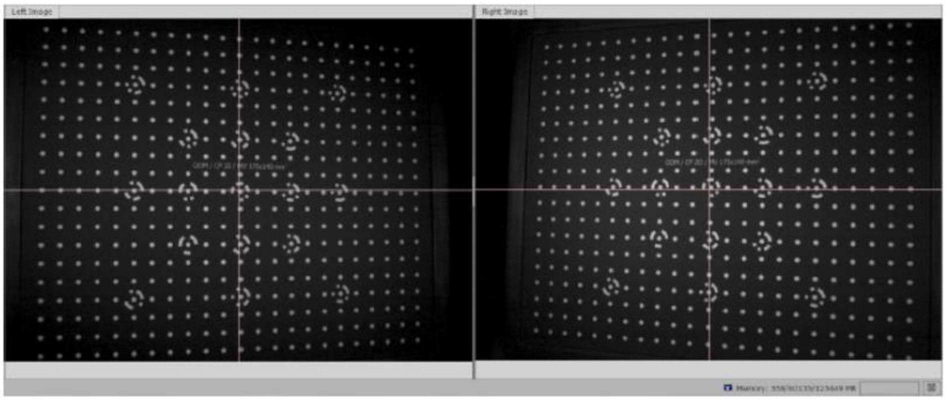

Figure 2.13 Calibration tool shown in left and right cameras [38].

After the camera lights are turned on, the “Overexposed Mode” is selected, and by right-clicking on the image, the image display is set to 'overexposed' to adjust the settings by changing the angles or increasing and decreasing the intensity of the red dots observed on the object. Figure 2.14 demonstrates the successful completion of the focusing process.

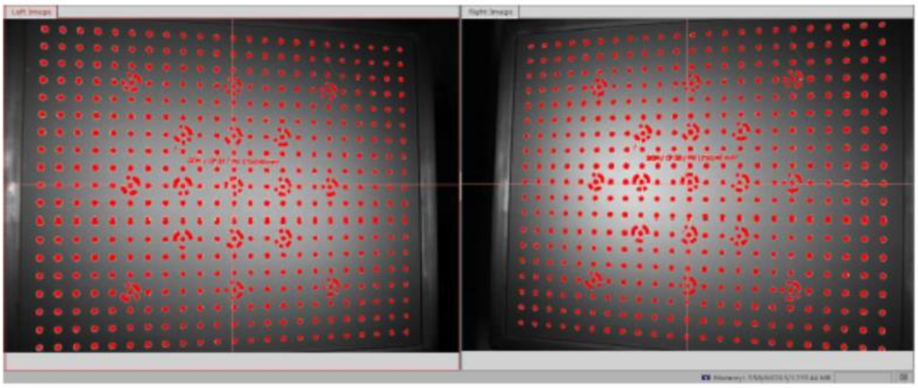

Figure 2.14 Overexposed dots left and right cameras [38].

After a successful focusing process, the appearance of the dots turning white in the images is expected to indicate the adjustment of the aperture setting. Once the dots turn white in the images, by right-clicking on the image, a false color adjustment is performed. This procedure ensures the calibration of the sensors.

Following the hardware-based calibration steps, the calibration process needs to be completed through software in the final stage. Under the “Sensor” section within the ARAMIS 4M GOM interface, the “Calibration” subheading allows the selection of the calibration object (CP20 250×200). As the program guides the user, after entering the aperture size used in the camera (20 mm) via the “Next” button, the process is completed. In the final stage, when the software presents a deviation of the calibration process between 0.01 and 0.04 pixels, it signifies a successful calibration. The calibration setting for the experiments was provided as 0.02 pixels by the software, indicating a successful calibration.

Upon completion of the calibration process, it is essential to select the image recording mode. According to the user manual, the most suitable option chosen was “Fast Measurement (PC RAM)”. The interface required the following data: the image rate per second set at 120.0 Hz, shutter time at 5 seconds, and the maximum number of images at 600. After selecting the “Use all” option to save all images, the calculation process was initiated.

2.4.1.2 Post-Processing

After selecting the measurement mode, the calculation process can be initiated. The final step to be checked is ensuring that the yellow surface generated on the surface for calculation does not exceed 0.3 pixels. This is crucial because an excess of the yellow surface indicates an intersection error in the three-dimensional facets (3D facet), necessitating recalibration. The steps of the calculation process can be outlined as follows:

1. Initially, masking is applied to the entire surface ("*Project* > *Mask* > *Define Mask*").
2. Subsequently, "Mask All" is chosen to mask the entire surface.
3. Then, the reverse of the masking process on the masked surface is executed using the "Unmask" tool. Despite various options for removing masks, "Unmask Rectangle" suitable for wing profiles in the project has been utilized.
4. Consequently, the surface for calculation is selected.
5. Clicking the unmasked surface results in the calculation surface turning green.
6. To perform the calculation, a starting point is assigned as a reference ("*Project* > *Add Start Point*").
7. Once the location of the starting point is determined, a point is assigned with "Ctrl + click".
8. If the selected starting point is unsuitable, the software indicates its unsuitability in red, prompting the selection of another starting point.
9. Now, starting points have been automatically selected for all stages, and the process continues with "Next".

10. A yellow checkmark next to each Stage indicates the addition of the starting point.
11. The calculation can now be executed with “*Project > Compute Project*”.
12. After the calculation process is completed, the software directs the user to the evaluation mode.

CHAPTER 3

NUMERICAL METHODOLOGY

This chapter proposes numerical studies to be adapted to the current research. Several computational methods defined introduce the evaluation steps of the thesis outputs. First, the morphological parameters of the wing are released from the literature, and then commercial CFD methods are implemented on the wing.

Flapping wing micro-aerial vehicles (MAV) have been ongoing developments for more than the last two decades.

3.1 Proposed Methods and Models

In this thesis, computational methods are investigated to make a validation of the methods. As a beginning, the flow domain is resolved by ANSYS Fluent software. Unsteady aerodynamics cases are performed to observe the flow characteristics. In the computation step not only aerodynamics of flexible wings but also structural deformations of them are taken into account altogether. A fluid domain is created for unsteady aerodynamic analysis in the wake of designing a scaled solid model of the butterfly wing.

This chapter is devoted to an in-depth review of aeroelastic estimation methods from computational fluid dynamics.

3.2 Piezoelectric actuated Rectangle wing and Rufous hummingbird wing

In general, birds employ wing flapping to create both lift and thrust; however, the mechanism becomes more intricate in smaller flyers. They exhibit varied and complex flapping patterns, altering the angle of attack between the upstroke and downstroke phases. For instance, in hummingbirds, the flapping motion adopts a sinusoidal pattern during hovering by higher frequency values (~100 - 200 Hz). These birds exhibit unsteady aerodynamic behavior while hovering by continuous flapping motion, and thus they can remain suspended in the air by creating enough force. The complexity of the problem raises the necessity for a simplified model. So, only the 1-DOF flapping motion is employed in the wing models.

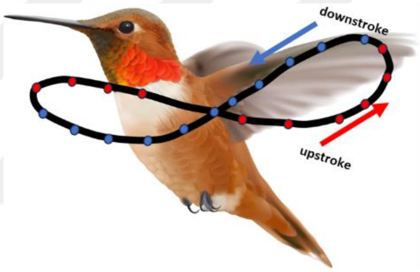

Figure 3.1 Hummingbird in hovering flight, wing's figure-eight patterns.

3.2.1 Morphological and Aerodynamic Parameters of Rectangle wing and Rufous hummingbird wing

Rufous hummingbird and rectangle wing models are reconstructed in the computational flow domain. The body of the hummingbird is neglected and only a single wing is investigated inside the fluid flow. A single degree of freedom- flap motion- is compared with rectangle wing shape cases. A solid model is created inside the computational domain and a wing is scaled to the surface area of 7500 mm^2 (S). To mimic the real wing, the thickness is taken as 0.4 millimeters. The key parameters are measured such as the semi-span for a single wing from root to tip 150 mm (R), and the mean chord and the nondimensional parameter aspect ratio are calculated as 50 mm (c_m = S/(2R)) and 3, respectively.

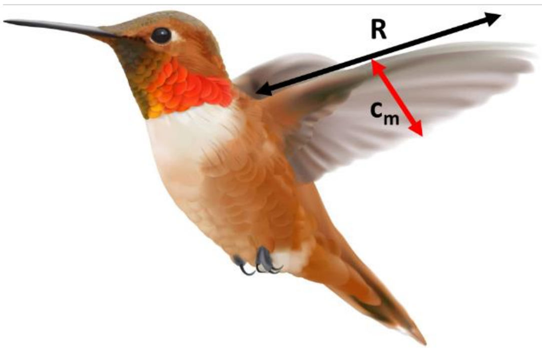

Figure 3.2 Rufous hummingbird, in hover position, respectively. R is semi-wingspan length; c_m is the mean aerodynamic chord.

Table 3.1 Dimensional parameters of Rufous hummingbird wing in the current study.

Parameter	Value
Forewing length (semi-span), R (mm)	150
Total wing area (single wing), S (mm^2)	7500
Mean aerodynamic chord, c_m =S/(b)	50
Aspect ratio, AR (R^2/S)	3

The Reynolds number represents the ratio between inertial and viscous forces within a fluid system. It serves as a dimensionless parameter utilized for classifying fluid systems, especially those where viscosity significantly influences fluid velocities or flow configuration. The Reynolds number serves as a criterion to ascertain the state of fluid flow, distinguishing between laminar and turbulent conditions.

$$Re = \frac{\rho \mathrm{Uc}}{\mu} \tag{3.1}$$

Where ρ is the fluid density, U is the velocity, c is a characteristic diameter, and μ is the dynamic viscosity.

In the classification of literature, insects and small birds are considered capable of flying at significantly low Reynolds numbers. The flow conditions around these fliers are characterized as laminar flow, therefore, numerical computations are performed using equations applicable to inviscid laminar flow cases for analysis in these scenarios (Table 3.2).

Table 3.2 Flow parameters for unsteady flapping wing study.

Parameter	Value
Wing tip velocity, U_{tip} (m/s)	0.67894
Air density, ρ (kg/m^3)	1.225
Dynamic viscosity, μ (kg/m. s)	1.7894× 10^{-5}
Reynolds number, Re =U. ρ. c_m/ μ	2324

3.2.2 Grid sensitivity study of Rectangle wing and Rufous hummingbird wing

In the experiments, the wing morphological deformation data can be obtained by using the DIC systems. Subsequently, this deformation data is utilized as input to incorporate the aeroelastic effect in the CFD simulation.

In this thesis study, after experimental deformations are collected and then for numerical analysis of the flapping motion, the fluid-based spherical domain is constructed around the 3D wing model.

For this study, tetrahedral elements are used to conform to the O-type mesh domain. In the study, two O-type domains are generated, and the wing models are set inside of the domains shown in Figure 3.4. For having an accurate result during dynamic mesh motion around the near field of the wing, a finer mesh is applied around the wing. The inner domain above the wing is constructed with a semi-cylinder having a radius of 350 mm. The outer spherical domain is constructed by a coarser mesh element. and has a 750 mm radius. The boundary condition for the far-field domain is assigned as pressure-outlet and the wing surface is set to a no-slip boundary condition. Table 3.3 shows that the number of mesh elements is coarse (Mesh 1), medium (Mesh 2), and fine (Mesh 3) mesh elements. The domain for fine mesh is presented in Figure 3.5 for both wings. The results are very close to each other. The wing models are investigated through instantaneous flapping motion displacements.

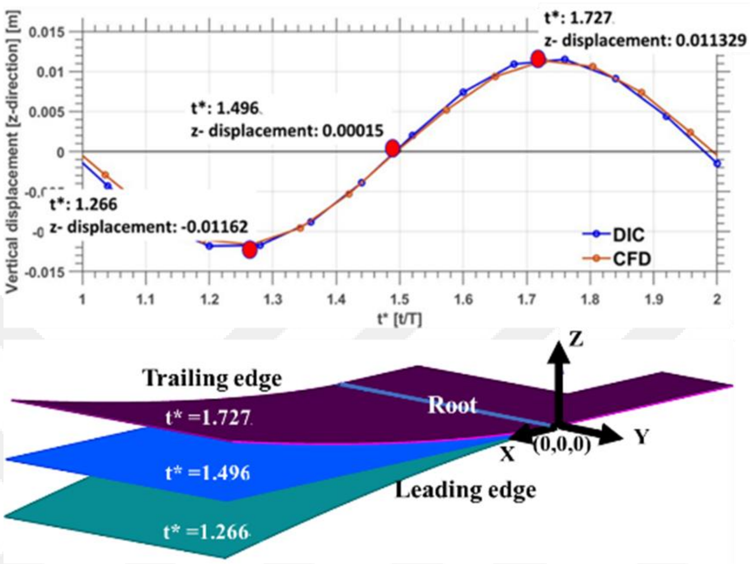

a)

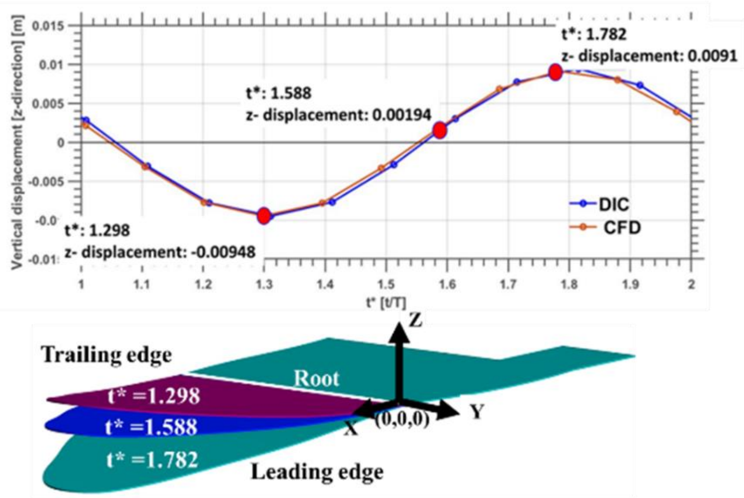

b)

Figure 3.3 Instantaneous wing flapping angles and displacements from the current study, a) rectangle wing, b) hummingbird wing.

The effect of the flapping angle is observed by the DIC system and investigated by MATLAB code. The angle changes between θ ϵ [-6°,6°] for rectangle wing, θ ϵ [-5°,5°] for hummingbird wing (Figure 3.3).

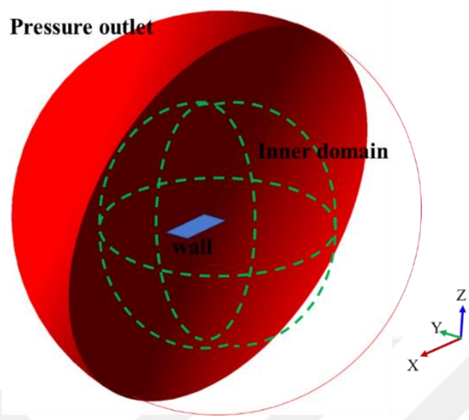

a)

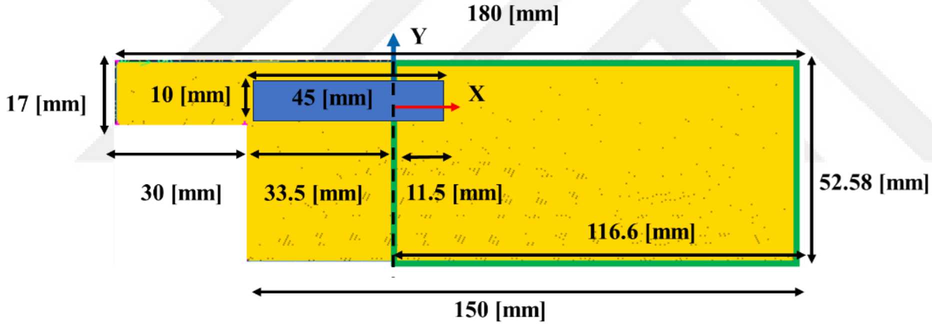

b)

Figure 3.4 a) Flapping wing computational domain and boundary conditions, b) dimensions of flapping wing and cartesian coordinate system.

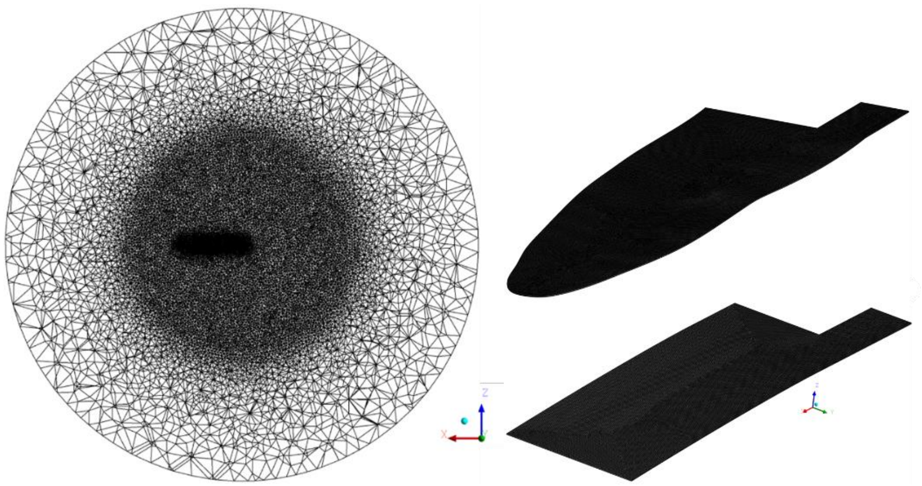

a) b)

Figure 3.5 Flapping wing mesh domain a) whole grid domain, b) wing's surfaces in the domain.

In laminar flows characterized by low Reynolds numbers ($100 < Re < 10^3$, where laminar boundary layer theory is applicable), and with $y^+ < 1$, the grid spacing near the wall is defined based on flat plate boundary layer theory. However, a boundary layer is not generated due to the limitations in dynamic mesh motion within FLUENT. Structured mesh above the wing surface is unfeasible; therefore, mesh spacing is adjusted instead of a structured boundary layer to achieve desired y+ values (Table 3.3 and Figure 3.5).

Table 3.3 Total mesh elements of wing prototypes.

Wing	**Mesh type**	**Number of elements**	**Time step**	**Face [mm]**	**Inner domain face [mm]**	**Body [mm]**
Rectangle	**Mesh 1**	1.022.700	Δt=0.0005 s	1.2	10	100
	Mesh 2	3.591.301		0.9	10	100
	Mesh 3	5.398.766		0.5	10	100
Rufous Hummingbird	**Mesh 1**	1.120.760	Δt=0.0004 s	1.2	10	100
	Mesh 2	3.820.346		0.9	10	100
	Mesh 3	5.198.700		0.6	10	100

For the grid refinement analysis, face sizing is allocated to the wing surface with a specified growth rate of 1.2. The face grid is expanded according to this growth rate and extended up to the boundary of the inner domain as defined in the table. To fill the space between the inner and outer domains, body sizing or outer domain volume is employed. This process ensures the completion of grid structures across all computational domains. Due to the dynamic flapping motion of the wing and computational limitations, three grid sizes are generated, and computations are performed using these varied grid configurations.

While both medium and fine mesh structures produce similar results, a decision has been made to utilize a fine mesh structure for a more in-depth examination of the vortex structures. Consequently, the grid refinement study and simulations for both wing prototypes, rectangular and hummingbird, are concentrated on fine mesh cases. The simulations conducted on fine meshes provide insights into the instantaneous aerodynamic variables.

3.3 Piezoelectric actuated Monarch butterfly (Flapping wing)

After conducting studies involving the rectangular and hummingbird wings utilizing DIC (Digital Image Correlation) and CFD (Computational Fluid Dynamics), a similar computational analysis is employed to examine the flapping motion of the Monarch butterfly. This investigation builds upon the preliminary studies conducted with the rectangular and hummingbird wings, which were computationally verified. The concepts and methodologies derived from these studies are being applied to the analysis of the Monarch butterfly's wing motion.

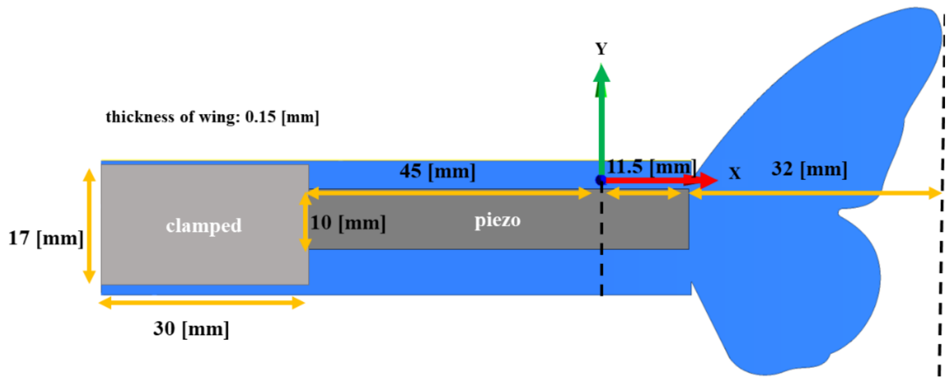

a)

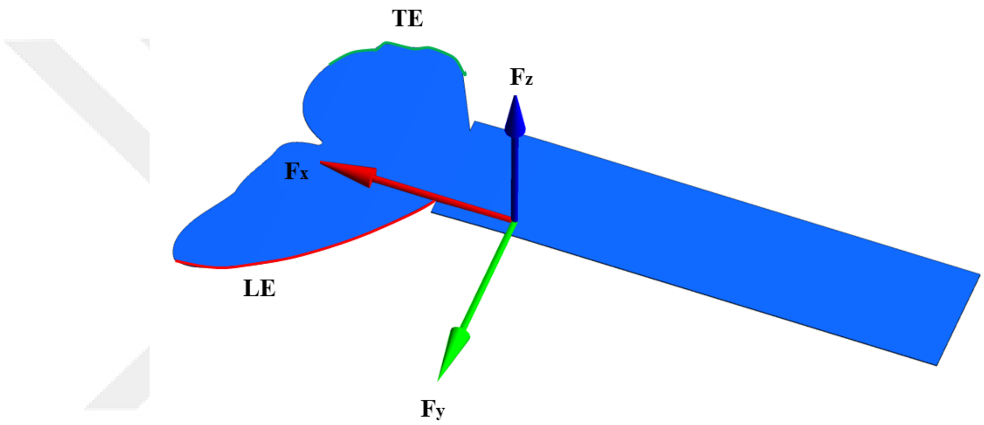

b)

Figure 3.6 Flapping Monarch butterfly wing size in the computational domain.

The dimensions of the Monarch butterfly wing, within the spectrum of real butterfly sizes, align with the earlier examination of rectangular and hummingbird wings. Consequently, a model depicting the flapping motion of the Monarch butterfly wing is formulated, building upon the insights garnered from the preceding analyses.

Table 3.4 Monarch wing grid refinement study.

Wing	**Mesh type**	**Number of elements**	**Time step**	**Face [mm]**	**Inner domain face [mm]**	**Body [mm]**
Monarch	**Mesh 1**	2853582	Δt=0.001 s	1.2	10	100
	Mesh 2	3934357		0.48	10	100
	Mesh 3	5529241		0.26	10	100

Due to the computer sources, the mesh refinement study is limited by Table 3.4. For the detailed flow investigation, the finest mesh (Mesh 3) is used in the flowing chapters.

In consideration of sizing aspects and computational assessments, three distinct mesh configurations are employed. The investigation entails the comparative analysis of the vertical force F_Z [gr] and thrust force F_Y [gr] across these grids. Following an exhaustive grid refinement study, a mesh exhibiting grid independence is carefully chosen. Subsequently, the outcomes are thoroughly examined and validated using the finalized mesh configuration.

When examining the mean values concerning the flapping motion, it becomes apparent that the Monarch butterfly wing is capable of generating a positive force in the y-axis direction, implying a thrust toward the y-axis.

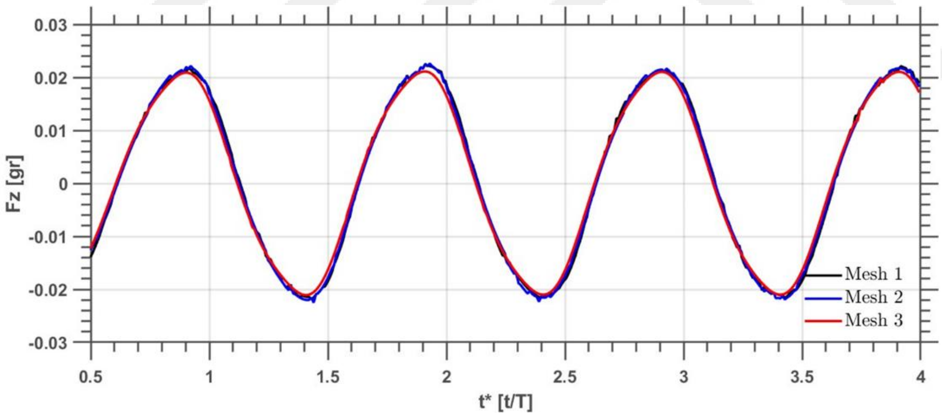

a)

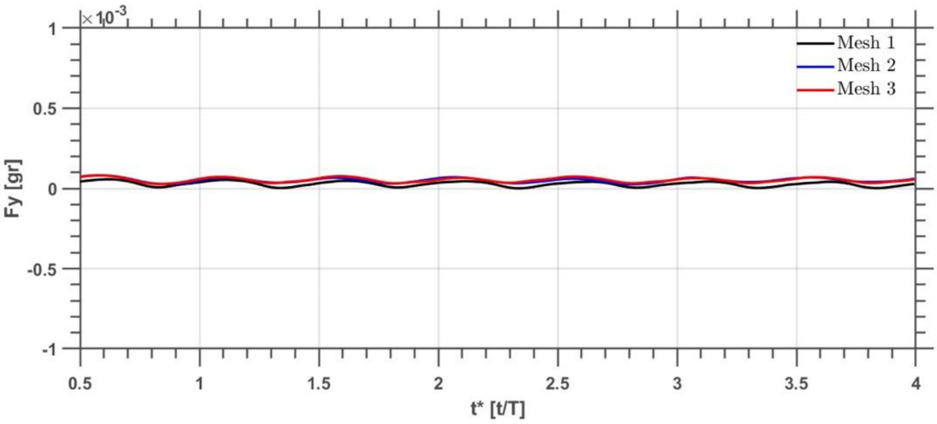

b)

Figure 3.7 Grid refinement study, a) Vertical force component (F_Z), b) Thrust force (F_Y).

3.4 Monarch butterfly (Stationary wing)

Moreover, our exploration extends to the flapping wing of the Monarch butterfly in hover conditions, as well as the investigation of stationary wings with varying angles of attack under free stream velocity. While the hover case didn't yield significant lift and drag, static wings at high angles of attack exhibited considerable lift and drag at free stream velocity.

Butterfly-like vehicles especially exemplify the low Reynolds number aerodynamics, and their flow physics vary with unconventional aerodynamic mechanisms during force generation namely, lift, drag, wake patterns, different leading-edge vortices, and active and inactive upstrokes [13]- [15]. Butterflies are included in an order of insects called *Lepidoptera*. They are one of the most widespread and widely recognizable insect orders in the world and they can fly in very agile motions in nature [16].

The objective of the current study is to investigate the instantaneous flow structures at different angles of attack employing computational fluid dynamics (CFD) simulations. Focusing on the forewing and hinge-wing fully opened orientation of the Monarch butterfly, maximizing the wing chord, determines the flow structures over the wing surface and around. The Monarch butterfly is used as a baseline case for further studies. The Monarch butterfly is well-known for its high capability of sharp flick forward motion performance at high speed with the wings lifted above the body [39]. Based on the unsteady simulations, the aerodynamic coefficients, static pressure, and 3D vortex core colored by velocity values and then the L/D ratio of the wing from Monarch butterfly are compared with literature. Besides this study provides more detailed insight into the higher angle of attack and discussion on the aerodynamic coefficients of the wing model at those angles.

3.4.1 Morphological and Aerodynamic Parameters of Monarch Butterfly

A monarch butterfly with a laboratory-pinned wing shape [13] is reconstructed in the computational flow domain. The forewings are positioned at the museum-pinned model means that the forewing is fully open forward in Figure 3.8. A detailed study on monarch (Danaus plexippus) butterfly wings is carried out. The wings are structured as a rigid material. The body of the butterfly is neglected and only a single forewing-hindwing couple is investigated inside the fluid flow. A single degree of freedom- flap motion- is compared to Ortega-Ancel et al. cases. For comparison with literature and further studies, the right-wing monarch (Danaus plexippus) is chosen. A solid model is created inside the computational domain and a monarch butterfly wing couple is scaled to the surface area of 900.03 mm^2 (S). To mimic the membrane of the real wing, the thickness is taken as 0.15 millimeters. The key parameters are measured such as the semi-span for a single wing from root to tip 31.68 mm (R), and the root chord length of 12.88 mm. Finally, the mean chord and the nondimensional parameter aspect ratio are calculated as 28.41 mm ($c_m = S/(2R)$) and 1.1150, respectively.

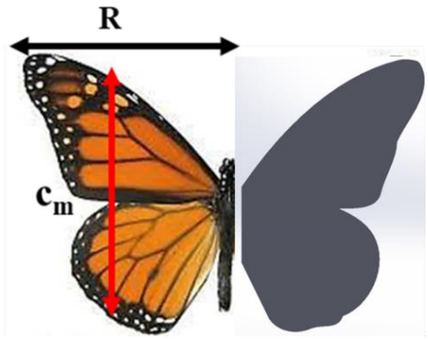

Figure 3.8 Monarch butterfly during museum position and gliding, respectively. *R* is semi-wingspan length; c_m is the mean aerodynamic chord.

Table 3.5 Morphological parameters considered in the current study.

Parameter	Value
Forewing length (semi-span), R (mm)	31.67892
Total wing area (single wing), S (mm^2)	900.00476
Mean aerodynamic chord, c_m =S/(b)	28.4102
Aspect ratio, AR (R^2/S)	1.1150

Compared to the literature, the dimensions are considered in similar values for the Monarch butterflies. In the study corresponding, the Reynolds number is obtained at 9,584 at 5 m/s free stream velocity. Straightforward free stream flow bumps into the wing model which is rotated inside the domain to determine the effects of angles of attack variations on the aerodynamic coefficients [30], [31], [40].

Table 3.6 Aerodynamic parameters considered in the current study.

Parameter	Value
Flow velocity, U (m/s)	5
Air density, ρ (kg/m^3)	1.125
Dynamic viscosity, μ (kg/m. s)	1.789×10^{-4}
Reynolds number, Re =U. ρ. c_m/ μ	9584

3.4.2 Grid and time sensitivity study of Monarch Butterfly

The solid model of the Monarch butterfly wing is imported into ANSYS design modeler, and a fluid-based rectangular domain is created around it. The mesh around the 3D Monarch butterfly shown in Figure 3.9 is composed of two parts, namely inner and outer domains. The inner domain above the boundary layer is constructed with a semi-cylinder having a radius of 40 mm with 30 mm depth and a length of 200 mm and used to refine the mesh around the wing. The outer domain is a cuboidal domain with dimensions 600mm×300mm×120 mm. The wing surface is placed three times mean chord ($3\bar{c}$) length away from the inlet and ten times the mean chord ($10\bar{c}$) from the outlet. The wing surface is assigned with a no-slip boundary condition. Besides, the other three sides of a rectangular domain are assigned by pressure outlet boundary. Lastly, the symmetric boundary is defined at the root of the wing.

The Monarch butterfly wing model, based on the literature [13][14][40][45], is investigated through aerodynamic forces with various angles of attack. The wing rotation is defined to be positive in the counterclockwise direction. The effect of the mean angle of attack angle is investigated between $\alpha \in [0°,40°]$ with 2° increment step between 0° and 10° and 10° amount between 10° and 40°. Meanwhile, assuming the incoming flow is kept at the stationary position in each case of wing rotation. Moreover, between 0^o and 10^o degrees an 8^o angle is additionally investigated to compare with literature in terms of vortices shape and velocity-pressure contours. Wake patterns, C_L, and C_D coefficients are shown in the following parts of the study.

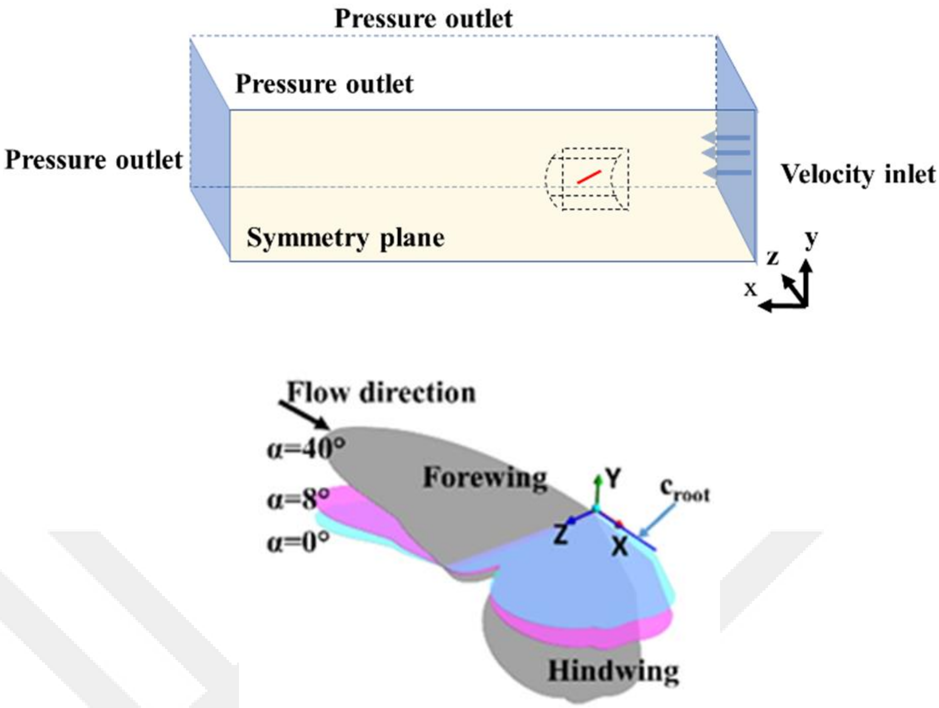

Figure 3.9 Computational domain and boundary conditions.

Under ANSYS Mesher body influence, face and edge sizing is applied to create all faces of the wing and enclosed domains. However, the mesh is denser near the tips and edges of the wing, a coarser mesh is produced towards the far field in Figure 3. A close view of the mesh is shown, and details of the boundary layer can be realized by zoomed images. The first cell spacing of the boundary layer value is calculated concerning y^{+} =0.72 < 1, therefore, the first spacing of the boundary layer is assigned as 0.035 millimeters and the corresponding Reynolds number is calculated as *9,584*. On the other hand, the boundary layer consists of twelve layers placed over the wing surfaces and a mesh refinement study is conducted by these configurations. Table 1 shows the sizing of edges, faces of the wing, and volume of the domain, and the numbers of total elements are given for each mesh. The domains have meshed using tetrahedral elements and a growth rate of 1.15 for all. Domain discretization with mesh points is subsequently increased from coarse mesh to extra fine mesh. For coarse mesh, the total number of volume cells is obtained as 2260769. On the other hand, a fine mesh has 4356291 elements, and this configuration creates a clustered region around the wing. Moreover, medium and extra-fine meshes are created consisting of 3405708 and 5148432 elements in total volume.

Regarding the domain and wing sizes, the grid sizes are subject to change. In this particular study focusing on a static Monarch butterfly within a rectangular domain exposed to incoming flow, the edges are divided based on a defined edge size. Specifically, the shorter edges correspond to the wing's thickness, while the other edges align with the shape of the butterfly's wing. Additionally, the face grid sizes are refined by a required face size, allowing the inner domain of the computational space to be filled. To complete the filling of the 3D rectangular domain, a body influence size is specified within the software. Moreover, for this study, a boundary layer is implemented in proximity to the wing shape.

Table 3.7 Summary of mesh refinement results for three-dimensional rigid wing computation.

Number of elements	**Mesh type**	**Face [mm]**	**Edges [mm]**	**Short edge [mm]**	**Body [mm]**	**Boundary layer**
2260769	Mesh 1	0.4	0.28	0.07	3	N= 12, $\Delta s = 0.035$ mm
3405708	Mesh 2	0.22	0.2	0.07	3	N= 12, $\Delta s = 0.035$ mm
4356291	Mesh 3	0.2	0.2	0.07	2	N= 12, $\Delta s = 0.035$ mm
5148432	Mesh 4	0.18	0.18	0.07	1.8	N= 12, $\Delta s = 0.035$ mm

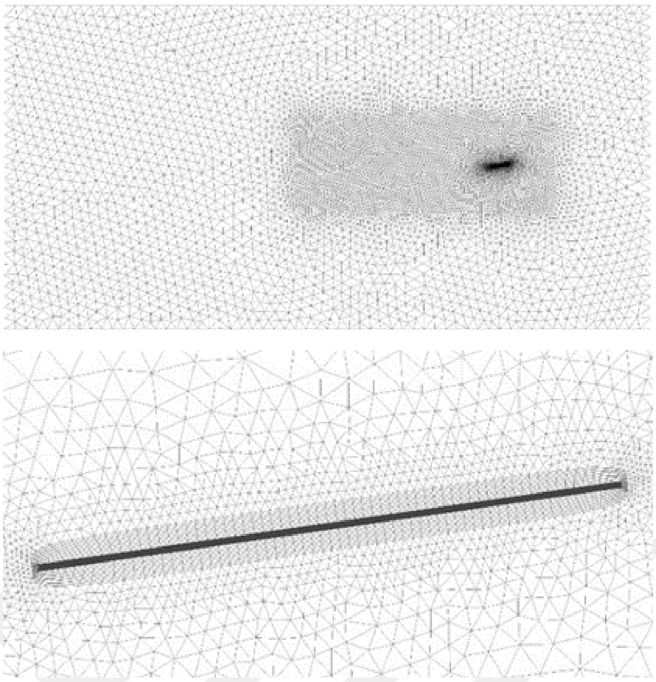

Figure 3.10 Mesh generated for the wing at $\alpha = 8°$. Medium mesh created with 12 boundary layers starting with 0.035 mm first inflation layer spacing.

Table 3.8 shows refined mesh sizes, computation time step, and outputs of the aerodynamic model. A refinement study is performed at an 8° angle of attack. For each mesh level, we calculate the mean lift and mean drag coefficients solutions for at medium mesh considered as the most accurate solution.

Table 3.8 Mesh and time refinement studies with error calculations at α=8°.

Mesh type		Mesh 1	Mesh 2	Mesh 3	Mesh 4	Mesh 5	Mesh 6
Number of elements		2260769	3405708	4356291	5148432	3856259	6917530
Δt=0.005 s							
	$\bar{C}_L$	0.2886	0.2894	0.2865	0.2862		
	$\bar{C}_D$	0.0664	0.0668	0.0663	0.0663		
Mesh refinement errors (Mesh $_{i+1}$–Mesh$_i$)/ Mesh$_{i+1}$	% Error in $\bar{C}_L$	-	0.27	1.01	0.10		
	%Error in $\bar{C}_D$	-	0.59	0.75	0		
	$\bar{C}_L$/ $\bar{C}_D$	4.34	4.33	4.32	4.31		
Δt=0.002 s							
	$\bar{C}_L$	0.2899	0.2912	0.2855	0.2863	0.2887	0.2885
	$\bar{C}_D$	0.0666	0.0668	0.0660	0.0661	0.0667	0.0666
Mesh refinement errors (Mesh $_{i+1}$–Mesh$_i$)/ Mesh$_{i+1}$	%Error in $\bar{C}_L$	-	0.44	1.99	0.27	0.86	0.0078
	%Error in $\bar{C}_D$	-	0.29	1.21	0.15	0.14	0.0095
Time refinement errors for Δt=0.005s	% Error in $\bar{C}_L$	0.44	0.61	0.35	0.03		-
	%Error in $\bar{C}_D$	0.30	0	0.45	0.3		-
	$\bar{C}_L$/ $\bar{C}_D$	4.35	4.35	4.32	4.32		4.33
Δt=0.001 s							
	$\bar{C}_L$	0.2911	0.2926	0.2869	0.2869		
	$\bar{C}_D$	0.0668	0.0671	0.0662	0.0662		
Mesh refinement errors (Mesh $_{i+1}$–Mesh$_i$)/ Mesh$_{i+1}$	%Error in $\bar{C}_L$	-	0.51	1.98	0		
	%Error in $\bar{C}_D$	-	0.44	1.35	0		
Time refinement errors for Δt=0.002s	% Error in $\bar{C}_L$	0.41	0.47	0.48	0.20		
	%Error in $\bar{C}_D$	0.29	0.44	0.30	0.15		
Time refinement errors for Δt=0.005 s	% Error in $\bar{C}_L$	0.85	1.09	0.13	0.24		
	%Error in $\bar{C}_D$	0.59	0.44	0.15	0.15		
	$\bar{C}_L$/ $\bar{C}_D$	4.35	4.36	4.33	4.33		
Literature							
	Number of elements (million)	$\bar{C}_L$ (CFD)	$\bar{C}_D$ (CFD)	$\bar{C}_L$/ $\bar{C}_D$ (CFD)	$\bar{C}_L$/ $\bar{C}_D$ (Experimental)		
Ortega Ancel et al. (2017)	1.6- 1.8	0.292	0.069	4.277	3.661		

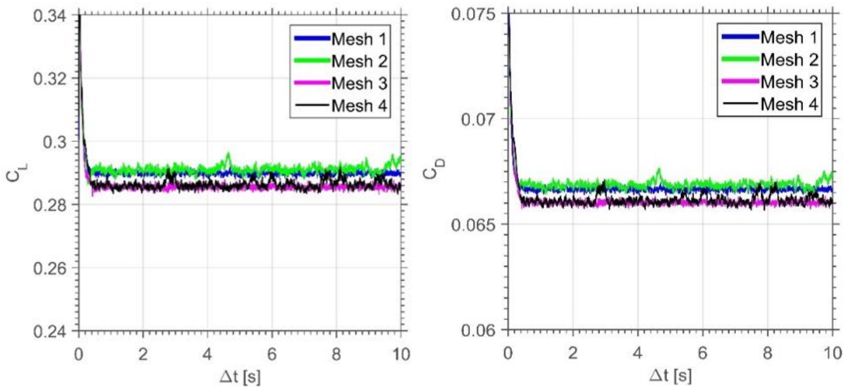

a)

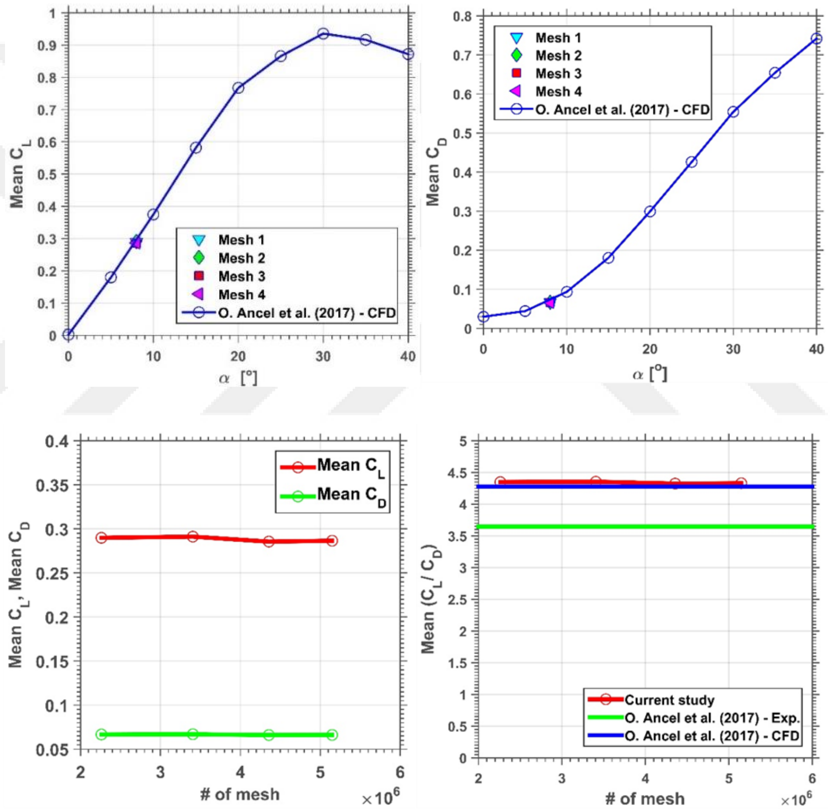

b)

Figure 3.11 a) Instantaneous C_L and C_D plots, $0s \le t \le 10s$, b) Mesh refinement study at $\alpha_0 = 8°$ (laminar flow, Δt=0.002s).

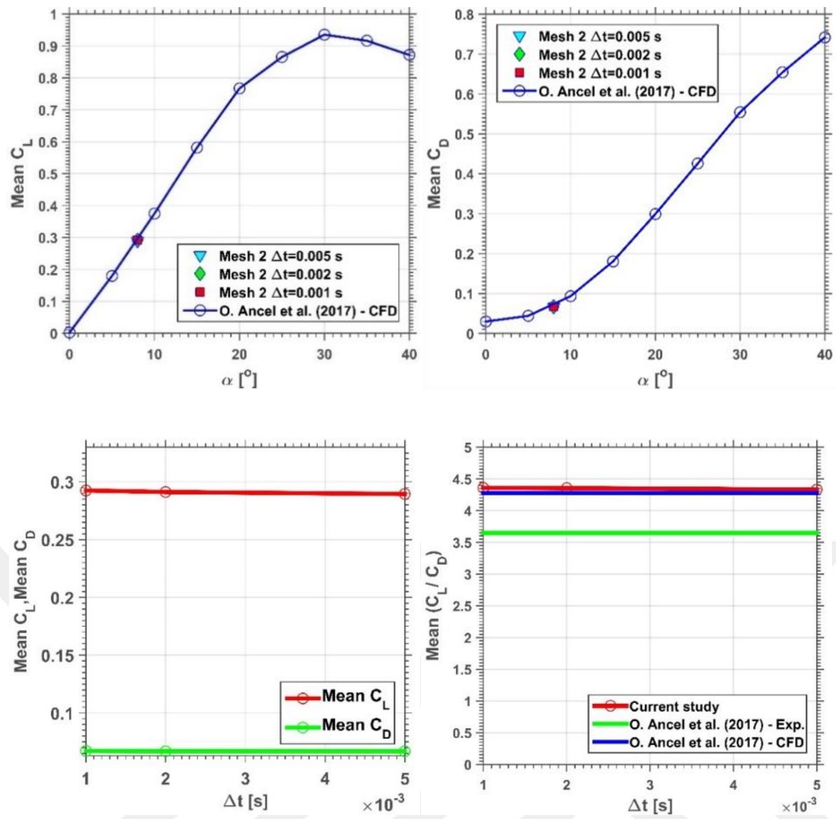

Figure 3.12 Time refinement study for time increments of $\Delta t = 0.001\ s, 0.002\ s$ and $0.005\ s$ at $\alpha_{\circ}$=8°.

CHAPTER 4

UNSTEADY AERODYNAMIC ANALYSIS OF STATIONARY MONARCH WING

4.1 Unsteady Aerodynamics Analysis of Stationary Wing

4.1.1 Monarch butterfly wing analysis

3D unsteadies numerical simulations have been carried out for the Monarch butterfly museum pinned model. The wing has been positioned at different angles of attack. Coherence with the literature has been verified under the same simulation conditions. The mean lift and drag coefficients, pressure distributions, skin friction with separation point, and wake patterns downstream of the wing model are discussed in detail. At low Reynolds numbers $10^4 < Re < 10^5$, thin flat plate models demonstrate different flow characteristics from the conventional wings based on relatively thick airfoil shapes. The literature shows that the characteristics of lift and drag are improved when the thickness of the wing section is decreased [41]. At low Reynolds numbers, the flow is accepted as laminar, and a possible transition to the turbulent flow regime can occur through increased angles of attack and Reynolds numbers. Therefore, a key term might be required, the laminar-turbulent transition model, which is coupled with a turbulence model [41] to improve the numerical solution for the prediction of the flow transition physics. In the current study, until a 10° angle of attack, the flow simulated with the laminar model is found to be close to the turbulent model. For angles of attack higher than 10°, the transition SST 4-equation turbulence-transition model is utilized for the simulations. The results are compared with the experimental and numerical results documented in the available literature [13], where their model employs ANSYS CFX, SST $k - \omega$, turbulence model. The analysis conducted for $0s \leq t \leq 10s$ with laminar flow proves inadequate to capture fluctuations at higher angles of attack.

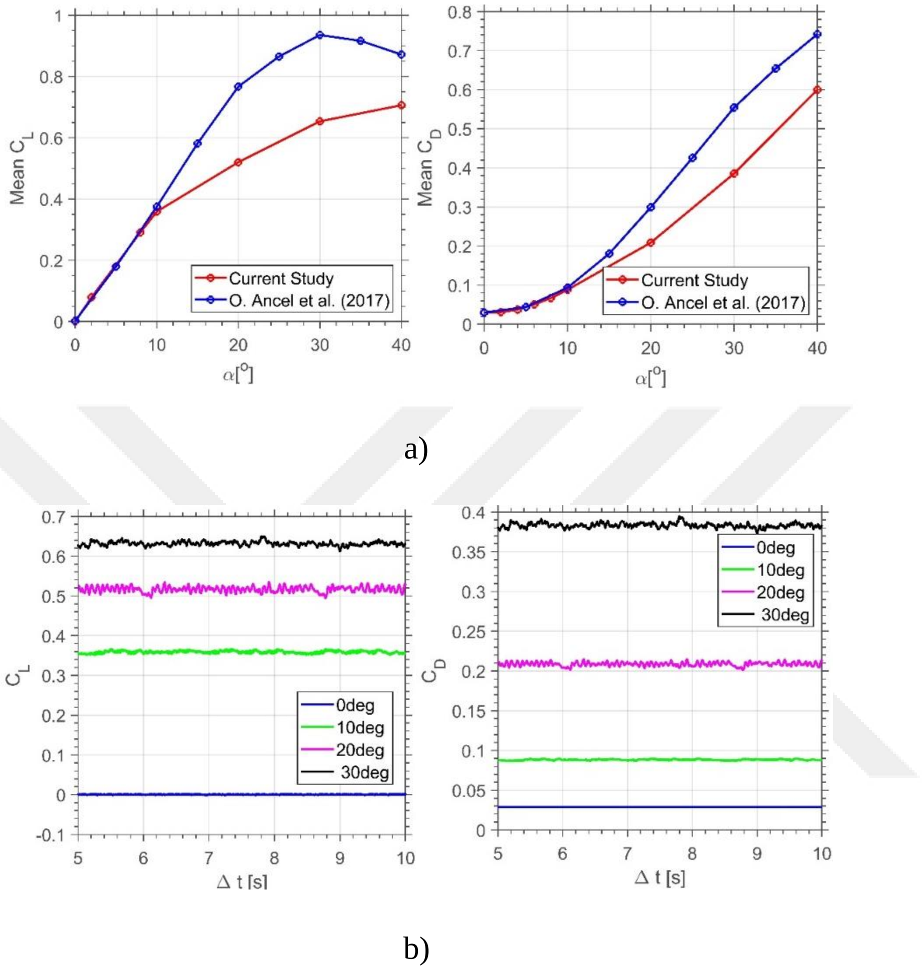

Figure 4.1 Laminar flow a) comparison with [13], b) instantaneous C_L and C_D values $5s \leq t \leq 10s$.

$0s \leq t \leq 10s$ analysis with transition SST flow TI 10% can capture fluctuations at higher angles of attack.

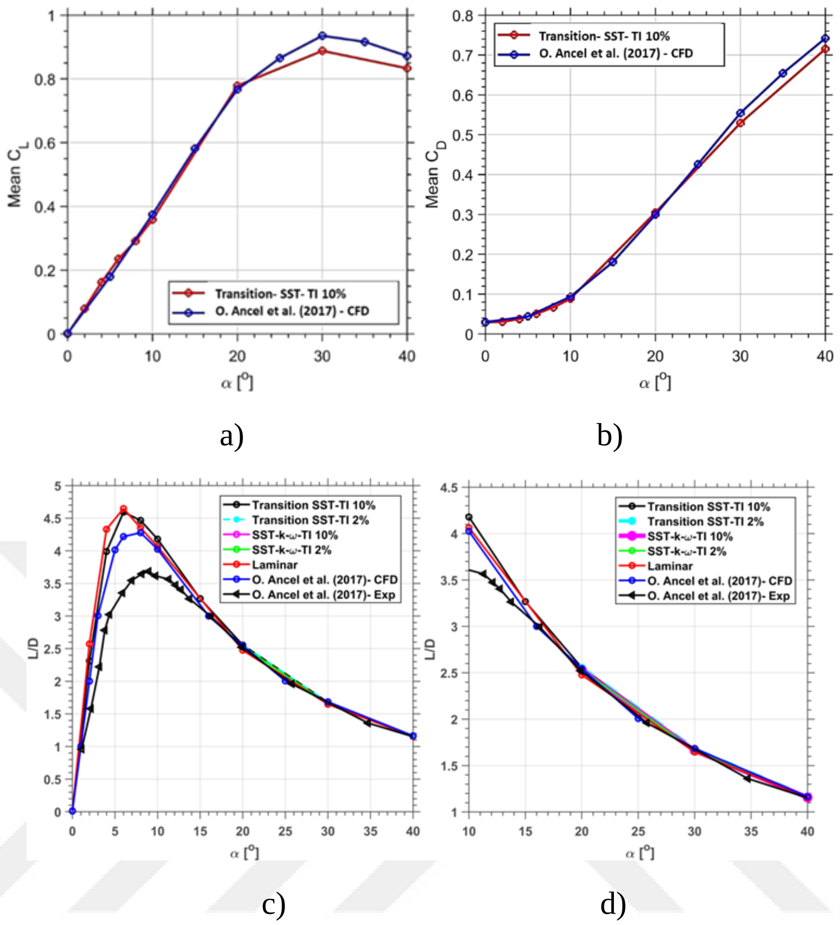

Figure 4.2 Different turbulence models comparison.

The mean aerodynamic force coefficients of 3D Monarch butterfly wings are compared with the available literature data [13],[14] for angles of attack from 0° to 40° (Figure 4.1 and Figure 4.2). For the angles from 0° to 40° degrees, the solutions are obtained both with laminar and turbulence models. The turbulence models selected are k-ε and Transition SST. The results are also compared with 2% and 10% turbulence intensities (TI) at the free stream (Figure 4.2). Among the simulations, the least error of the aerodynamic coefficients is obtained at the Transition SST simulations with TI = 10%. Therefore, the current study is continued with the transition SST 4-equation turbulence-transition model with TI = 10%. Moreover, all simulations are performed until t = 10s with a time increment of Δt = 0.002s. The mean aerodynamic values are obtained by averaging in the time interval of 5s ≤ t ≤10s.

Considering Figure 4.2, the wing achieves the stall angle at around 30° angle of attack where the flow separates from the upper surface of the wing, resulting in reduced lift. The leading-edge vortex (LEV) at a low Reynolds number readheres to the wing during the entire upstroke, resulting in a strong lift, which is referred to as the delayed-stall mechanism [42],[43],[44]. The LEV's circulation increases the vortex and thus the lift. A dynamic stall is one in which a wing can fly at high angles of attack and generate extra lift before the stall [43]. In the results found by Ancel et al. [13], a discrepancy is observed between experimental and numerical studies. They denoted that this variation results from a long rod used in their wind tunnel experiments to amplify the force measurements, and this experimental setup creates a number of small vibrations. On the other hand, in numerical simulations, the vibration effects are omitted and not included in the numerical method. The lift and drag curve predictions of the current study match well with the numerical results obtained by Ortega Ancel et al. before the stall angle of α=30°.

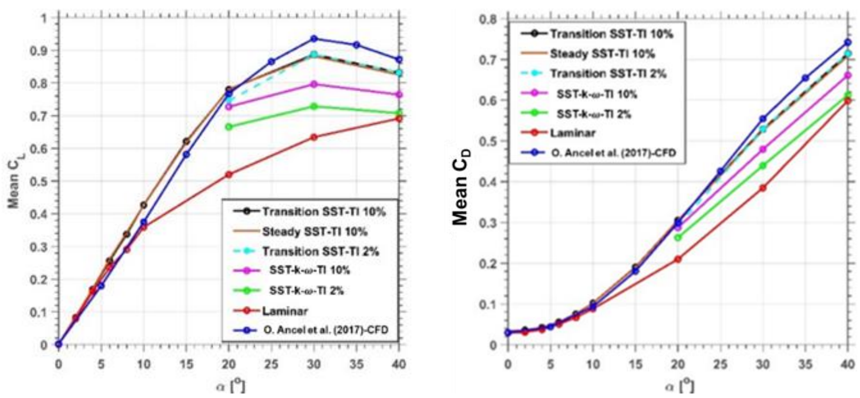

Figure 4.3 Different flow model comparisons a) ($\bar{C}_L$), b) ($\bar{C}_D$).

In addition, the steady analysis is compared with the unsteady results (in Figure 4.3). The results are close to the CFD results of the reference study. The aerodynamic efficiency of the wing is defined by the lift-to-drag ratio. The L/D ratio is compared with the data of Ancel et al. [13] and the highest efficiency is obtained between 6°

and 8° angles of attack (Figure 4.2c). Above these angles, the Monarch butterfly wing shows a decreased performance. The results from the current study and the studies done by Ancel et al. [13] show minor differences attributed to a slight difference in wing geometry. Consequently, the mean lift and mean drag coefficient, the L/D ratio, and pressure contours also vary due to geometric discrepancies. In the current study, for all angles of attack, the time average mean flow data is calculated at the interval of $5s \leq t \leq 10s$.

Mean static pressure and the 3D vorticities are presented for the Monarch butterfly wing in Figure 4.4 and Figure 4.5. The pressure distribution on wing surfaces varies significantly with the angle of attack. In Figure 4.5, the Q-criterion is colored by non-dimensional z-vorticity magnitudes. As the angle of attack increases, the vortices on the upper (counterclockwise) and the lower (clockwise) surfaces of the wing increase in intensity. It can be observed that as the angle of attack increases from 8° to 40°, the intensity of the leading-edge vortex (LEV) increases abruptly. The details of the vorticity contours are also presented at spanwise planes. When the angle of attack increases, the streamwise vorticity (z-vorticity) from the root plane to the tip plane becomes more dominant. The flat plate-like wings exhibit significantly different flow characteristics than the conventional wings with the same flow regime ([26]). As shown in Figure 4.6, the wing is divided through a spanwise direction into five planes from root to tip in order to visualize the mean velocity streamlines, the pressure distribution, and skin friction values at these planes to observe the three-dimensional variation of these parameters.

At α=0° and α=2° angles of attack, both upper and lower surfaces of the wing show low mean static pressure differences resulting in low lift values as expected (Figure 4.4a-b). The leading edge at these angles of attack is covered by small, attached vortices (Figure 4.5a-b).

At α=8°, the tip vortex from the forewing and trailing edge vortex are starting to develop and the leading-edge vortex starts to partially detach from the upper surface.

The most distinct characteristic being the separation bubbles generated at the near leading edge is shown as a big pressure jump in mean static pressure contours in Figure 4.4c. A small separation bubble around the leading edge of the Monarch butterfly is observed at $\alpha=8°$ as shown in Figure 4.5c and also in Figure 4.7a, Figure 4.8a, and Figure 4.9a. When air flows around the leading edge, it passes above the trapped vortex and is dragged in by the vortex's lower pressure, which produces lift. As shown in Figure 4.5c, the separation at the wing's upper surface corresponds to a growing leading-edge vortex (LEV). Thereafter, at higher angles of attack, much larger vortices are formed both in size and magnitude. The leading-edge vortex (LEV) helps to improve lift by the use of a delayed stall. It is created and fed by the separation of the fluid from the leading edge, and it flows along the wing semi-span, beginning at the root and working its way to the tip where it meets the wingtip vortex, eventually producing a shedding wake. The mean leading-edge vortex separates and reattaches toward the wing's trailing edge; thus, the pressure difference of the Monarch wings can be preserved at a low Reynolds number, and more lift is provided at higher angles of attack (Figure 4.5)

Growing leading-edge vortex (LEV) with an increasing angle of attack, as shown in Figure 4.5, can result in the generation of a strong suction region on the upper surface of the wing (Figure 4.4).

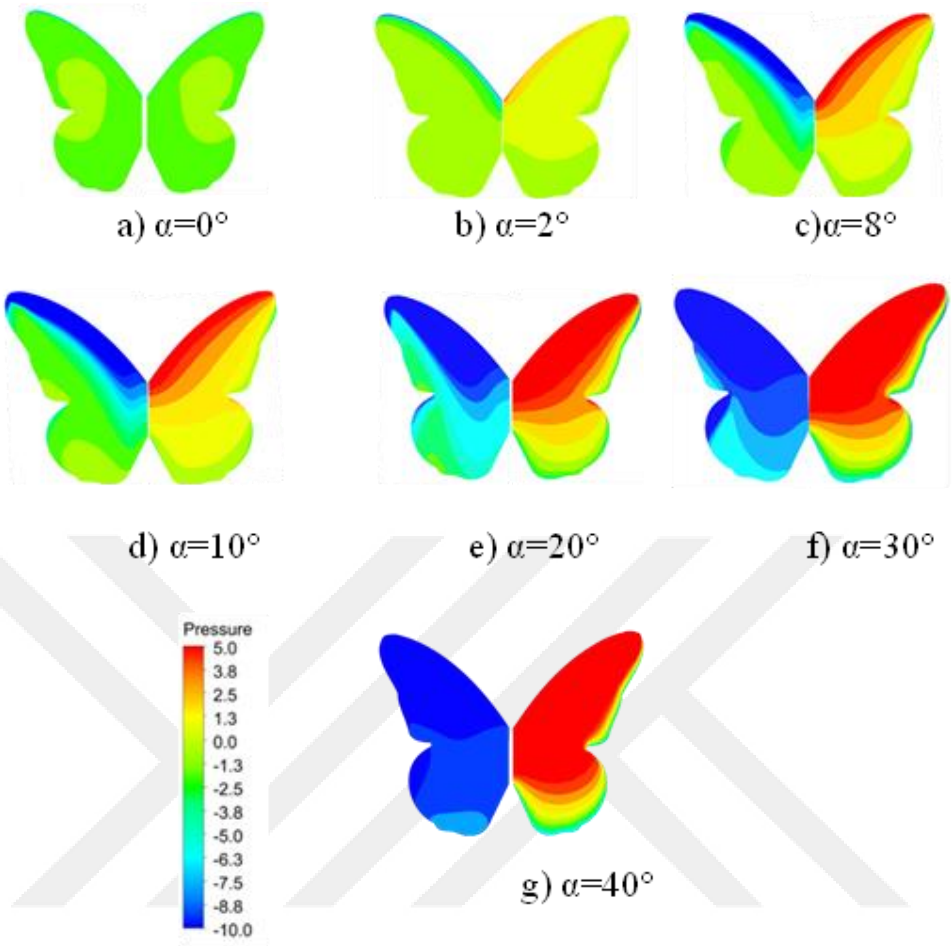

Figure 4.4 Mean static pressure contours at the upper surface (left wings) and lower surface (right wings) at different angles of attack.

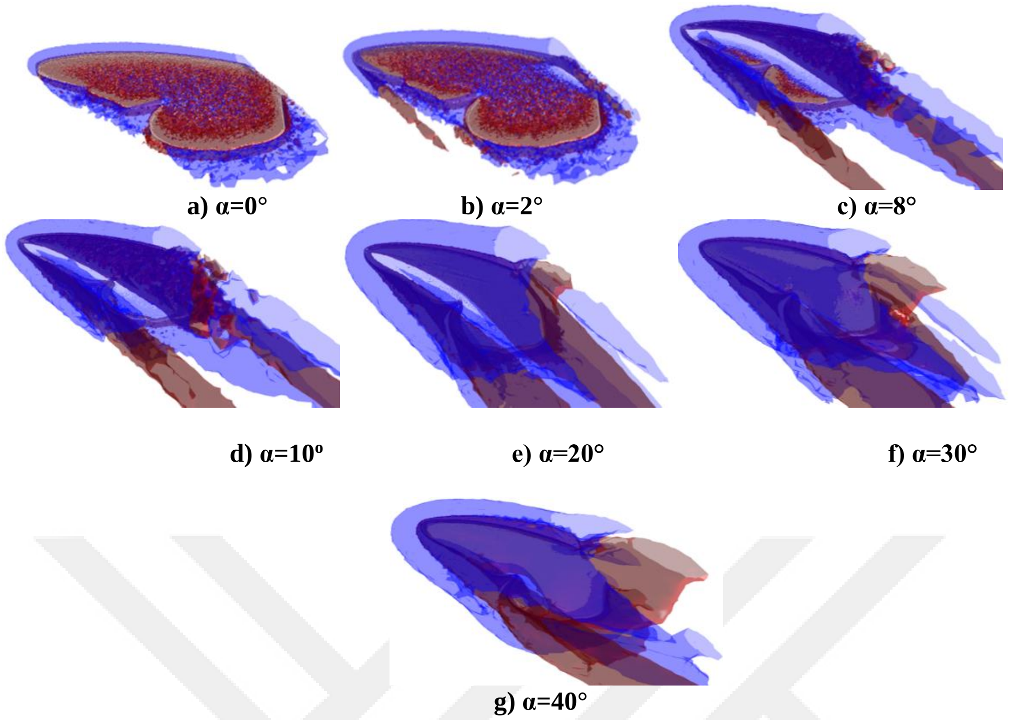

Figure 4.5 Iso-Q contours (colored to indicate sign; red is positive, and blue is negative) on the Monarch wing at different angles of attack.

Close to the stall angle of attack of α=30°, the lift reaches its maximum value. The leading-edge vortex gradually detaches from the wing's upper surface from the AA' plane (Figure 4.7b) until EE' plane (Figure 4.10b). The LEV is observed to reattaches close to the mid-chord length, at CC' plane as seen in Figure 4.9b. The same leading-edge vortex on the forewing grows progressively and it sweeps on the hindwing surface. Furthermore, the leading-edge vortex detaches and reattaches almost half of the BB' cross-section, which is on the forewing surface, on the other hand, the velocity streamlines flow over the upper surface of the hind wing surface without any vortices (Figure 4.8b). In this section, in two dimensions, the front wing and hind wing are seen to be in tandem positions, so the hind wing is at the wake of the front wing of the butterfly. The intermittent geometry through the BB' line, the flow might be disrupted, and the main LEV might not be able to grow like on the CC' and DD' planes as shown in Figure 4.10b and Figure 4.11b. Thus, both fore- and hind- wings are observed to have separated flows on their upper surfaces.

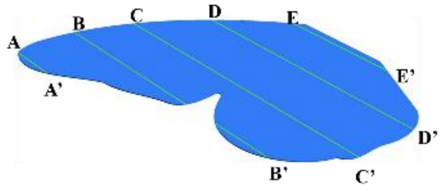

Figure 4.6 Monarch wing presented at five spanwise planes from root to tip.

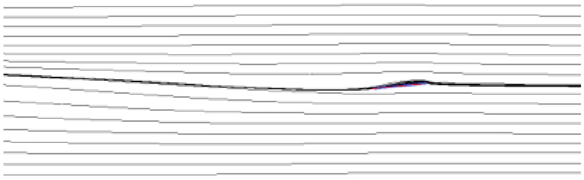

a)

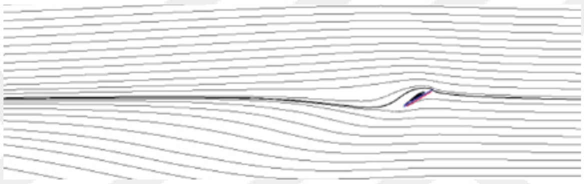

b)

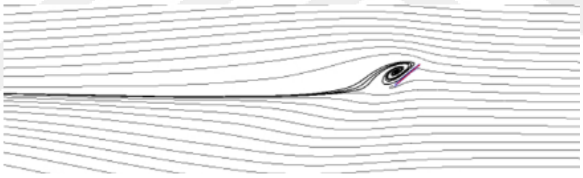

c)

Figure 4.7 Mean velocity streamlines at a) α = 8°, b) α = 30°, and c) α = 40° (along AA').

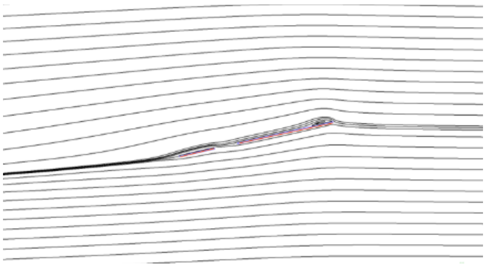

a)

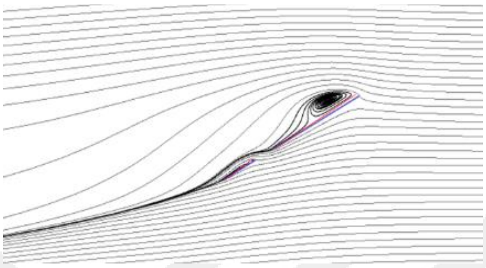

b)

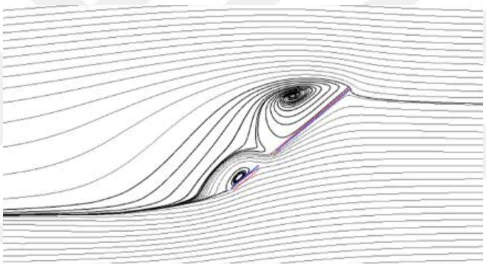

c)

Figure 4.8 Mean velocity streamlines at a) α = 8°, b) α = 30°, and c) α = 40° (along BB’).

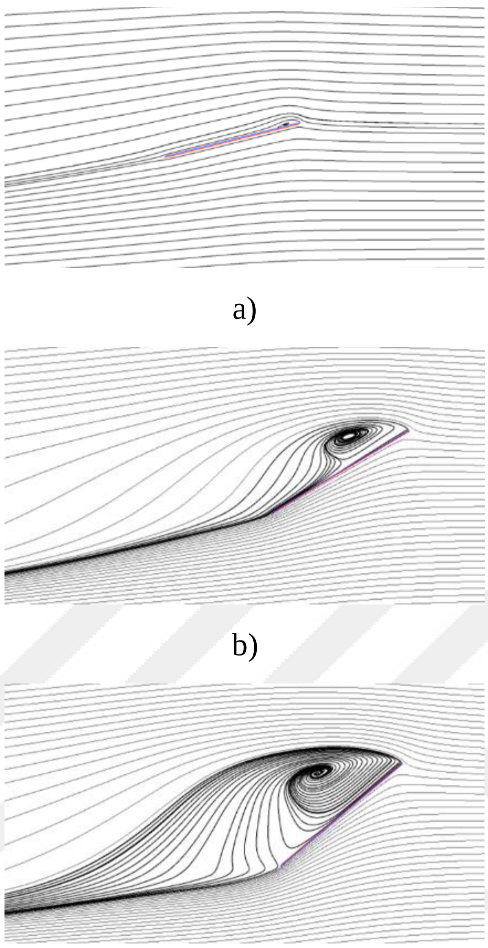

a)

b)

c)

Figure 4.9 Mean velocity streamlines at a) α = 8°, b) α = 30°, and c) α = 40° (along CC’).

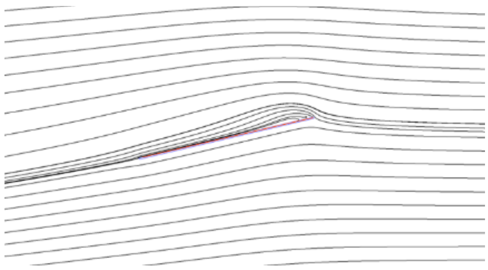

a)

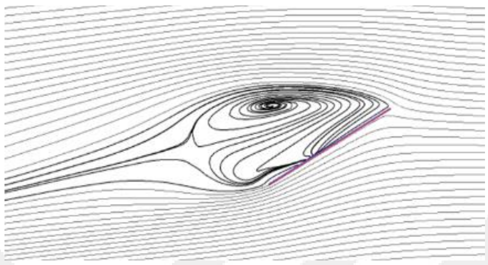

b)

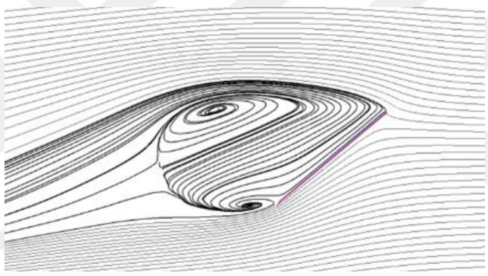

c)

Figure 4.10 Mean velocity streamlines at a) α = 8°, b) α = 30°, and c) α = 40° (along DD').

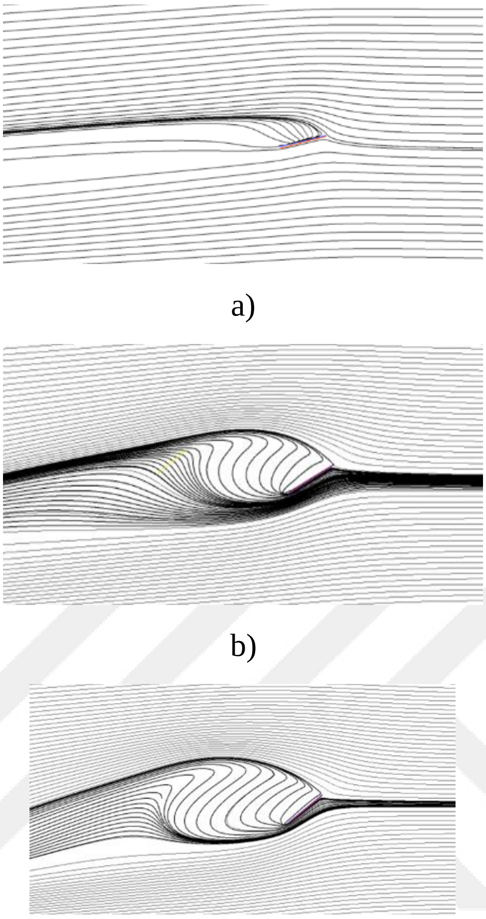

a)

b)

c)

Figure 4.11 Mean velocity streamlines at a) α = 8°, b) α = 30°, and c) α = 40° (along EE').

At α=40^{o} angle of attack, these vortex structures are observed to be more dominant (Figure 4.5g). The vortex almost entirely detaches from the upper surface of the wing and does not reattach to the wing before the trailing edge as shown in Figure 4.9c, causing the lift to drop as shown in Figure 4.2a. Meanwhile, a trailing edge vortex (TE) is observed at the trailing edge on DD' plane as shown in Figure 4.10c. Meanwhile, the separation vortex on the upper surface causes the lift to decrease slightly compared to the maximum lift value. Moreover, at BB' cross-section, the leading-edge vortex completely breaks away from the forewing. Moreover, a flow reversal occurs at the trailing edge, and a secondary vortex grows on the upper surface of the hindwing (Figure 4.8c).

Mean C_f and C_P distributions

The pressure coefficient and the skin friction coefficient distributions on the wing surface are investigated to understand the flow characteristics at pre-stall (α=8°), close to stall (α=30°), and the post-stall (α=40°) angles (from Figure 4.12 to Figure 4.14). As shown in Figure 4.6, the flow mean pressure and skin friction distributions are presented at five different spanwise planes from AA' to EE' from tip to root.

At the low angle of attack, flow is attached to the wing surface except for a narrow separation region near the leading edge and the pressure distribution curves confirm the trend of the separation process with a short length on the pressure plateau where a small separation bubble grows at the leading edge of the wing (Figure 4.12). The separation and reattachment locations are obtained from the skin friction coefficient (C_f) curves (Figure 4.16- Figure 4.18) for different angles of attack. The pressure distribution at α=30° over the upper surface of the Monarch wings shown in Figure 4.13 also indicates the presence of the flow separation emerging in the upper surface. Moreover, the leading-edge vortex results in a rise in the lift coefficient. From the pressure coefficient plots, the most lift on the tip of the wing is generated in the region close to the leading edge at α=30°.

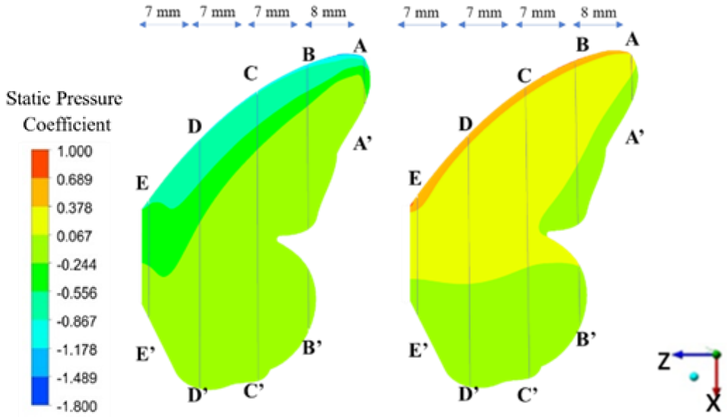

a) Upper surface of the wing b) Lower surface of the wing

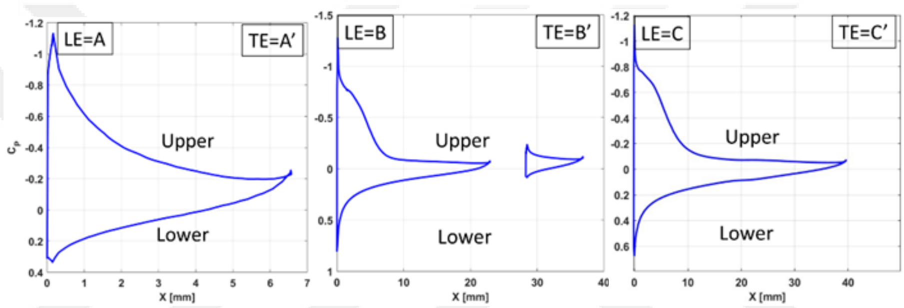

c) along AA’ d) along BB’ e) along CC’

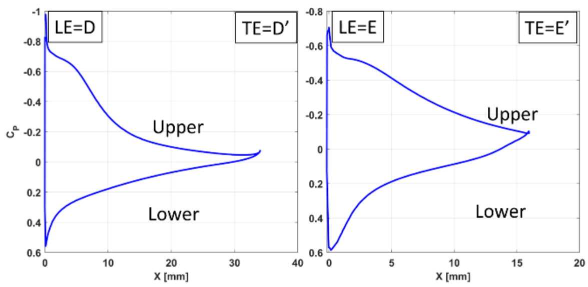

g) along DD’ h) along EE’

Figure 4.12 Monarch butterfly wing’s mean pressure coefficient distributions at $\alpha=8^0$.

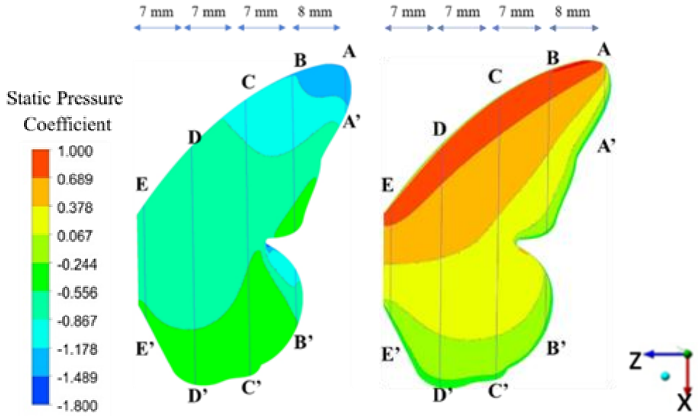

a) Upper surface of the wing b) Lower surface of the wing

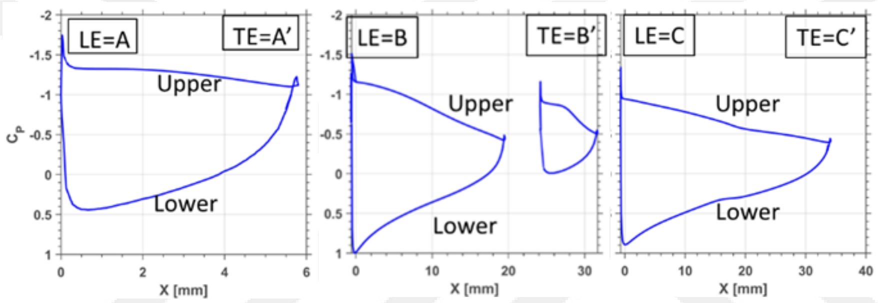

c) along AA' d) along BB' e) along CC'

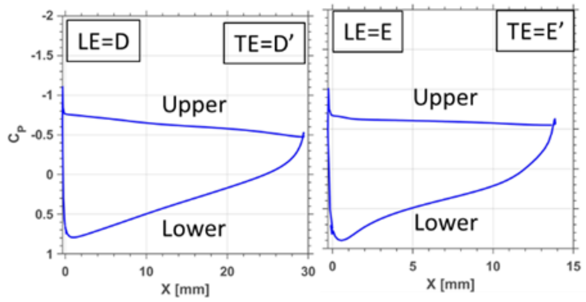

g) along DD' h) along EE'

Figure 4.13 Monarch butterfly wing's mean pressure coefficient distributions at $\alpha=30^0$.

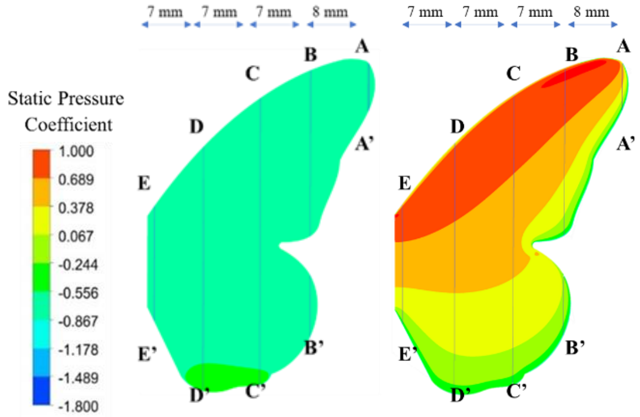

a) Upper surface of the wing b) Lower surface of the wing

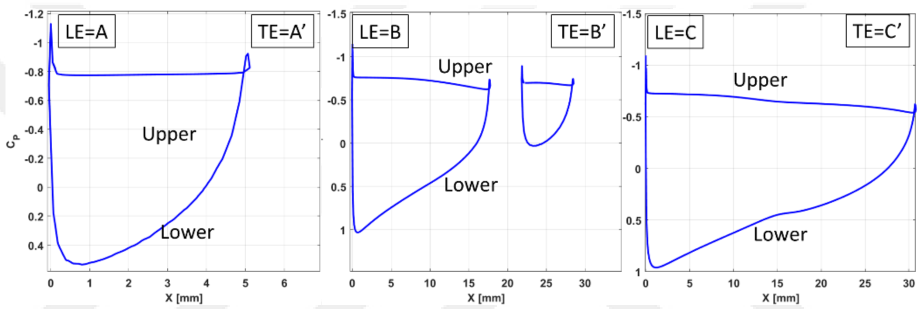

c) along AA' d) along BB' e) along CC'

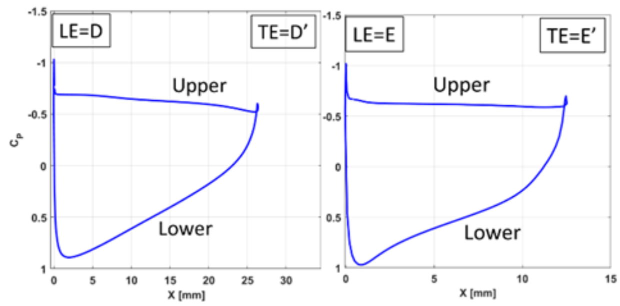

g) along DD' h) along EE'

Figure 4.14 Monarch butterfly wing's mean pressure coefficient distributions at $\alpha=40^0$.

At the higher angle of attack of 40°, the pressure distribution shows a straight pressure plateau where a large separation vortex is shown on the upper surface of the wing (Figure 4.14). The LE line is investigated at three angles of attack. At α=30°

and α=40°, C_p changes are found indeed to be more constant compared to a lower angle of attack of α=8°. As the angle of attack increases, uniformity of the lift (ΔC_p) over the wing leading edge seems to increase. C_p variation on the upper leading edge and lower leading edge are shown in the figure below Figure 4.15. In Figure 4.17, the skin friction coefficient shows the separation of the flow on the wing at 30° angle of attack. The separation starts from the leading edge of the wing and grows in size and magnitude on the upper surface. At α=30° angle of attack stronger wingtip vortex is observed. (Figure 4.17g).

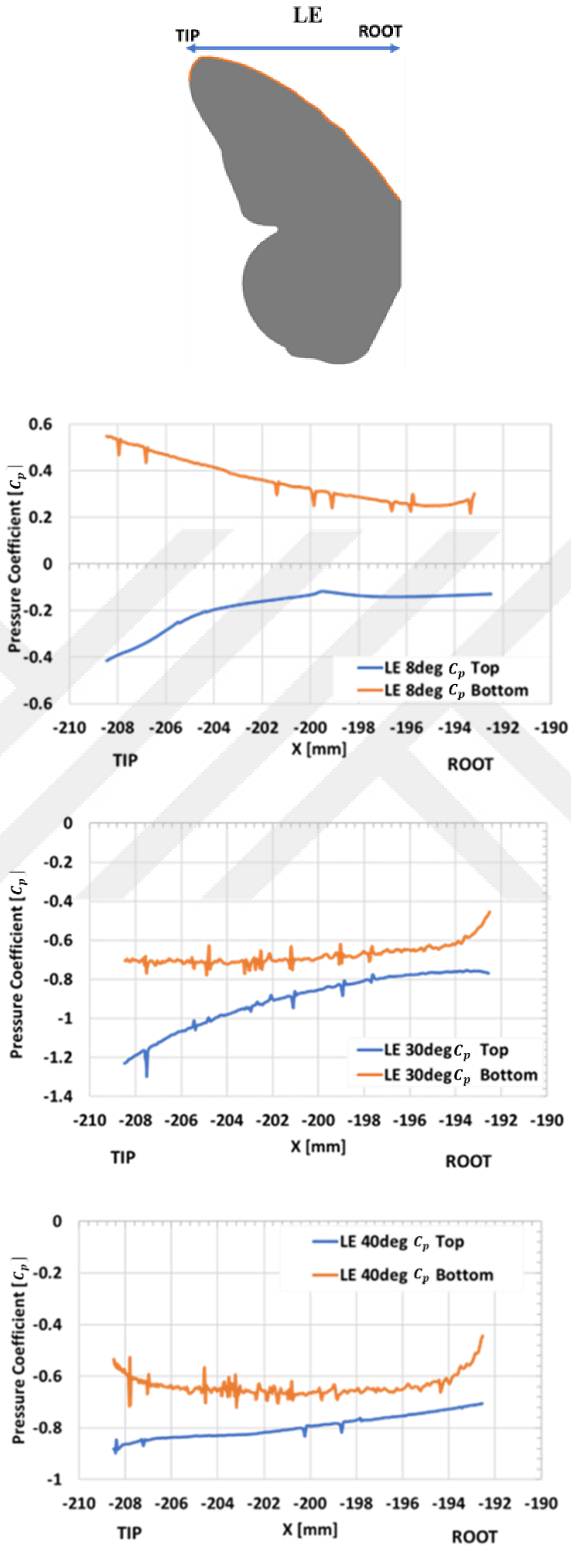

Figure 4.15 C_p distribution along the leading edge of the wing from root to tip.

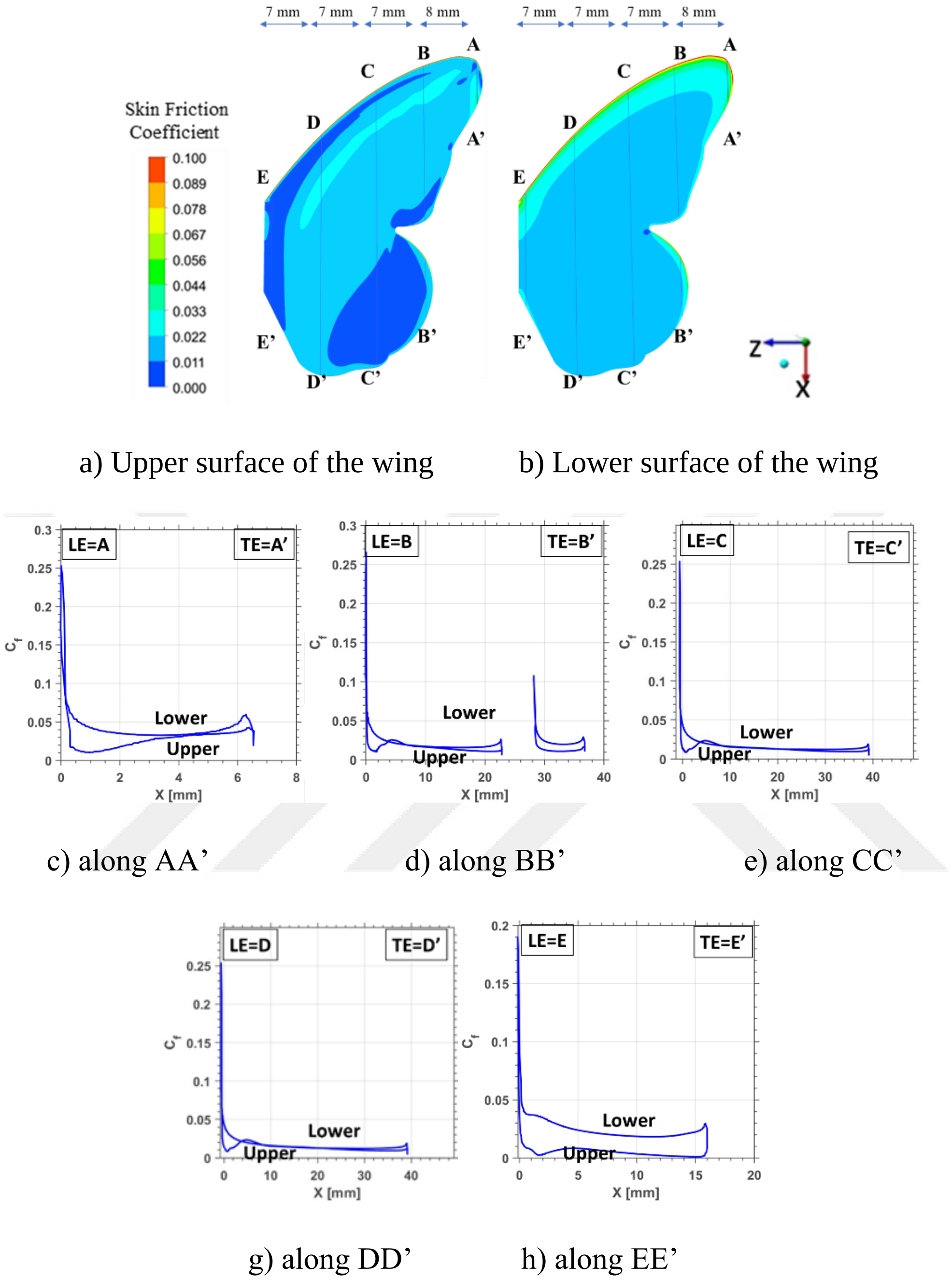

Figure 4.16 Monarch butterfly wing's mean skin friction coefficient distributions at $\alpha=8^0$.

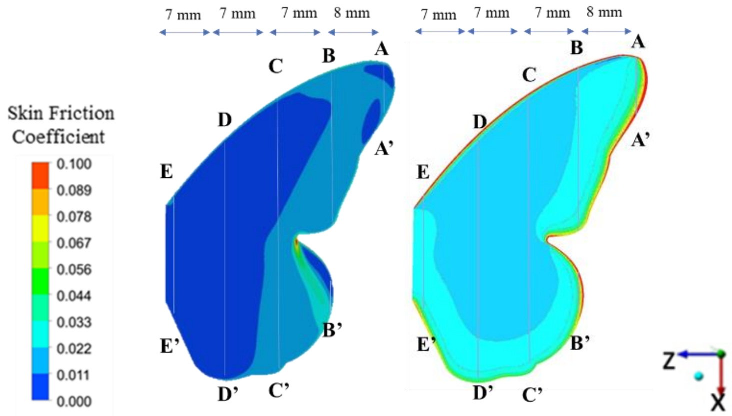

a) Upper surface of the wing b) Lower surface of the wing

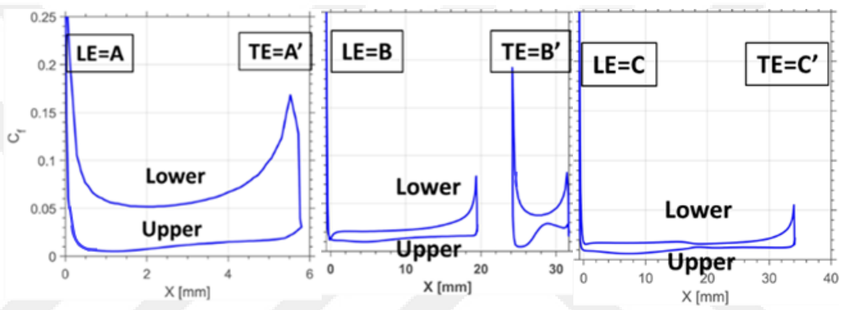

c) along AA' d) along BB' e) along CC'

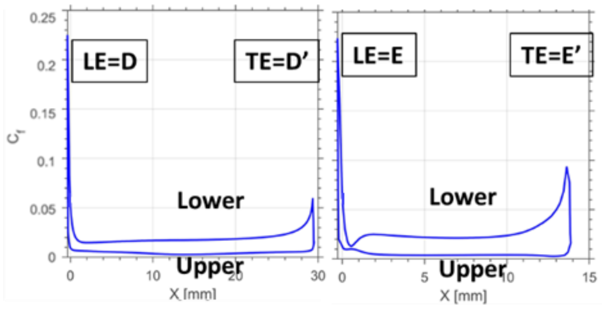

g) along DD' h) along EE'

Figure 4.17 Monarch butterfly wing's mean skin friction coefficient distributions at $\alpha=30^0$.

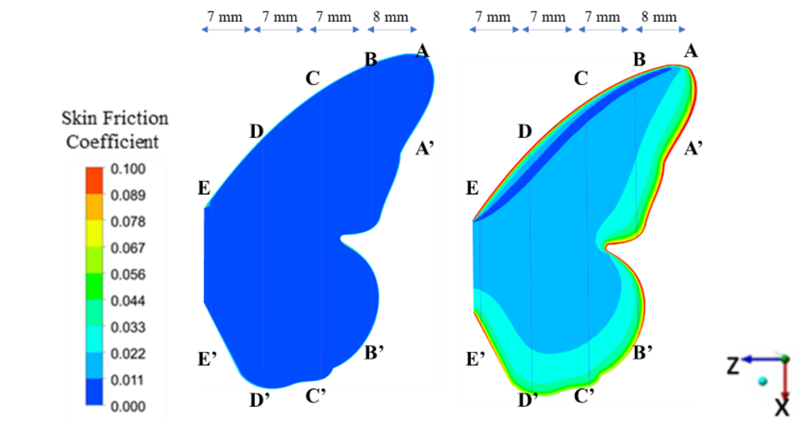

a) Upper surface of the wing b) Lower surface of the wing

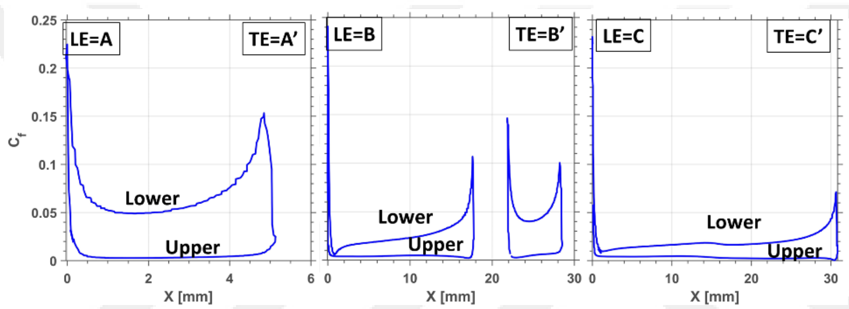

c) along AA' d) along BB' e) along CC'

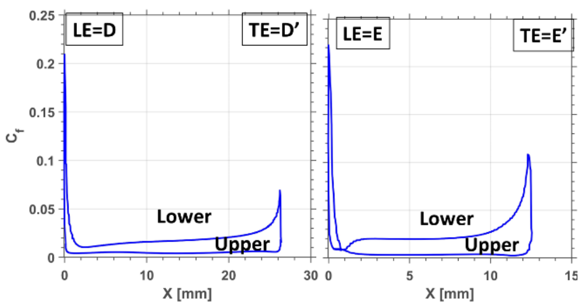

g) along DD' h) along EE'

Figure 4.18 Monarch butterfly wing's mean skin friction coefficient distributions at $\alpha=40^0$.

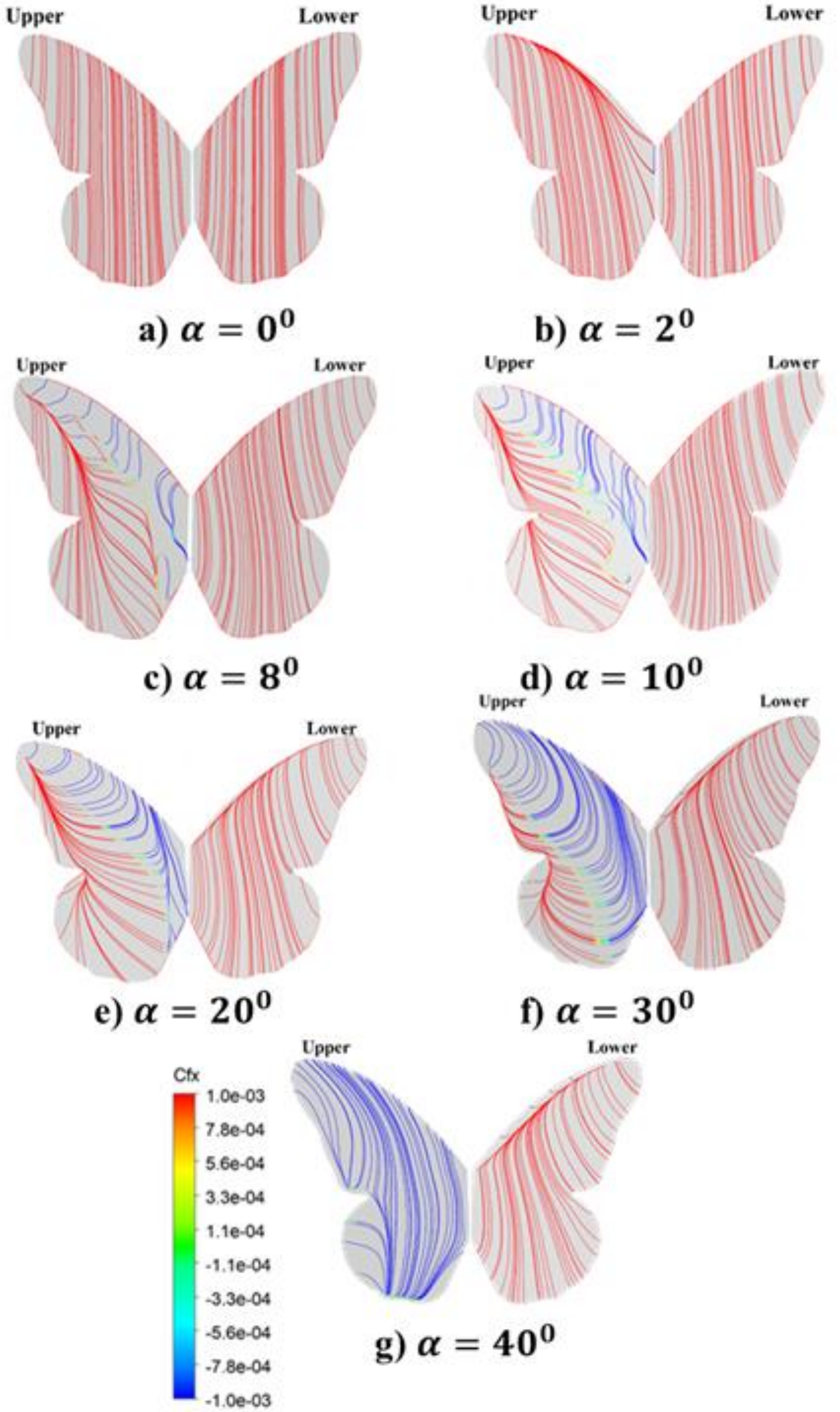

Figure 4.19 The skin friction lines colored with non-dimensional x-shear stress (C_{fx}) on the upper and lower surface of the wing at different angles of attack.

The skin friction lines are drawn on the upper and lower surfaces of the wing at different angles of attack. The lines are colored with the non-dimensional shear stress in the x-direction (C_{fx}) where the negative values with blue color represent reverse flow regions on the upper and lower surfaces of the wing. Reverse flow is observed above 8^o angle of attack on the upper surface and as the angle of attack increases this separation moves from the leading edge towards the trailing edge. At α=40^o, the whole upper surface is observed to have negative C_{fx} values (Figure 4.19g). The separation is observed close to the leading edge at the lower surface of the wing for angles of attack of 20^o to 40^o as shown in Figure 4.19.

CHAPTER 5

EXPERIMENTAL AND NUMERICAL UNSTEADY AEROELASTIC EFFECT ANALYSIS OF WING MODEL TRIGGERED WITH PIEZOELECTRIC MATERIAL METHODOLOGY

5.1 Unsteady Aerodynamics Analysis of Dynamic Wing

In the experimental studies some complicated deformations can be observed on the wing models, and these cause challenges that could not be overcome by computational methods. Due to inaccurate simulation results, an alternative strategy is required to achieve the complexities of those deformations.

In this thesis, unique morphological data regarding the piezoelectric actuated wing deformations are obtained experimentally through DIC system techniques [64]. These real deformations are subsequently employed as inputs to incorporate aeroelastic effects within computational fluid dynamics (CFD) simulations. This method bypasses the need for detailed computational structure modeling since the wing's morphological data are acquired in advance.

The experimental system in this study employs two distinct measurement methods. One method records force/torque data, while the other captures 3D dynamic deformations of the wing. All experiments are conducted under zero free stream velocity and zero incidence conditions for all wings. Specifically, the flapping frequencies are set to 9.6 Hz for rectangular wings and 12.1 Hz for hummingbird wings [65]. A comprehensive dataset for the Monarch butterfly is derived from these experiments, forming a conclusive study. Subsequently, a similar study is replicated using this dataset.

The following subsections detail the presentation and analysis of the results from these experimental systems, comparing them with the computational fluid dynamics (CFD) outcomes. The study concludes by summarizing key points derived from the analysis.

5.1.1 Piezoelectric actuated Rectangle wing and Rufous hummingbird wing

DIC (Digital Image Correlation) technology, known for its image correlation nature, measures wing deformation. It is highly suitable for assessing piezoelectrically actuated flapping wing deformations due to its non-intrusive nature, allowing it to capture real-time results for multiple measurement positions on a specimen's surface. The obtained data can be directly transferred to testing devices, data acquisition units, or processing software.

In a typical setup, around 12-13 images are captured in one cycle flapping motion for the rectangular wing (9.6 Hz), while 9-10 images are taken for the hummingbird wing (12.1 Hz). Due to the camera's maximum image rate per second limitation, the image capture rate is set at 120.0 Hz with a shutter time of 5 seconds. Consequently, the maximum number of images obtained is 600. Following the postprocessing of the evaluated images, large vertical displacements can be observed in the wings. This observation indicates that the piezoelectric-actuated wings successfully mimic the flapping motion observed in biologically inspired wing models.

The system captures the initial image as the wing motion rises, followed by its movement along a sinusoidal path (shown in Figure 5.1a).

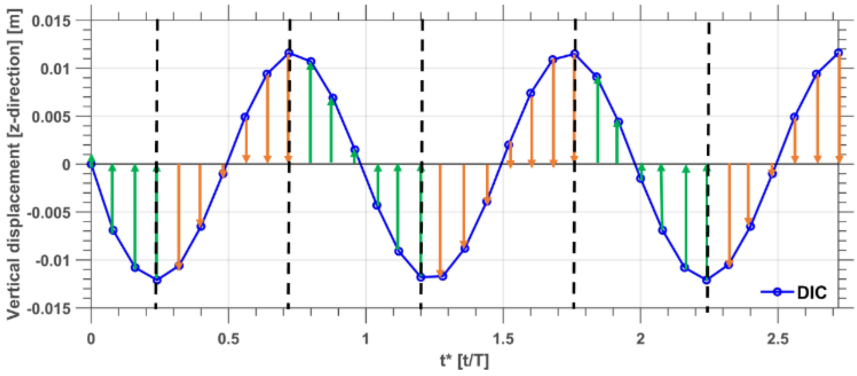

a)

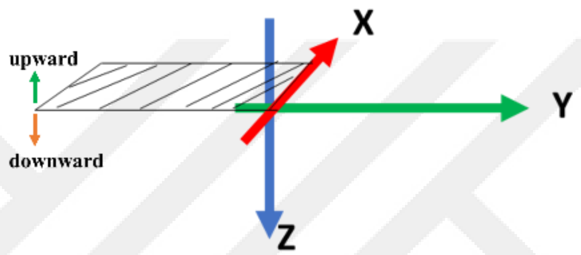

b)

Figure 5.1 DIC vertical displacement a) Rectangle wing (green arrows: upward, orange arrows: downward), b) wing position and its coordinate system.

Figure 5.3 and Figure 5.4 illustrate the curves representing kinematic values obtained from DIC results for the rectangular wing and Rufous hummingbird wing. Moreover, velocity and acceleration curves depicting the flapping motion are acquired through the DIC system. The velocity and acceleration curves can be formulated as the first and second derivatives of displacement equations, respectively. Once the displacement equation is mathematically defined, these expressions can be interchanged among the values.

$$d_z(t) = 0.0119 * sin(60.5770t - 3.0910)$$

$$v_z = d_z{}'(\mathrm{t}) = 0.7209 * cos(60.5770t - 3.0910) \quad (5.1)$$

$$a_z = d_z{}''(t) = -43.6679 * sin(60.5770t - 3.0910)$$

The empirical parameters given in Equation 5.1 are obtained from the displacement curve of the rectangular wing captured by the DIC system. Thus, the equations in (5.1) are derived from the velocity and acceleration curves.

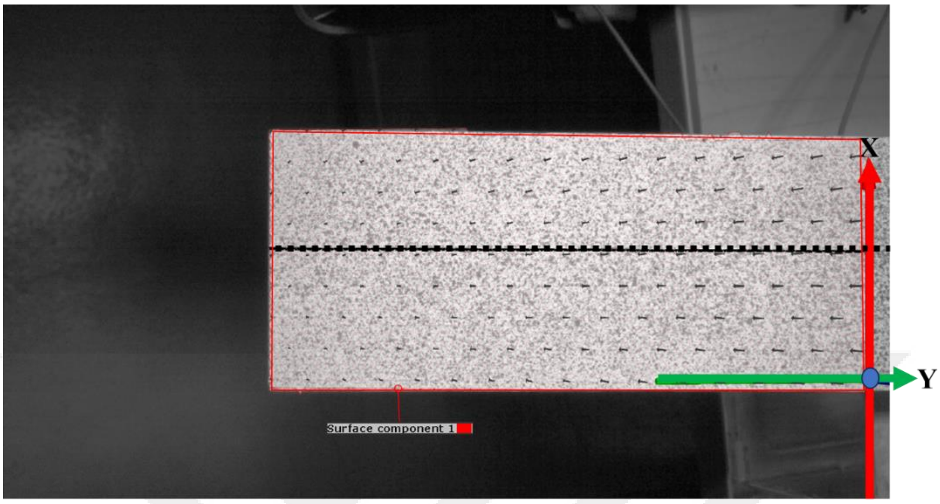

Figure 5.2 Capturing deformation values with the DIC system.

The software, illustrated in Figure 5.2, calculates values based on the image correlation of the wing surfaces. Specifically, values along the spanwise line at the semi-chord location are extracted from the wing surfaces. These kinematic properties are acquired for each timestep during the flapping motion, and subsequent curves are generated using this information.

In Figure 5.3 and Figure 5.4, the time-dependent plots of the data obtained from the rectangle wing and the hummingbird wing experiments are observed. Concerning the coordinate system (Figure 5.1b) provided, the values indicated by green arrows in the displacement curve move upward. Furthermore, when comparing the velocity and displacement curves given in Figure 5.3 and Figure 5.4, it is observed that when the wings reach their maximum displacement values, the velocity tends to approach zero. While, when examining the acceleration curve, it is noted that in instances where the wing reaches the maximum flapping angle and starts the reverse movement, the displacement and acceleration data points have opposite signs (when displacement is negative, acceleration is positive, or vice versa). The wing's acceleration is proportional to its negative displacement.

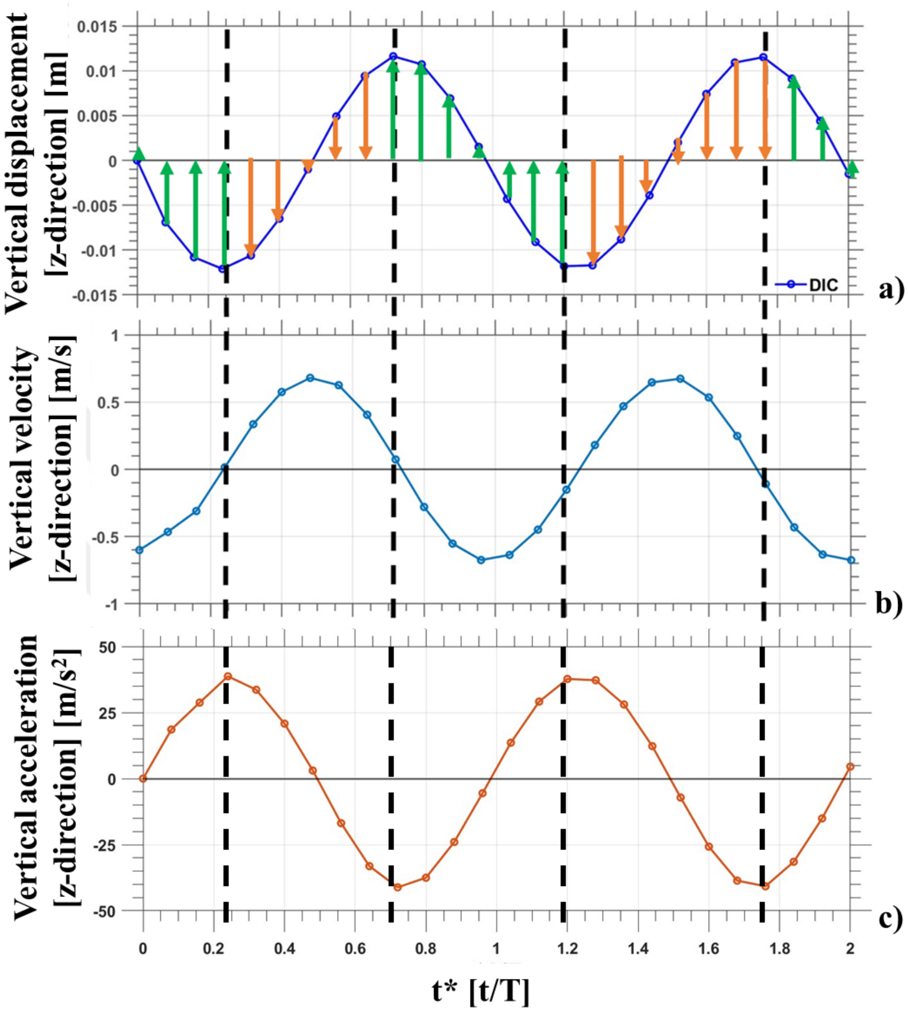

Figure 5.3 Kinematic properties of rectangle wing, a) d_z, vertical displacement, b) v_z, vertical velocity,c) a_z, vertical acceleration.

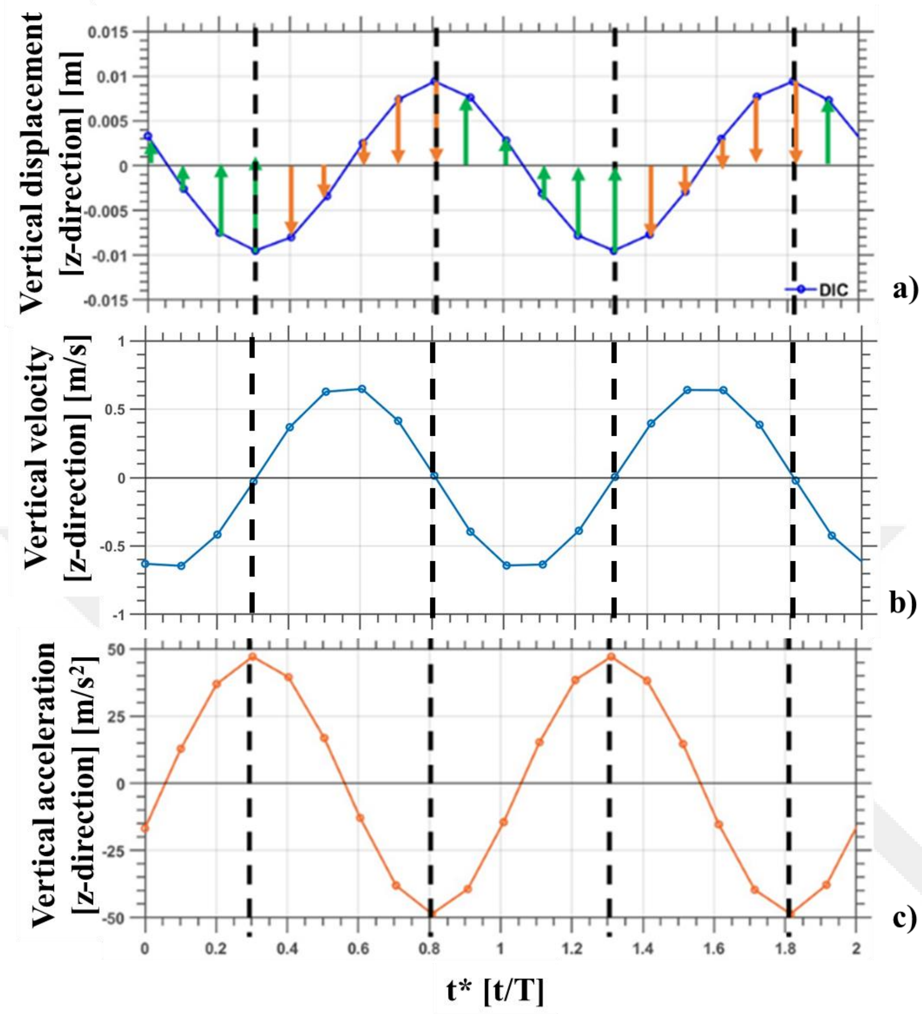

Figure 5.4 Kinematic properties of Rufous hummingbird wing, a) d_z, vertical displacement, b) v_z, vertical velocity,c) a_z, vertical acceleration.

Following the investigation of the characteristics of the wing deformations, the equation of the motion is obtained and subsequently integrated into the CFD user-defined function routine. Thus, the wings can perform the aeroelastic motion during numerical flapping wing simulations.

- **Displacement investigation of DIC and CFD**

In the computational part of the study, wing motion is given by user-defined subroutines (UDF function) by dynamic mesh motion. Thus, the aero-elastic effects can be visualized by simulation. The re-meshing technique is used for the dynamic mesh option in the FLUENT solver. A three-dimensional computational grid that comprises tetrahedral cells is solved by the Naiver-Stokes equations. At the beginning, a three-dimensional, double-precision pressure-based solver is adjusted for computation. Then, the second-order upwind and central differenced schemes are used for computing momentum and pressure, respectively. The flow is assumed to be laminar. In the hover case, as a reference value, air density is set to 1.225 kg/m^3 and the kinematic viscosity is assigned as 1.7894× 10^{-5} kg/m-s. Grid is adapted by smoothing method selection. For the sake of the generation of flapping motion, the user-defined function (UDF) is loaded and compiled. A simple periodic velocity profile equation of flapping wing motion (ω) is given by (Eq.5.2):

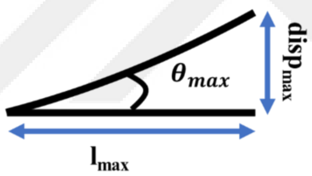

Figure 5.5 Schematic displacement motion.

$$\omega = \theta_{max} * 2 * \pi * f_{flapping} * \cos(2 * \pi * f_{flapping} * t) * \sqrt{x/l_{max}} \qquad (5.2)$$

As shown in Figure 5.5 where θ_{max} maximum flapping angle in radian, $f_{flapping}$ flapping frequency in Hz, x/l_{max} x- nodes coordinate divided by the length of the wing along the spanwise direction. The parameters are obtained from the outcomes of the DIC dynamic deformations.

To validate the CFD model, the displacement curves obtained from DIC and CFD are compared. The comparison shows a good agreement between DIC and CFD visualizations in terms of displacement, as depicted in Figure 5.6 and Figure 5.7.

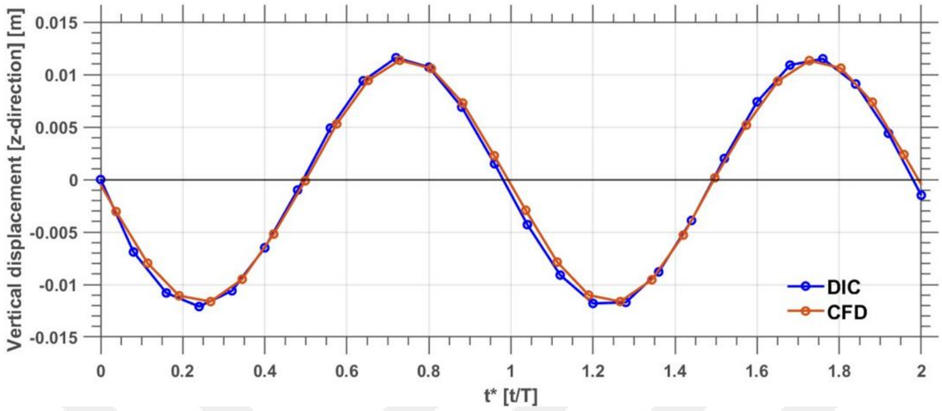

Figure 5.6 DIC and CFD displacement comparison for rectangle wing.

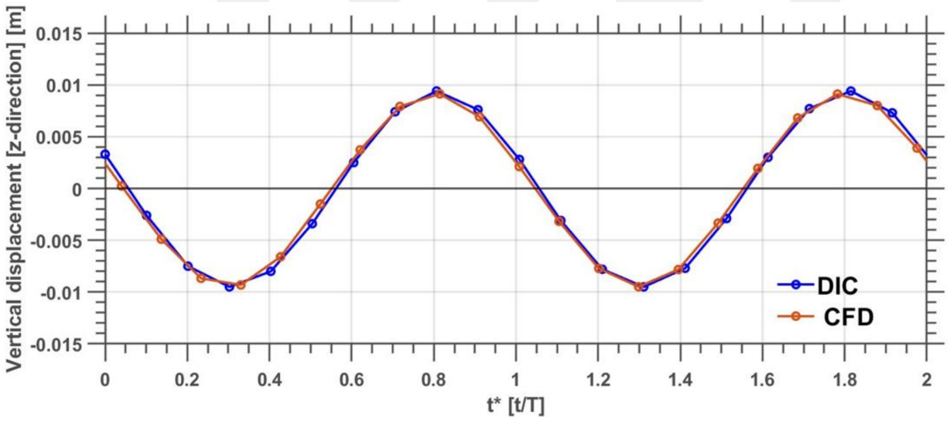

Figure 5.7 DIC and CFD displacement comparison for Rufous hummingbird.

- **Force calculation of DIC and CFD**

It is important to note that inertial forces play a significant role in the flapping motion. A dynamic problem is, given the motion of the wing object, finding the force acting on it. When solving the problem, the second-order curve fits of the acceleration are integrated from the root to the tip of the wing. To obtain the inertial force on the wing, Newton's second law is substituted into the equation (Eq. 5.5).

In the current situation, the dynamic deformation (vertical displacement) and acceleration of the wing models are measured directly from the experimental flapping process.

To calculate the integral of the acceleration curve along the span of the wing, the trapezoidal function is called in MATLAB software.

$$\int_a^b acc(x)dx \approx \frac{1}{2}\sum_{n=1}^{N}(x_{n+1} - x_n)[acc_n(x) + acc_{n+1}(x)] \quad (5.3)$$

where $a = x_1 < \cdots < x_N < x_{N+1} = b$, and $(x_{n+1} - x_n)$ is the spacing between each consecutive pair of points.

Subsequently, an average acceleration value is examined for each wing position at every time step.

$$a_{avg} = \int_a^b acc(x)dx\,/(length\ of\ wing) \quad (5.4)$$

To obtain the inertial forces, the average acceleration values (Eq. 5.4) are multiplied by the mass of the wing (Table 5.1).

$$\vec{F} = m\vec{a}_{avg} \quad (5.5)$$

Table 5.1 Mass properties.

	Density [kg/m³]	**Volume [m³]**	**Mass [kg] (mass proportional to total)**
Rectangle wing	2700	3.7×10^{-6}	0.0078
Hummingbird wing	2700	2.9×10^{-6}	0.00624
Monarch butterfly	2700	1.3500×10^{-7}	0.0012
Piezoelectric material	-	2.6400×10^{-7}	0.002

Based on the information provided, the inertial forces are obtained by using the instantaneous accelerations of the wings. These instantaneous inertial forces are displayed in Figure 5.8 and Figure 5.9 for the rectangular and hummingbird wings, respectively.

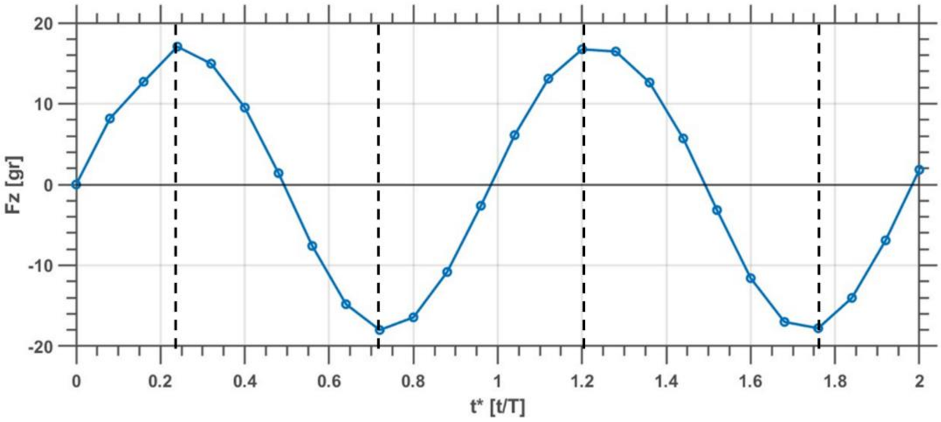

Figure 5.8 Inertial force calculation by rectangle wing acceleration (DIC).

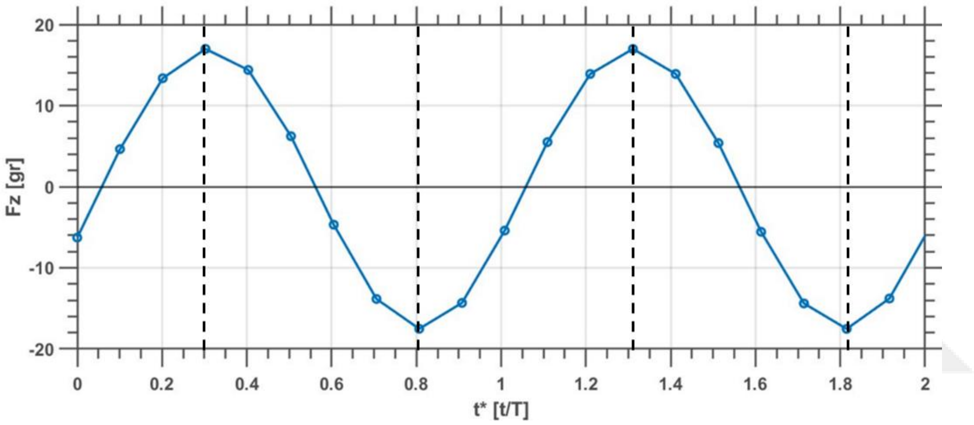

Figure 5.9 Inertial force calculation by Rufous hummingbird wing acceleration (DIC).

It is essential to emphasize that for the rectangular wing, the time instances $t^* = t / T = 0.24$ and $t^* = t / T = 1.2$ indicate identical moments related to the wing attaining the maximum upstroke positions. These instances precisely align with the termination of the upstroke and the initiation of the downstroke, as illustrated in Figure 5.8.

For hummingbird, at $t^* = t / T = 0$, the upstroke of the wing initiates, reaching its peak after the upstroke ($t^* = t / T = 0.3$) with maximum vertical positive force. Subsequently, the downstroke occurs, resulting in a gradual reduction of force until reaching the minimum force value at $t^* = t / T = 0.8$. This pattern continues until the end of the downstroke. This cyclic process repeats periodically for subsequent up and down strokes, as demonstrated in Figure 5.9.

Besides the indication of inertial forces, it is possible to derive the aerodynamic force obtained through CFD, depicted in Figure 5.10 and Figure 5.11. The vertical forces in the z direction obtained aerodynamically are examined in the CFD simulations to demonstrate the amount of the contribution of these forces.

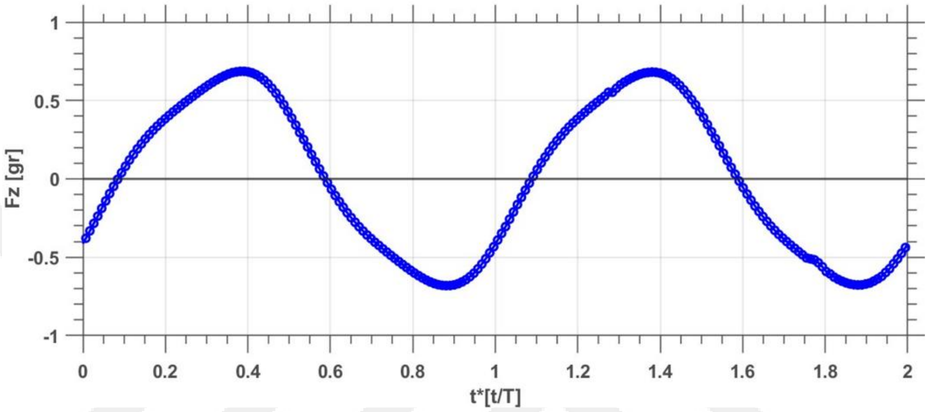

Figure 5.10 Vertical force of the Rectangle wing in z-direction direction.

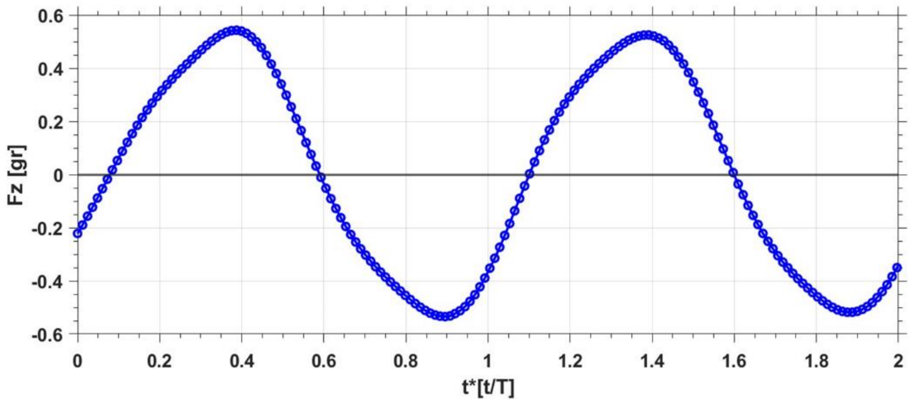

Figure 5.11 Vertical force of Rufous hummingbird wing in z-direction.

The force sensor measures the comprehensive forces in the direction of flapping motion, encompassing both aerodynamic and inertial forces. Consequently, the combined forces can be represented as the sum of aerodynamic and inertial forces, as depicted in Figure 5.14 and Figure 5.15. Following this, these cumulative forces can be compared with the data acquired from the force sensor.

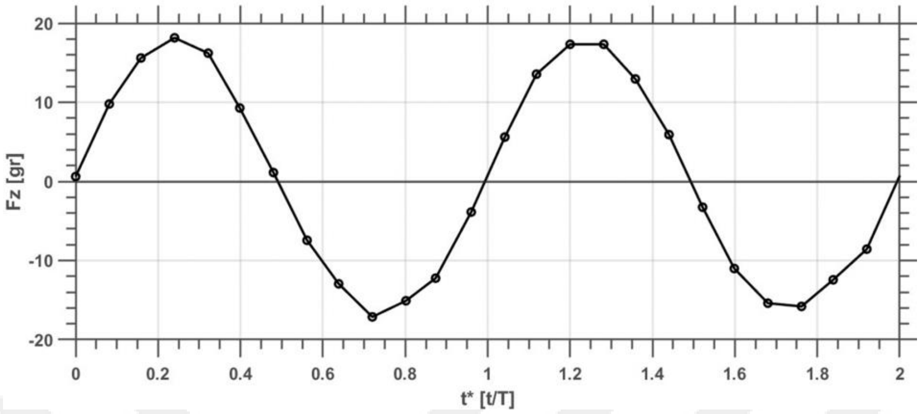

Figure 5.12 Total force measurement in vertical direction [z-direction] of rectangle wing by sensor.

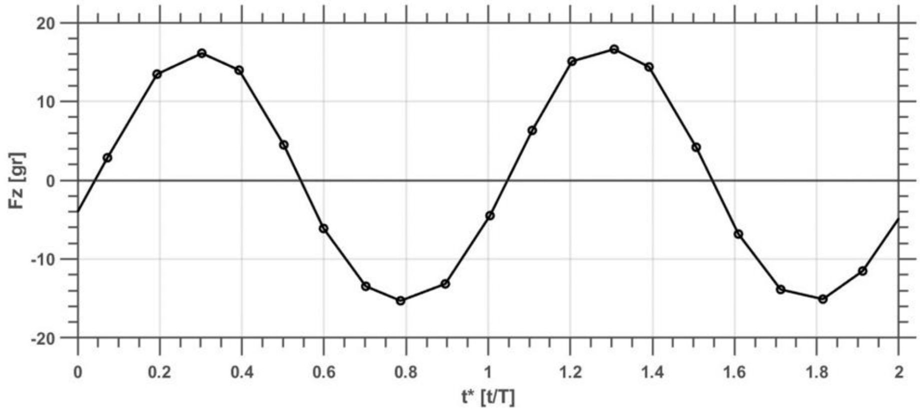

Figure 5.13 Total force measurement in vertical direction [z-direction] of Rufous hummingbird wing by sensor.

Upon examination of the figures, the comparisons unveil closely aligned curves. The clear match is evident at the end of the upstroke and the beginning of the downstroke. However, a marginal discrepancy is observed between the sensor measurement and the total (CFD + Inertial) forces during the reverse motion, corresponding to the end of the downstroke and the beginning of the upstroke. This discrepancy is quantified as 11.6411% in the case of the rectangle wing curves, while the difference for the hummingbird wing is determined to be 14.7834%.

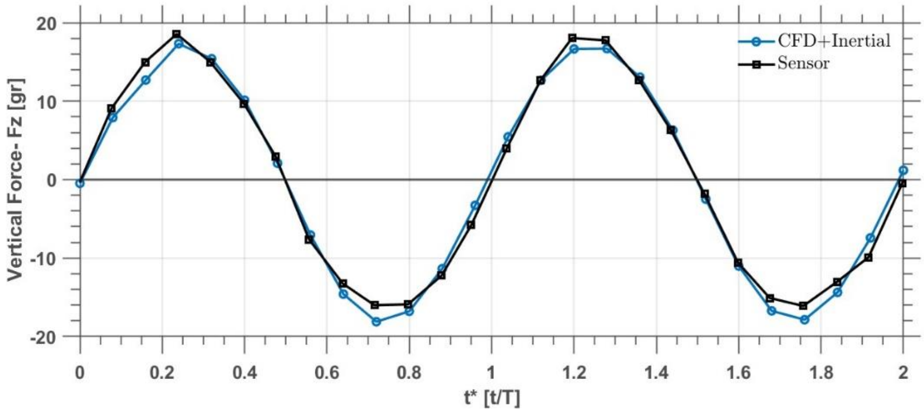

Figure 5.14 Vertical force comparison between CFD and Inertial forces with sensor data in the z-direction (rectangle wing).

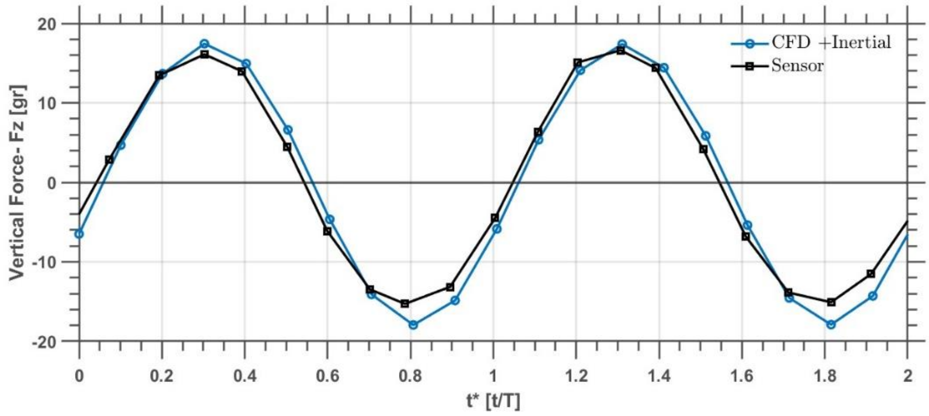

Figure 5.15 Vertical force comparison between CFD and Inertial forces with sensor data in z-direction (Rufous hummingbird wing).

In the z-direction, the mean values of the aerodynamic force and inertial force are approximately zero compared to their peak values. This aligns with the predicted behavior within the current experimental setup. Nonetheless, in the z direction of the rectangle wing, the mean values of aerodynamic force and inertial force are 0.0559 gr and 0.7238 gr, respectively, indicating that the vertical force is almost entirely contributed by inertial force. Similarly, for the hummingbird wing, the corresponding values are 0.0433 gr and 0.4608 gr, respectively.

- **Pressure distribution**

At t* = t/T = 1.266, corresponding to the end of the upstroke for the rectangular wing, a low-pressure region forms on the upper surface due to the presence of the leading-edge vortex. Simultaneously, a relatively noticeable high-pressure area develops on the lower surface due to interaction with the air.

From the commencement of the downstroke until the mid-downstroke motion, vortices migrate towards the wing tip, consequently causing the high-pressure region on the bottom surface of the wing to also shift towards the wing tip. This is depicted in Figure 5.17.

Likewise, at t*=t/T = 1.727, the high-pressure region shifts to the upper surface, while the low-pressure area appears on the lower surface, as observed in the same figure.

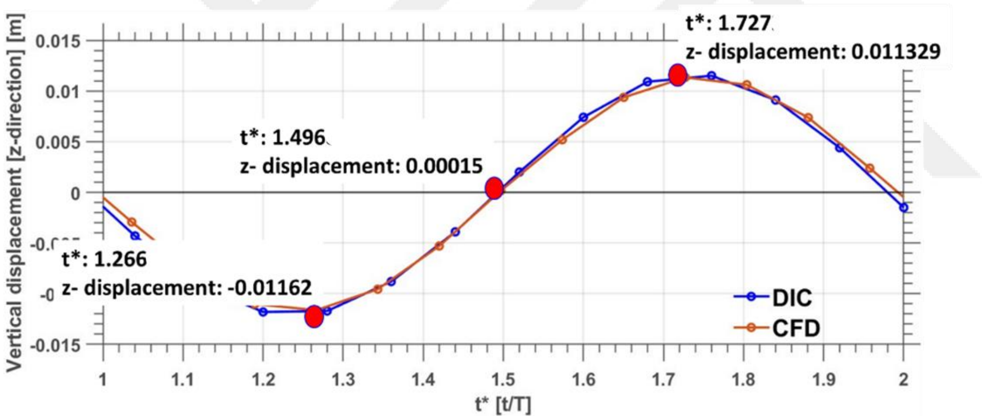

Figure 5.16 One period of flapping motion of rectangle wing (2nd period of flapping motion).

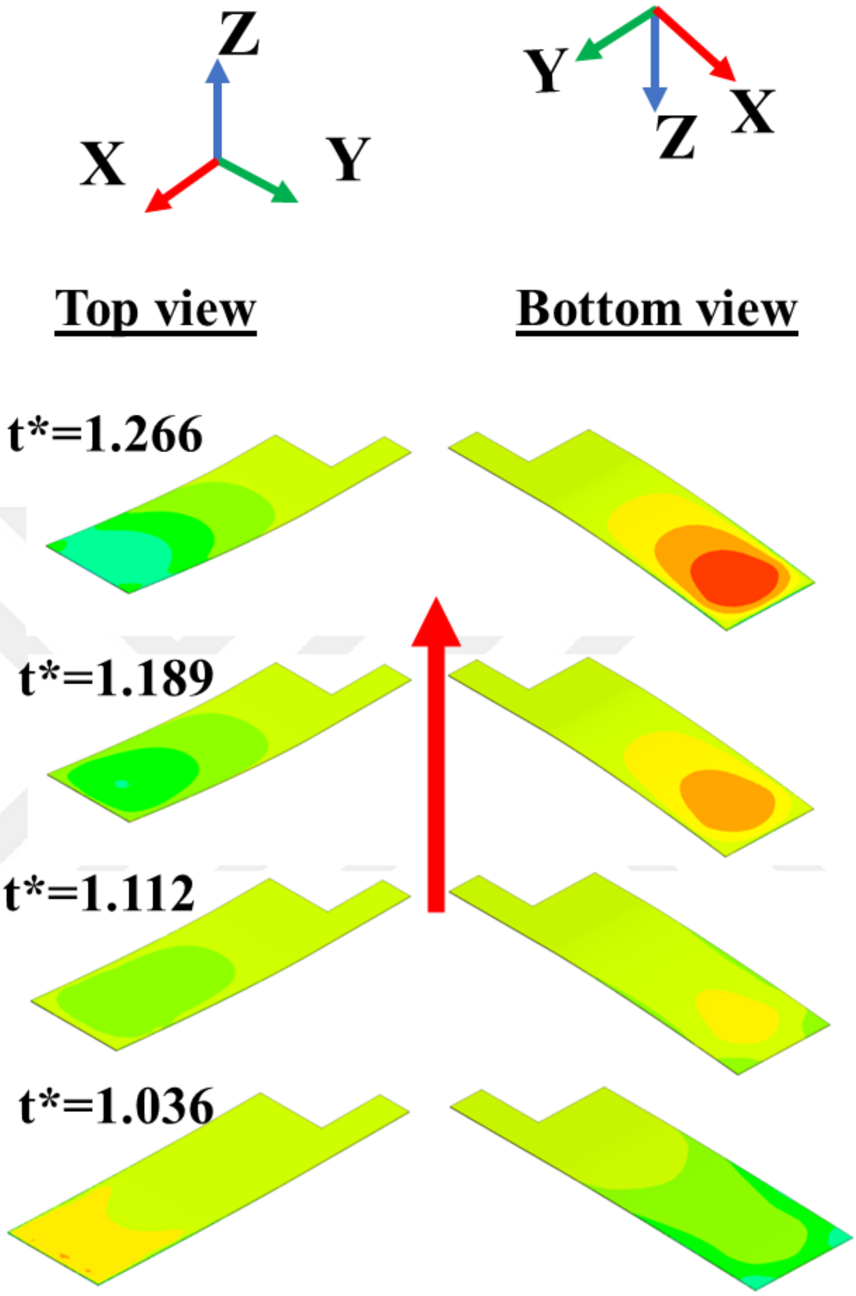

a)

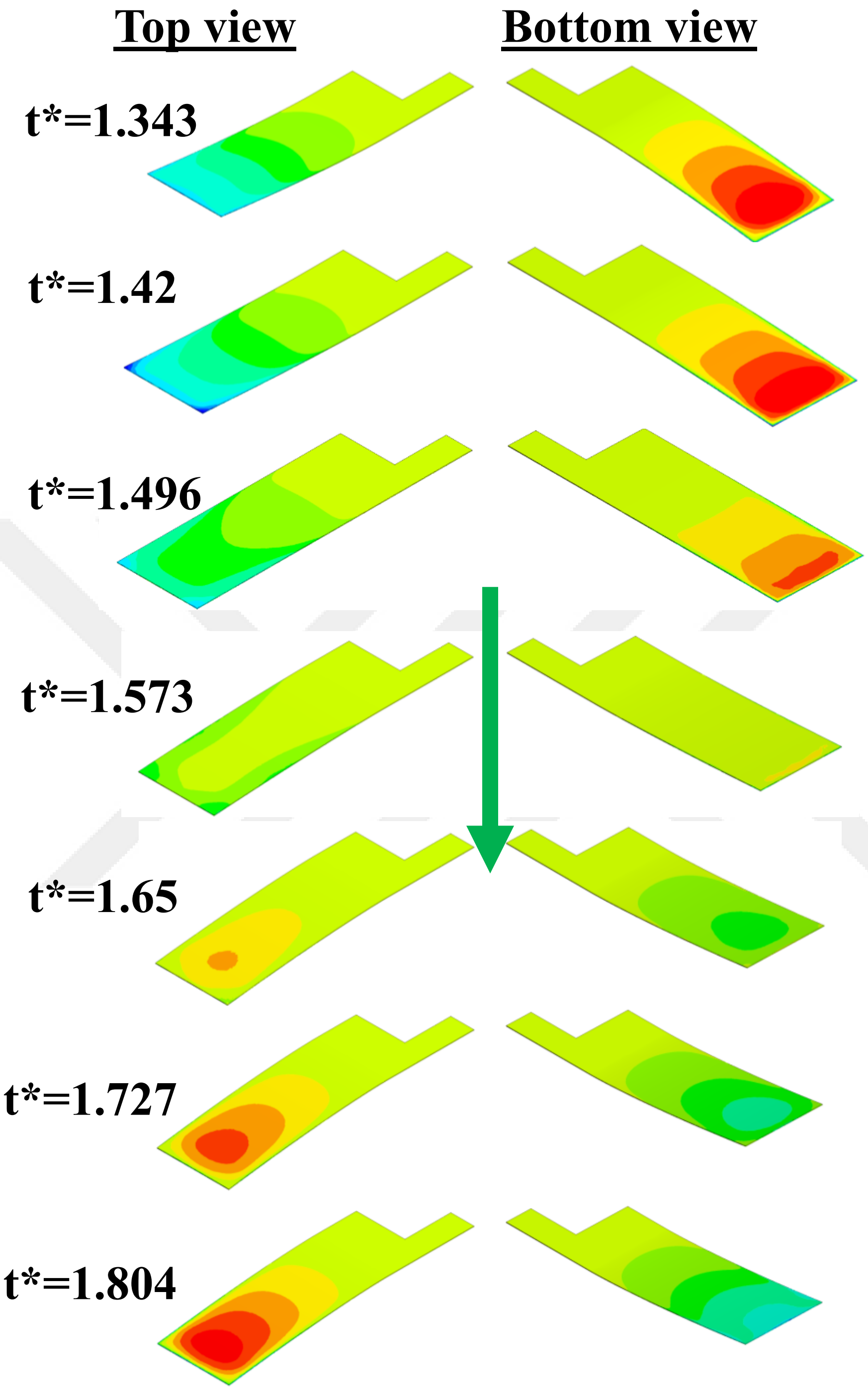
Top view
Bottom view
t*=1.343
t*=1.42
t*=1.496
t*=1.573
t*=1.65
t*=1.727
t*=1.804

b)

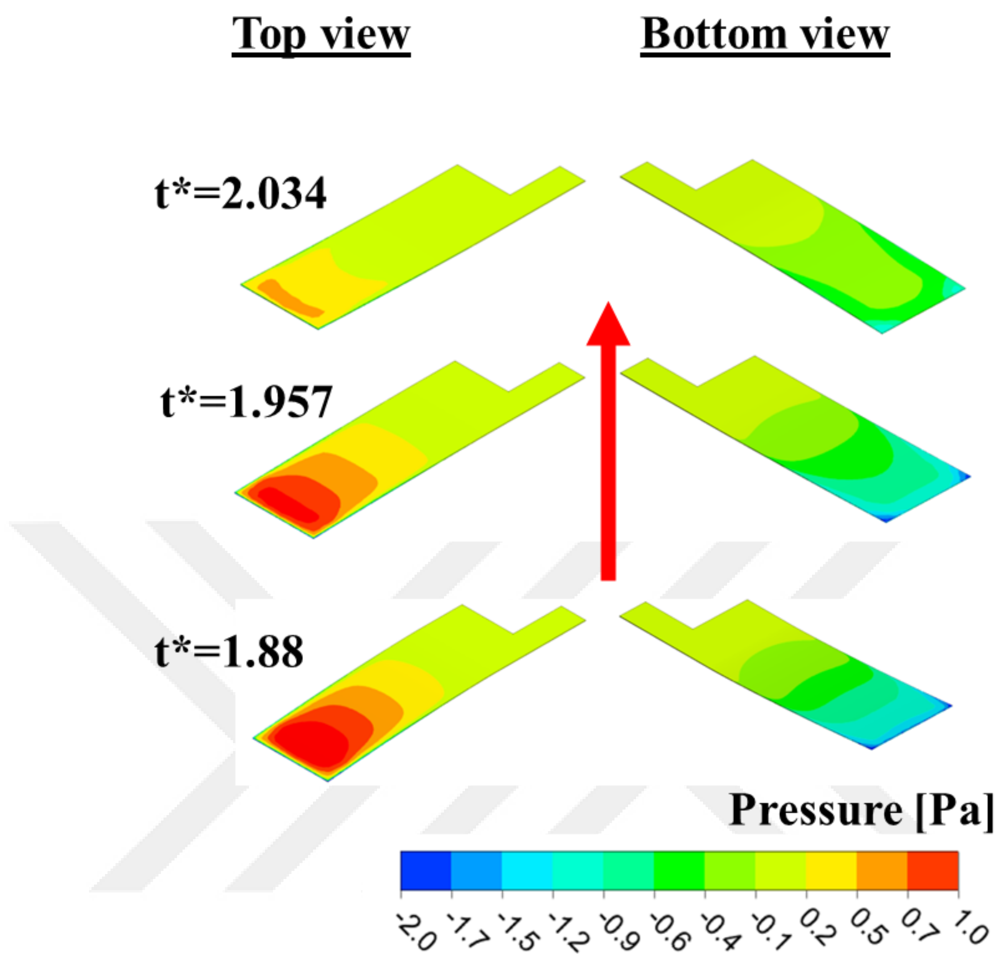

c)

Figure 5.17 Instantaneous pressure contours of rectangle wing (2nd period of flapping motion).

Furthermore, for the hummingbird wing, at t*=t/T = 1.298, a low-pressure region forms on the upper surface again due to the presence of the leading-edge vortex, while a relatively notable high-pressure area develops on the lower surface due to the interaction with the air. This is depicted in Figure 5.19. Likewise, at t*=t/T = 1.782, the high-pressure region shifts to the upper surface, while the low-pressure area appears on the lower surface, as observed in Figure 5.19.

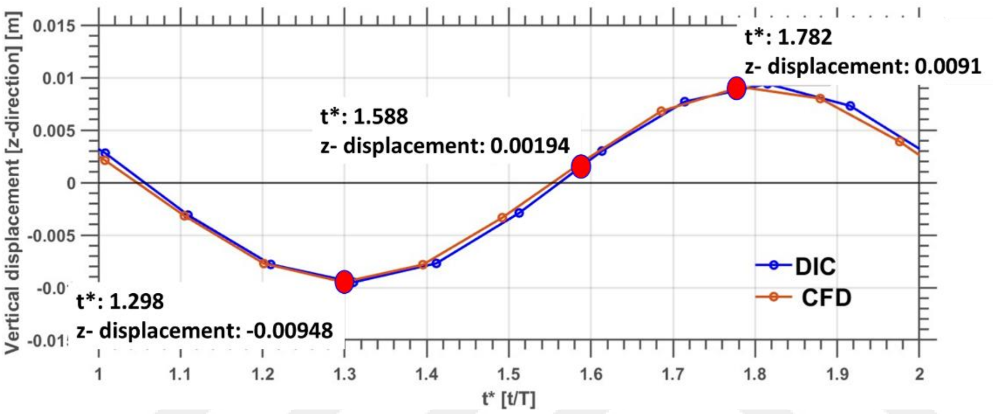

Figure 5.18 One period of flapping motion of Rufous hummingbird wing (2nd period of flapping motion).

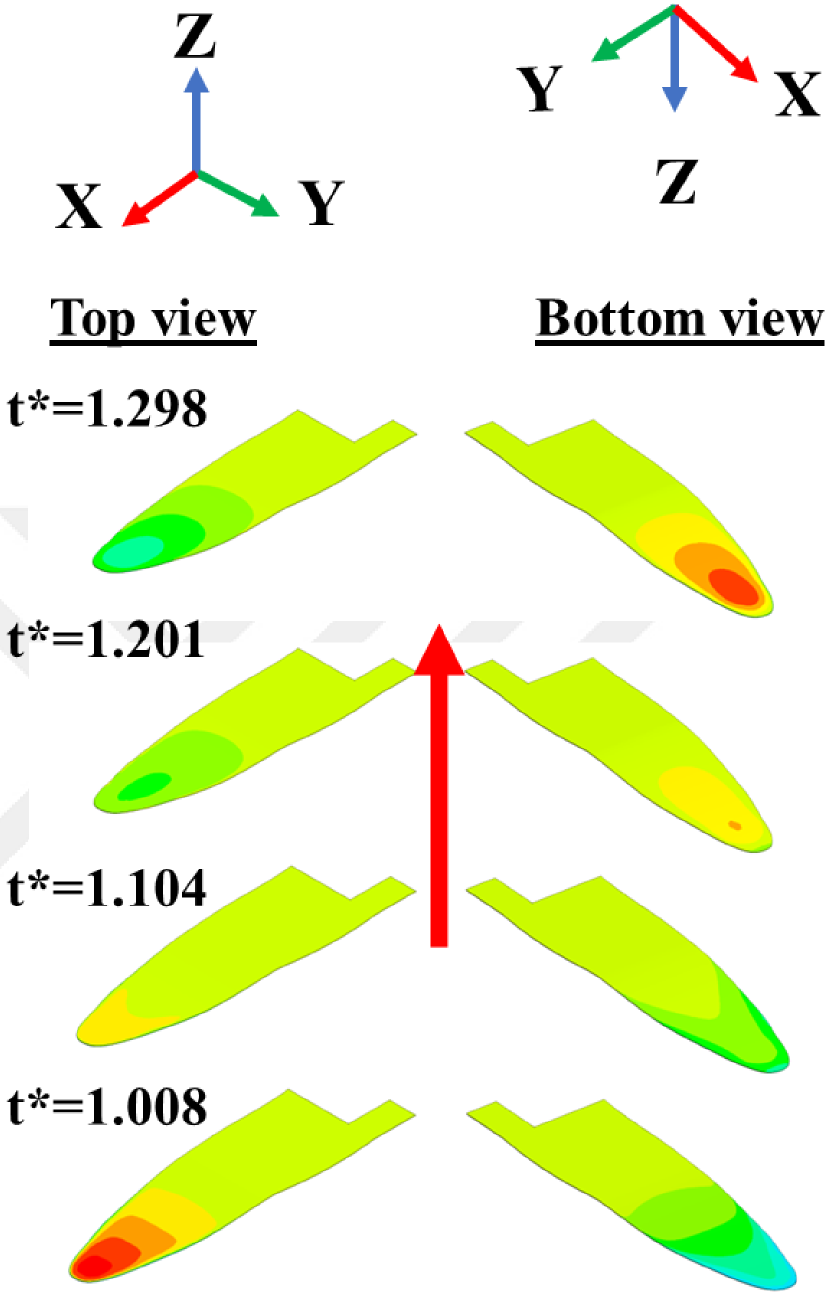

a)

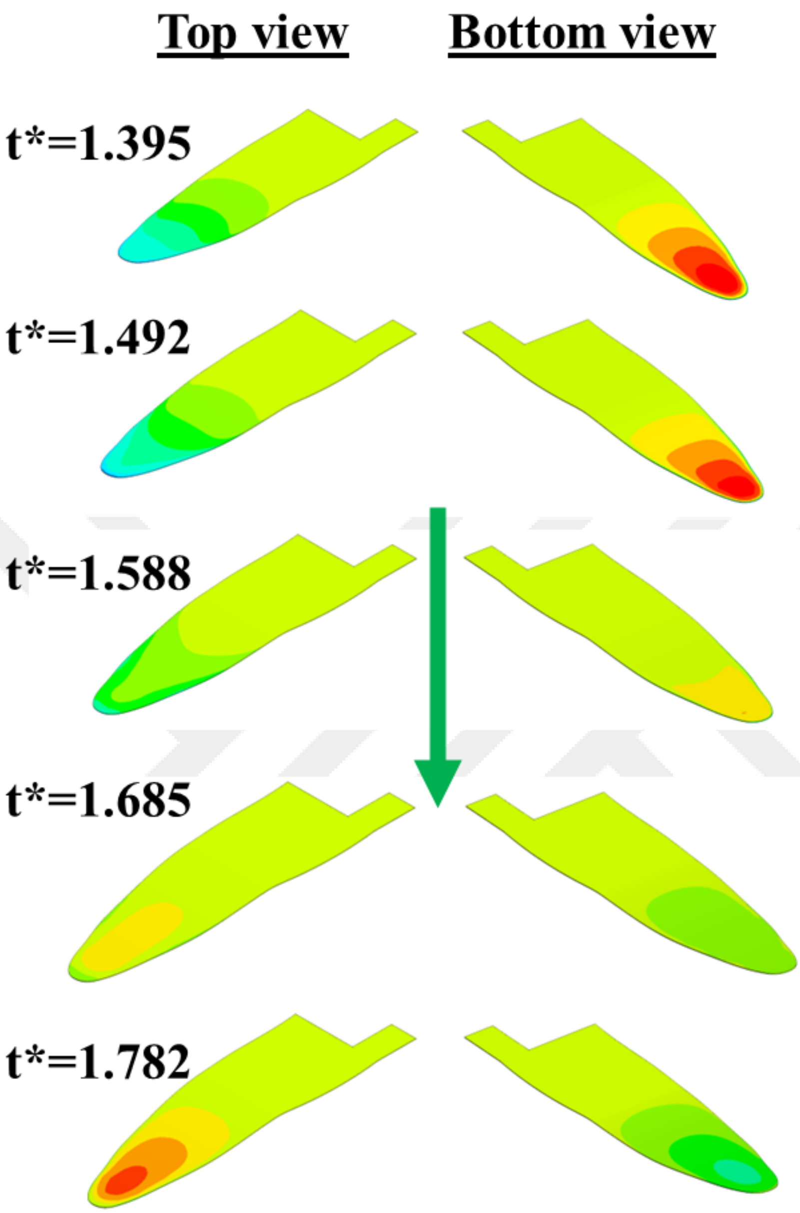

b)

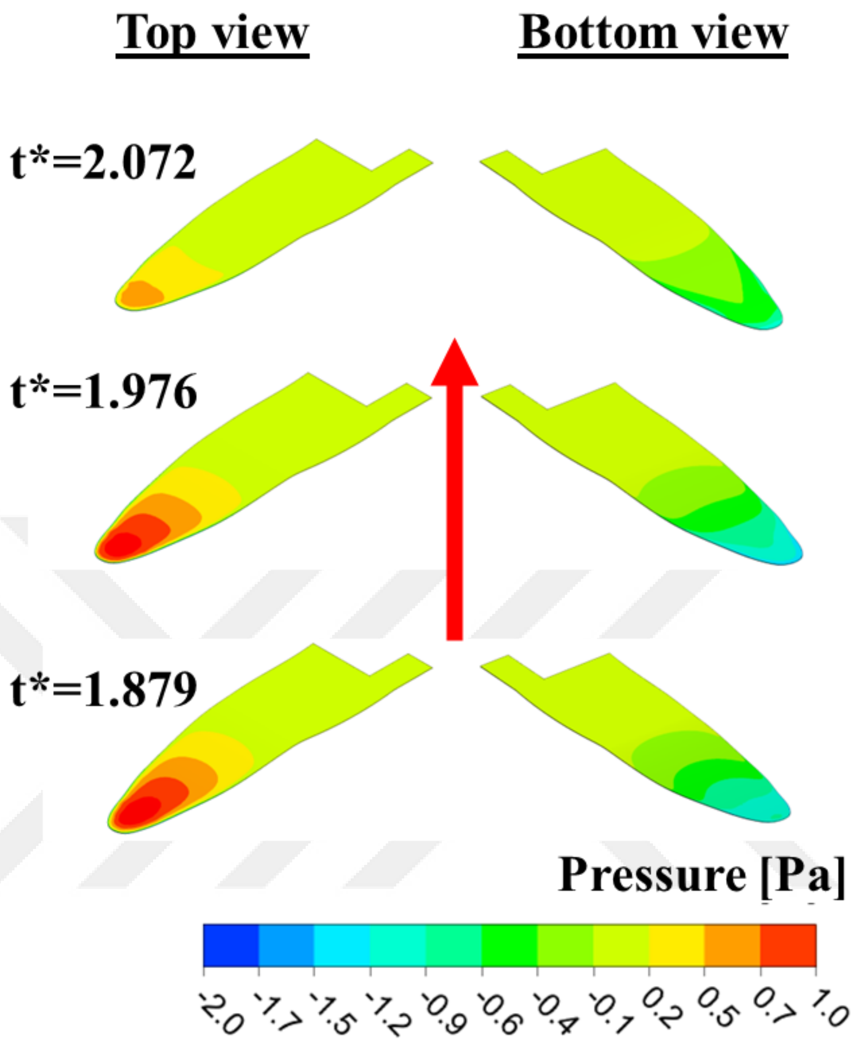

c)

Figure 5.19 Instantaneous pressure contours of rufous hummingbird wing (2nd period of flapping motion).

- **Vortex identification**

To further analyze the flow structures around the wing, the vortex structures at different instances are illustrated by using the non-dimensional Q criterion.

The second invariant of velocity gradient (also called as second invariant of the mean rate-of-displacement tensor) is given by Equation (5.6)

$$Q = \frac{1}{2}(\Omega_{ij}\Omega_{ij} - S_{ij}S_{ij}) \quad (5.6)$$

Once $u_{i,j}$ is known, S_{ij}, Ω_{ij} and Q can be calculated. Q criterion technique is used in vortex identification by Hunt et al. [47].

Non-dimensional Q_{ND} is defined as:

$$Q_{ND} = \frac{Q.S_{wing}}{(U_{tip,max})^2} \quad (5.7)$$

where S_{wing} is the wing area and $U_{tip,max}$ is the maximum velocity of the profile.

Table 5.2 Maximum wing tip velocity for wings.

	Maximum tip velocity (U_{tip}) [m/s]
Rectangle wing	0.6794
Hummingbird wing	0.648
Monarch butterfly wing	0.3018

The vortex structures around the wing are being analyzed to understand their underlying effects on aerodynamics. Figure 5.20, Figure 5.21, and Figure 5.28 depict a few selected instances of the vortex structures near the wing surface at different time instants, respectively. They have been identified by plotting the isosurface of Q_{ND} = 100. By analyzing the Q-criterion of the wings, the three dominant vortex structures namely the leading-edge vortex (LEV), the trailing-edge vortex (TEV), and the tip vortex (TV) are observed in Figure 5.20 and Figure 5.21. At t*=t/T=1.036 for the rectangle wing and t*=t/T=1.008 for the hummingbird wing, when they are at the start of the upstroke, the LEV, TEV, and TV that are generated during the previous upstroke and downstroke are about to shed from the wing to prepare for the generation of new vortexes. Furthermore, upon the wing returns to the straight position, the leading-edge vortex (LEV) remains present on the upper surface. However, this LEV gradually migrates toward the wingtips and initiates spread from the wing surface. Due to the wings flapping under zero free velocity conditions, the vortices are mostly attached however swirl around upper and bottom surfaces.

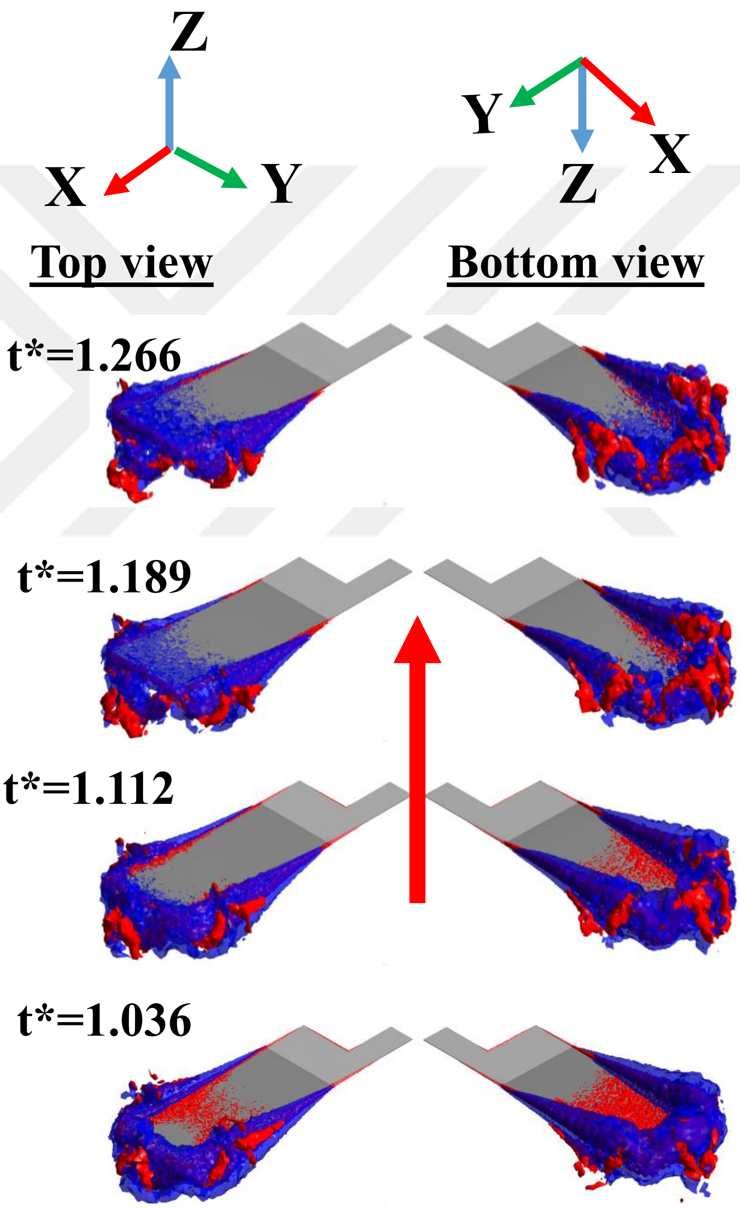

a)

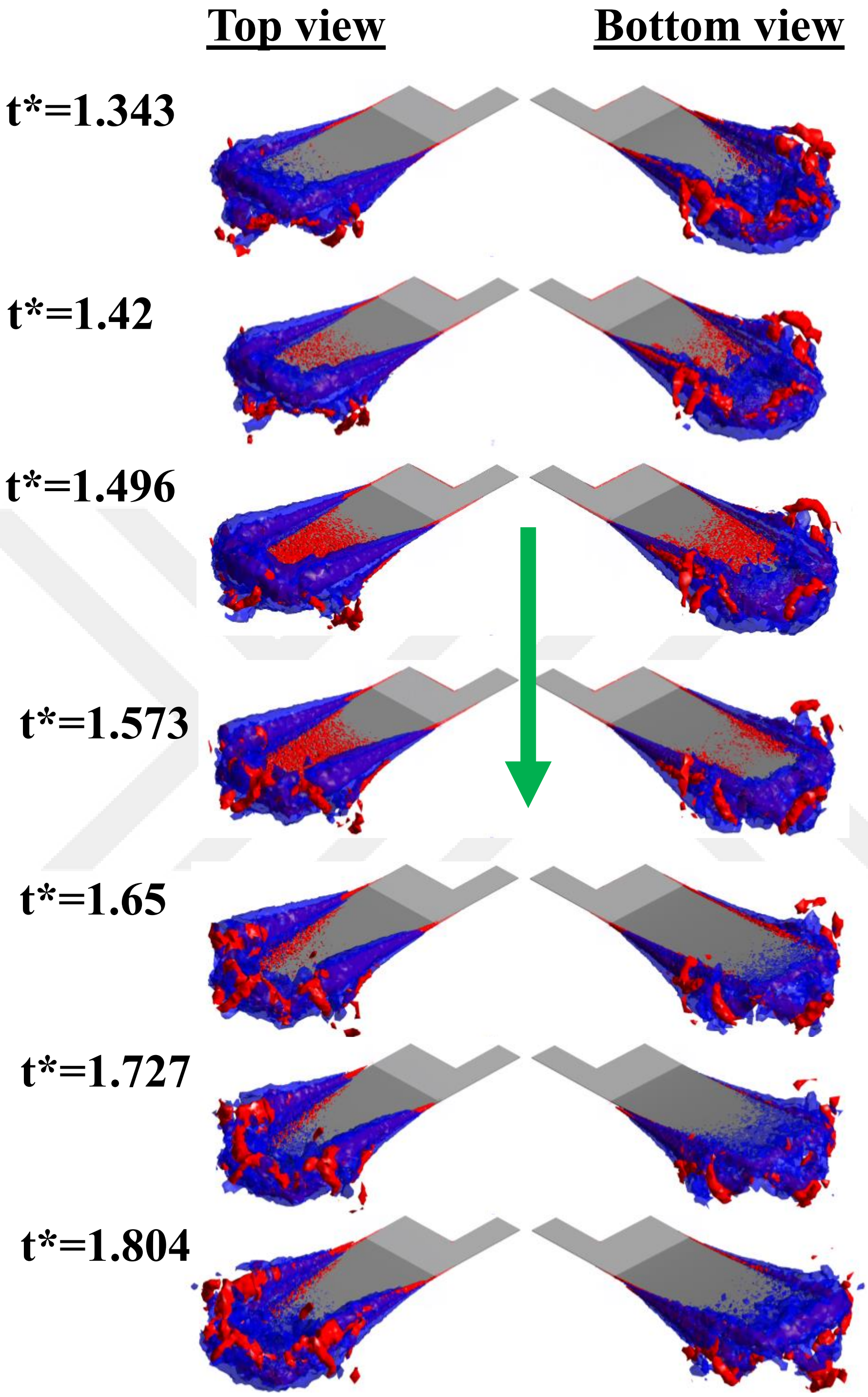
Top view
Bottom view
t*=1.343
t*=1.42
t*=1.496
t*=1.573
t*=1.65
t*=1.727
t*=1.804

b)

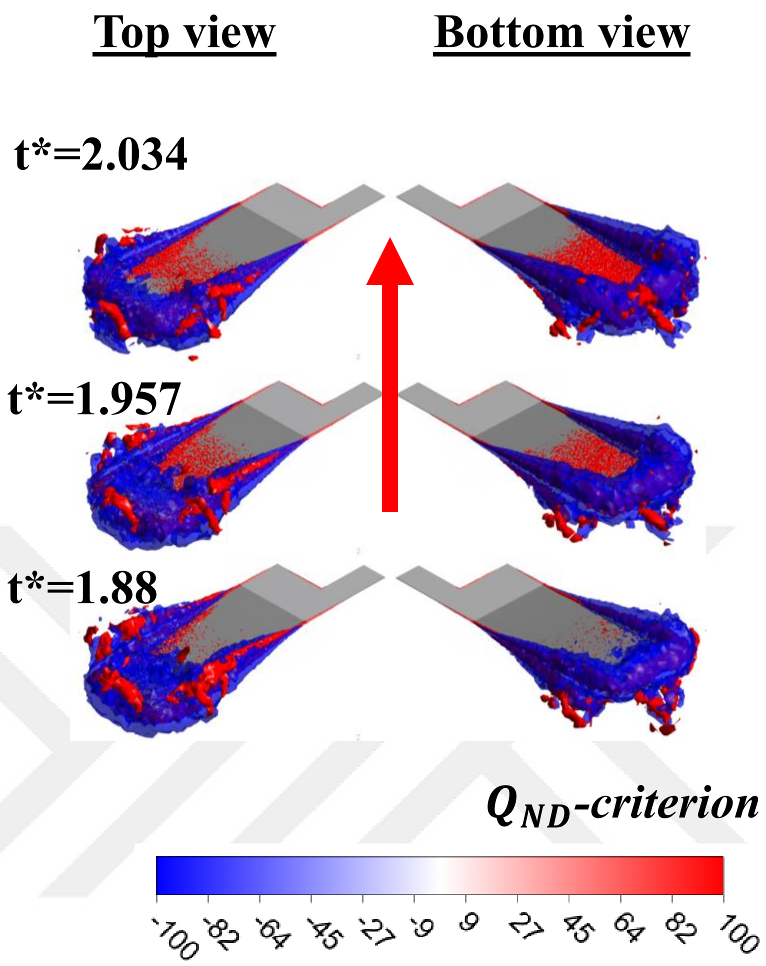

c)

Figure 5.20 Isosurface of non-dimensional Q criterion colored during one flapping cycle (rectangle wing, blue: negative, red: positive vortices).

A ring vortex developed progressively from the previous period tends to break away as the wings move upward, transitioning from the upper side to the lower side of the wing. This behavior persists from the end of the upstroke to the mid-downstroke. Meanwhile, a new ring vortex becomes visible on the upper surface of the wings at the beginning of the mid-downstroke. This formation is sustained throughout the upstroke and downstroke due to the periodic flapping motion of the wings.

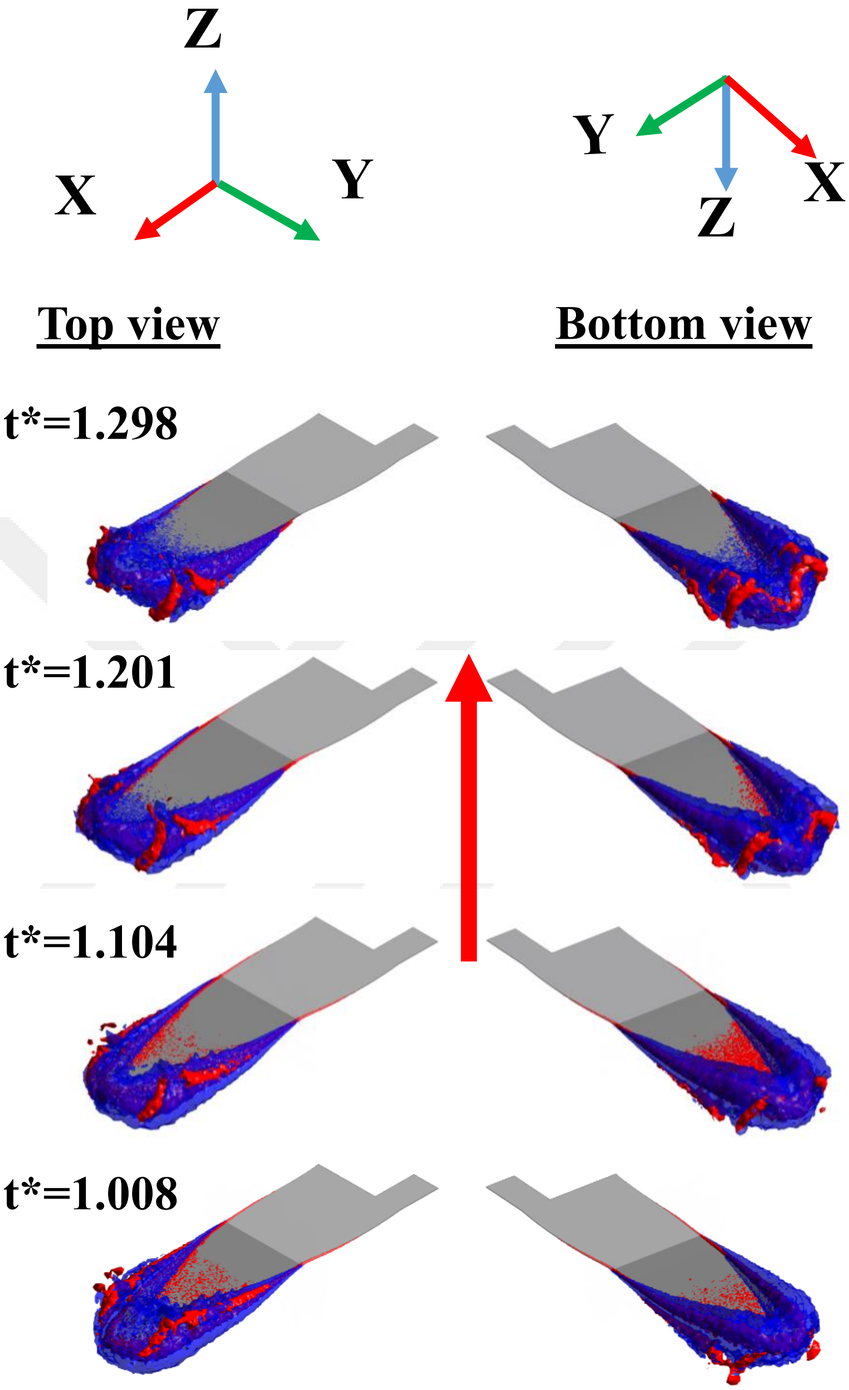

a)

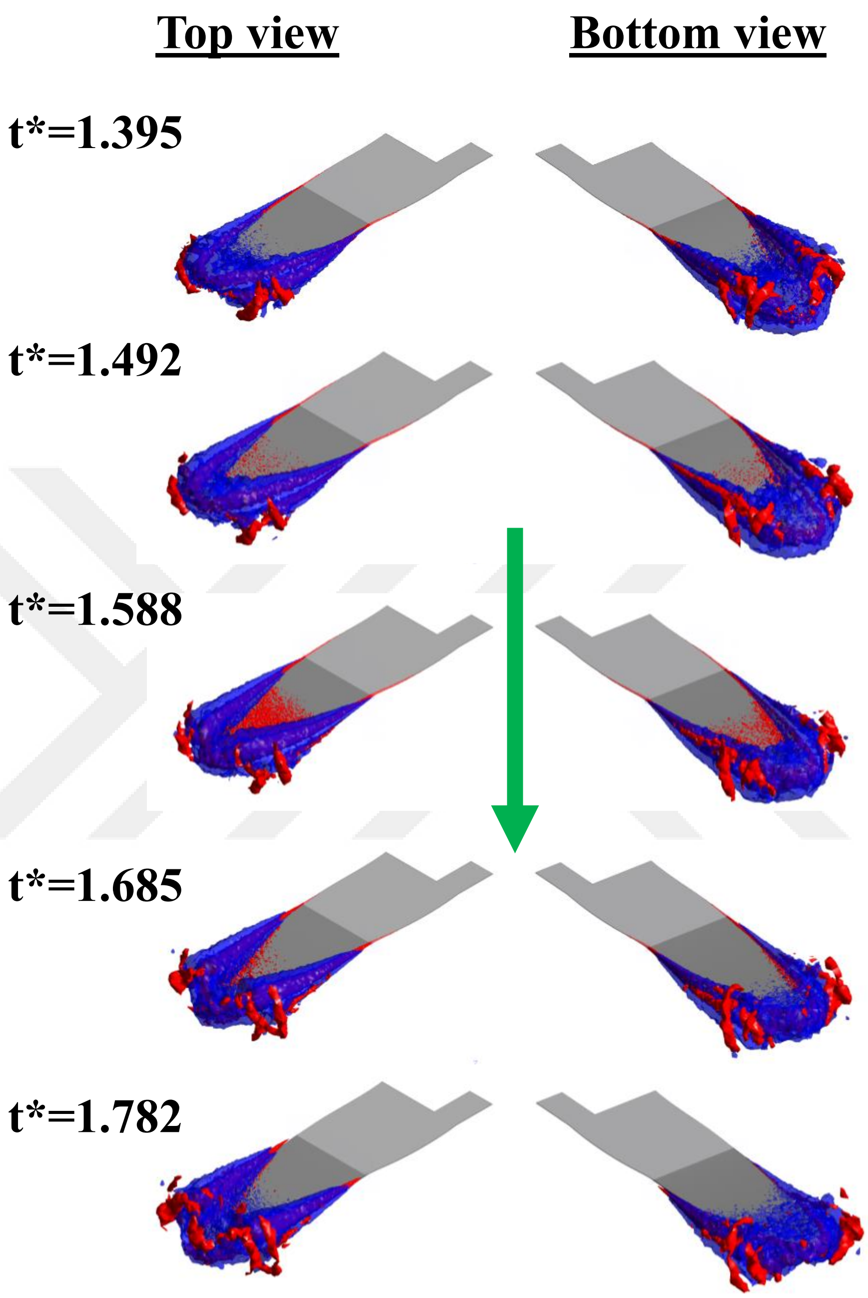

b)

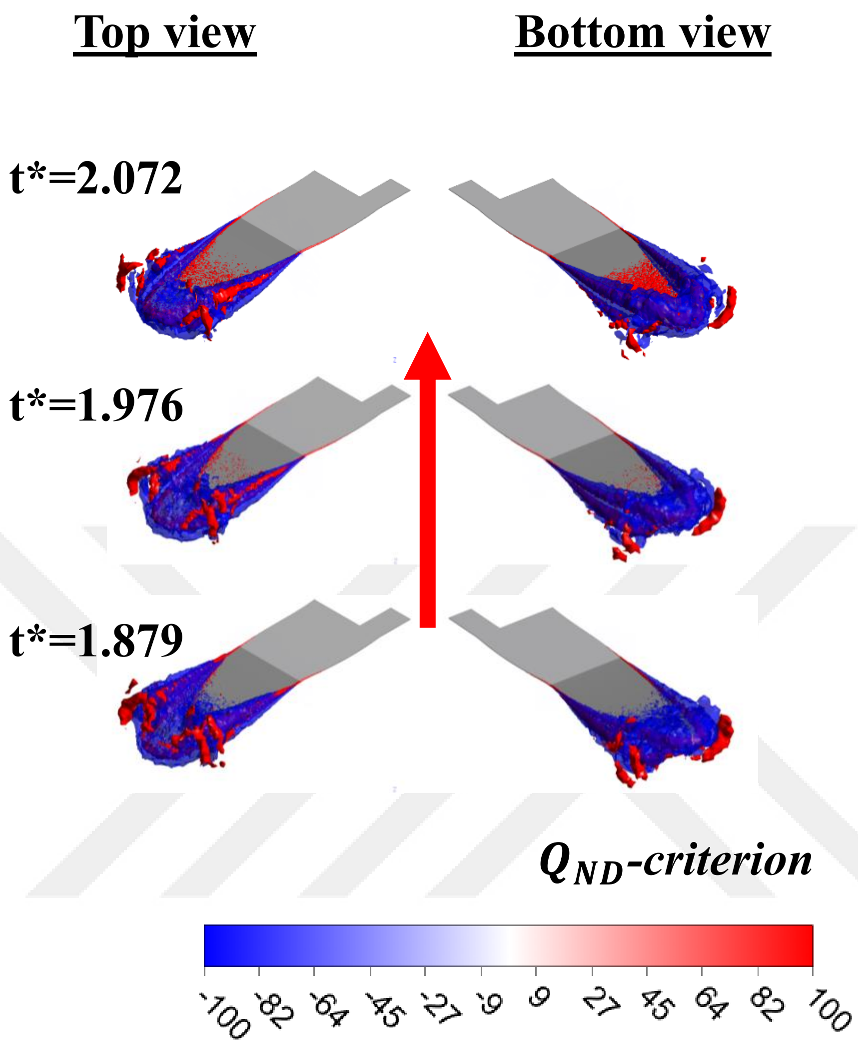

c)

Figure 5.21 Isosurface of non-dimensional Q criterion colored during one flapping cycle (hummingbird wing, blue: negative, red: positive vortices).

Based on the wing morphology, the vortices exhibit greater dispersion in the sharply-cornered rectangular wing (depicted in Figure 5.20). In contrast, in the hummingbird wing, designed to mimic avian wings, the vortices manifest in a configuration more closely adhering to the wing. In both wing configurations, there is an augmentation in vortex size from the root, with this enlargement being more closely associated with the hummingbird wing surface (in Figure 5.21). It is essential to consider that the vortices adhering to the wings could be attributed to the constraint of the flapping angle within narrow degrees.

5.1.2 Unsteady aeroelastic effect analysis of piezoelectric actuated Monarch butterfly wing

In this chapter, the studies conducted for the rectangular wing and hummingbird wing in the preceding subheadings are reiterated for the Monarch butterfly wing under this subheading.

The same spherical grid domain is used for numerical solutions to investigate the aeroelastic effects of the Monarch butterfly wing. The motion was investigated from DIC dynamic deformations of rectangular wings. The same motion is implemented into the numerical study for the Monarch butterfly wing.

Regarding the configuration of the flapping motion of the Monarch butterfly wing, the kinematic values are lower than those of the rectangle wing and hummingbird wing counterparts. These anticipated outcomes are illustrated in Figure 5.22.

In terms of the acceleration during the flapping motion of the Monarch butterfly wing, the inertial force generation is illustrated in Figure 5.24. Although there is no direct sensor force measurement for the butterfly wing, the results are compared to the extent possible with those of the rectangle and hummingbird wings.

Moreover, employing the DIC motion curve for the Monarch wing, simulation data is acquired, and an examination of vertical force is conducted. Subsequently, for detailed insights into the flow, investigations are carried out on instantaneous pressure distribution contours and vortex structures at specific time instances (in Figure 5.27 and Figure 5.28).

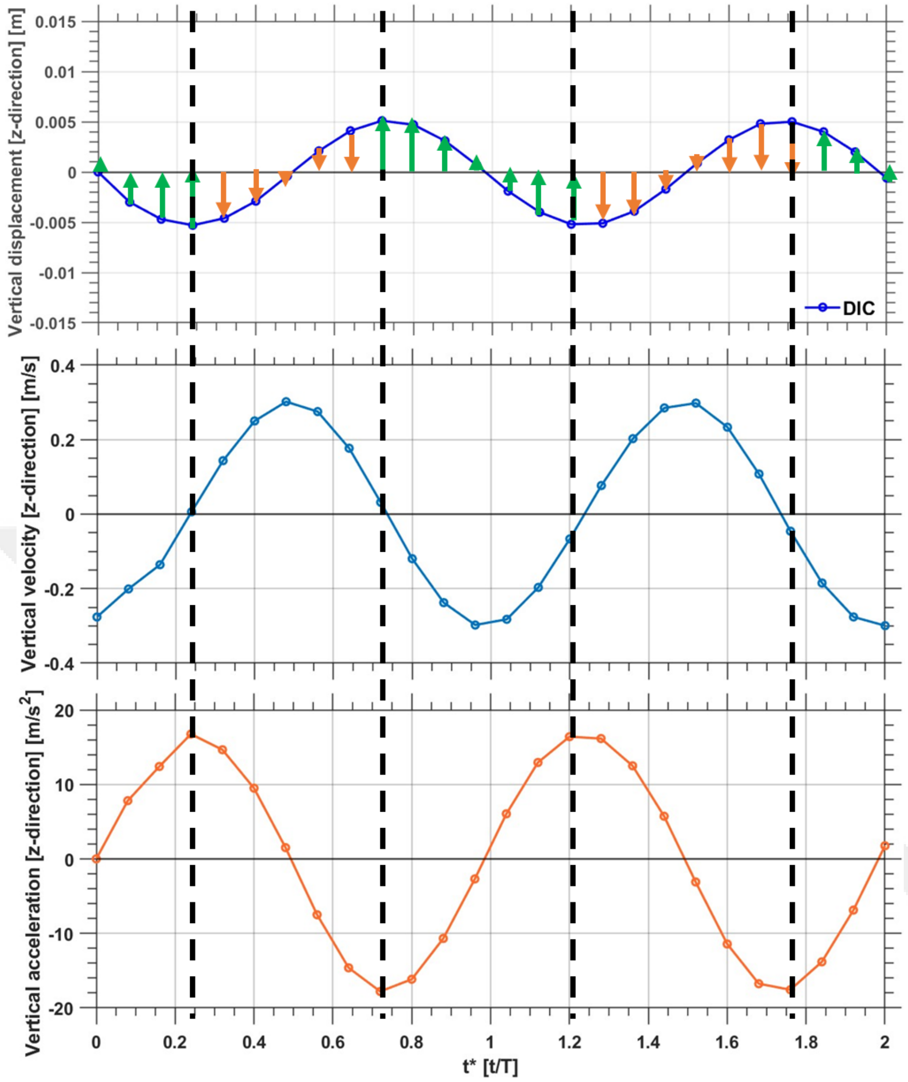

Figure 5.22 Kinematic properties of Monarch butterfly wing.

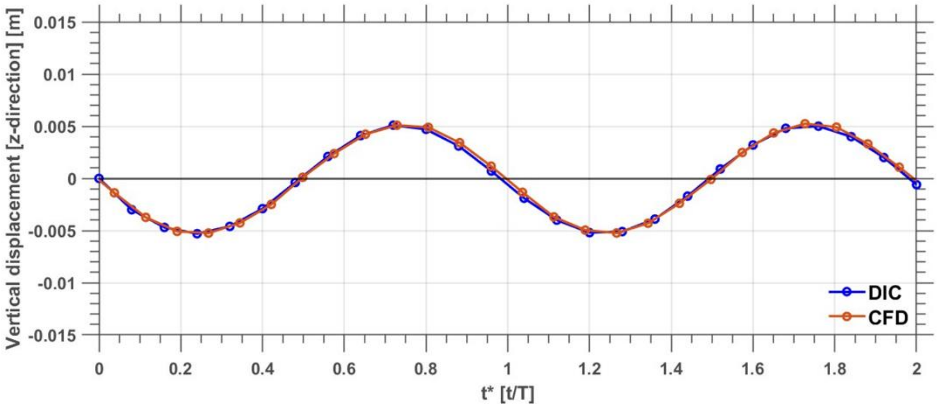

Figure 5.23 DIC and CFD displacement comparison of Monarch butterfly.

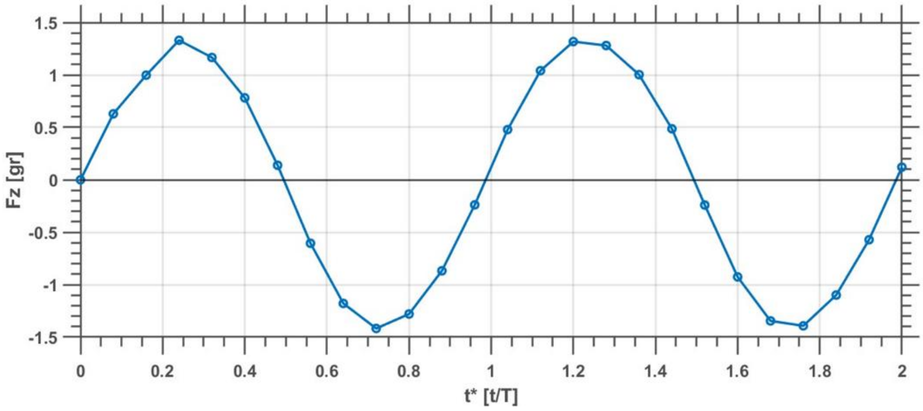

Figure 5.24 Inertial force calculation by Monarch butterfly acceleration (DIC).

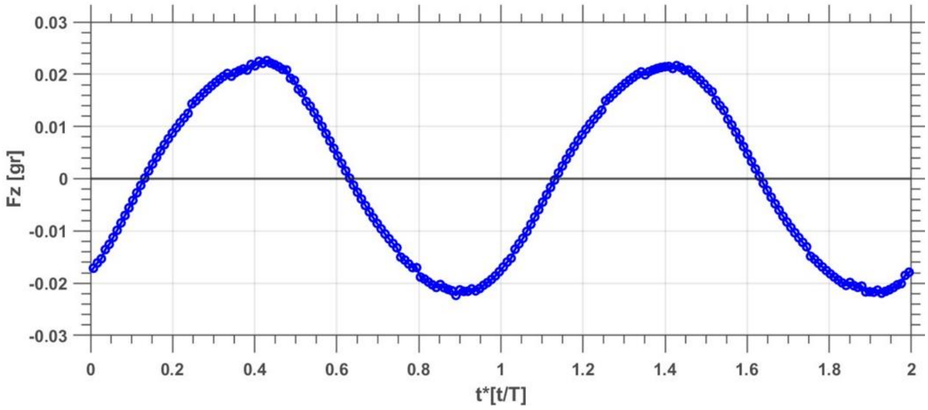

Figure 5.25 Monarch butterfly CFD force in vertical direction [lift in z-direction].

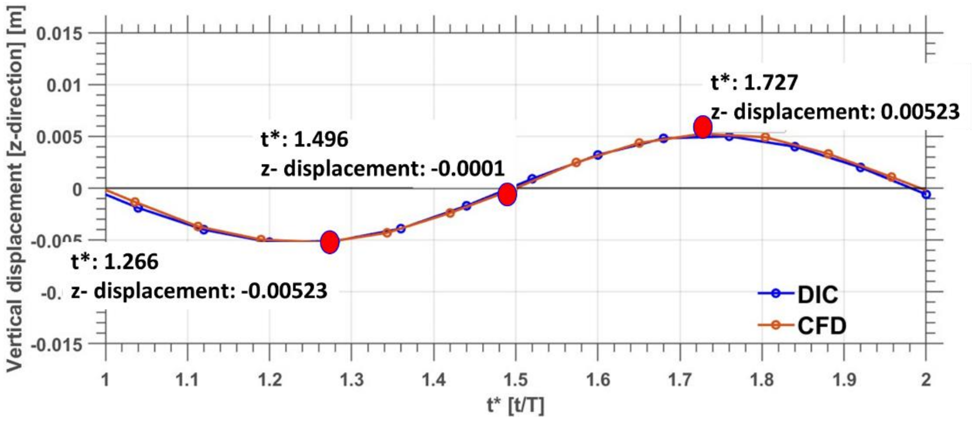

Figure 5.26 One period of flapping motion of Monarch butterfly wing (2nd period of flapping motion).

When analyzing the Monarch butterfly wing, it was noted that the vortex structures exhibited a slightly more positive and negative nature, with clearly visible vortices in Figure 5.28. Consequently, it is evident that at t* = 1.266, representing the conclusion of the upstroke motion as indicated in Figure 5.26, the vortices from the previous cycle detach from the outer margin edges of the forewing and hindwing, giving rise to new vortices. This behavior persists in the wing section after the mid-downstroke at t* = 1.65, and by the end of the downstroke t* = 1.727, the vortices have separated from the wing, initiating the formation of new vortices for the reverse motion.

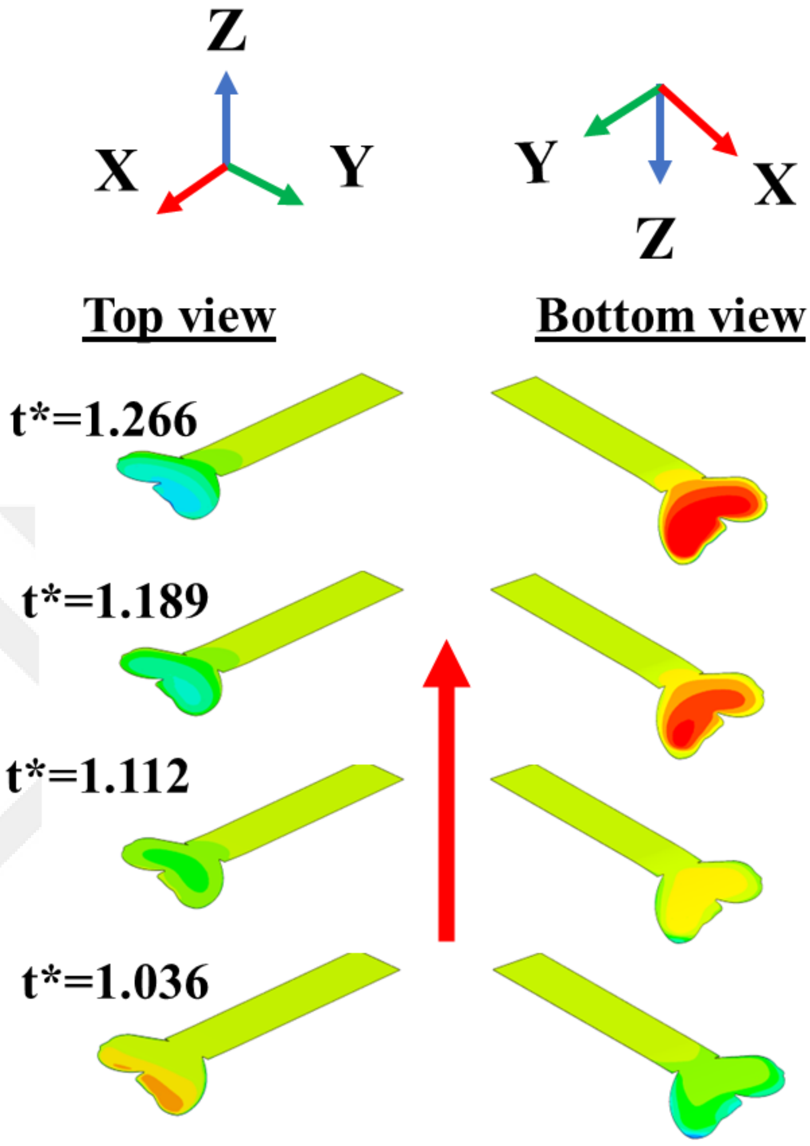

a)

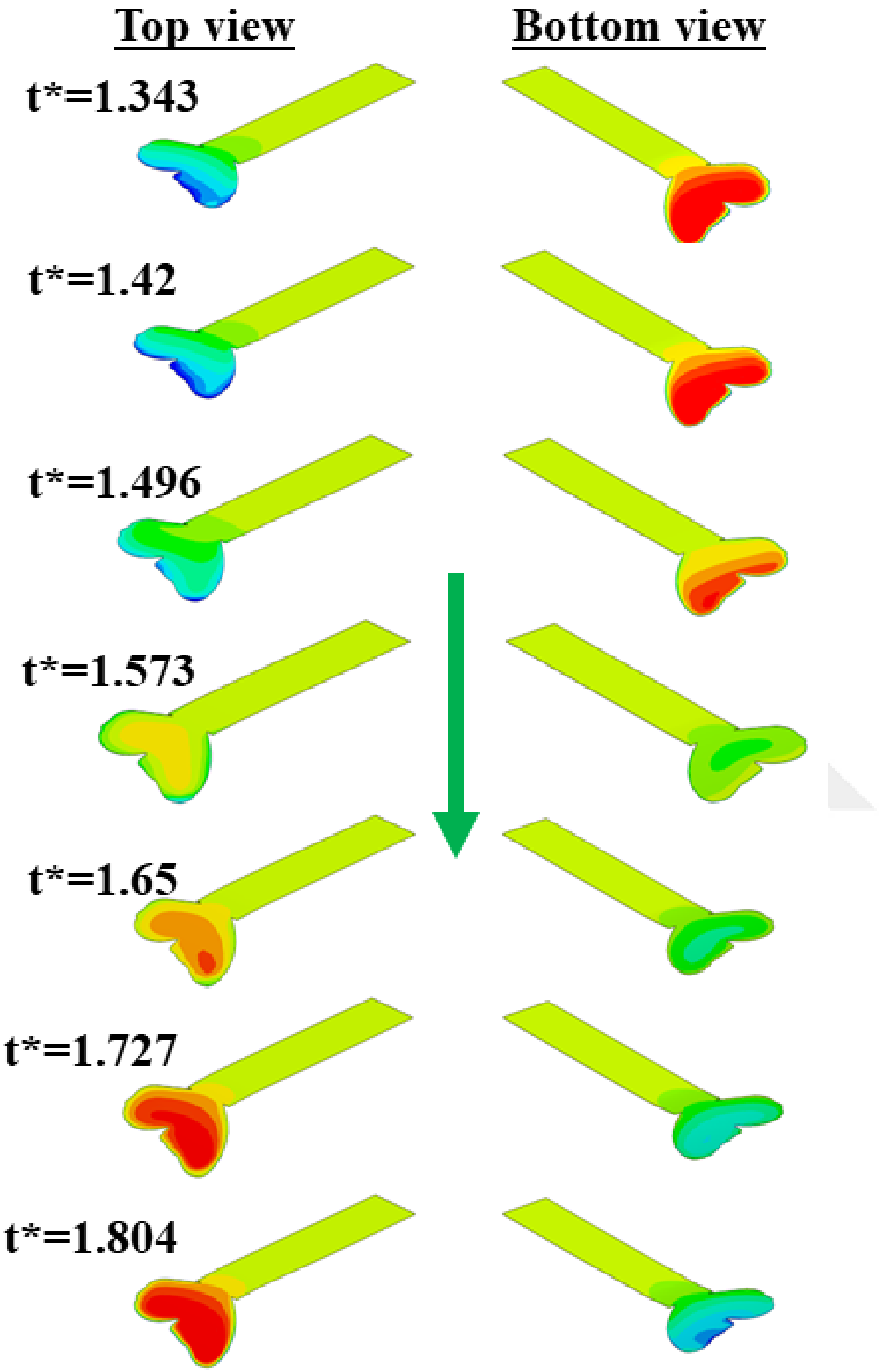
Top view
Bottom view
t*=1.343
t*=1.42
t*=1.496
t*=1.573
t*=1.65
t*=1.727
t*=1.804

b)

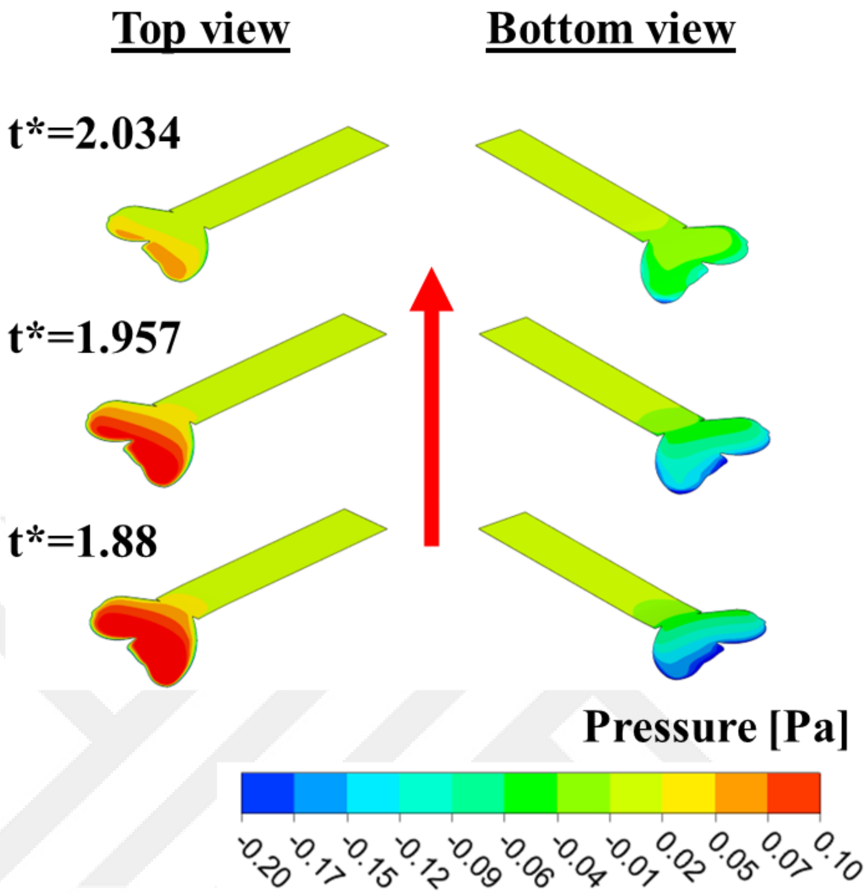

c)

Figure 5.27 Instantaneous pressure contours of Monarch butterfly wing (2nd period of flapping wing).

A ring vortex developed progressively from the previous period tends to break away as the wings move upward, transitioning from the upper side to the lower side of the wing. This behavior persists from the end of the upstroke to the mid-downstroke. Meanwhile, a new ring vortex becomes visible on the upper surface of the wings at the beginning of the mid-downstroke. This formation is sustained throughout the upstroke and downstroke due to the periodic flapping motion of the wings.

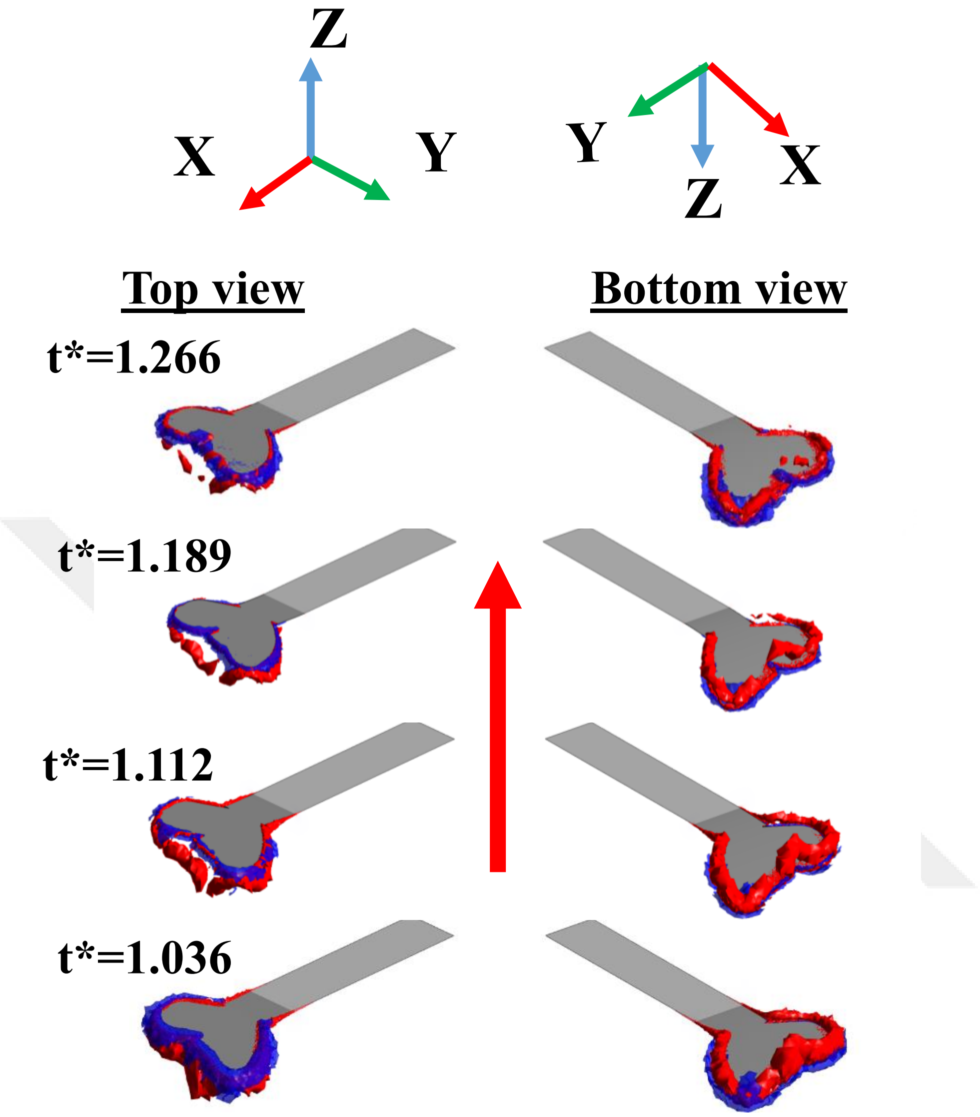

a)

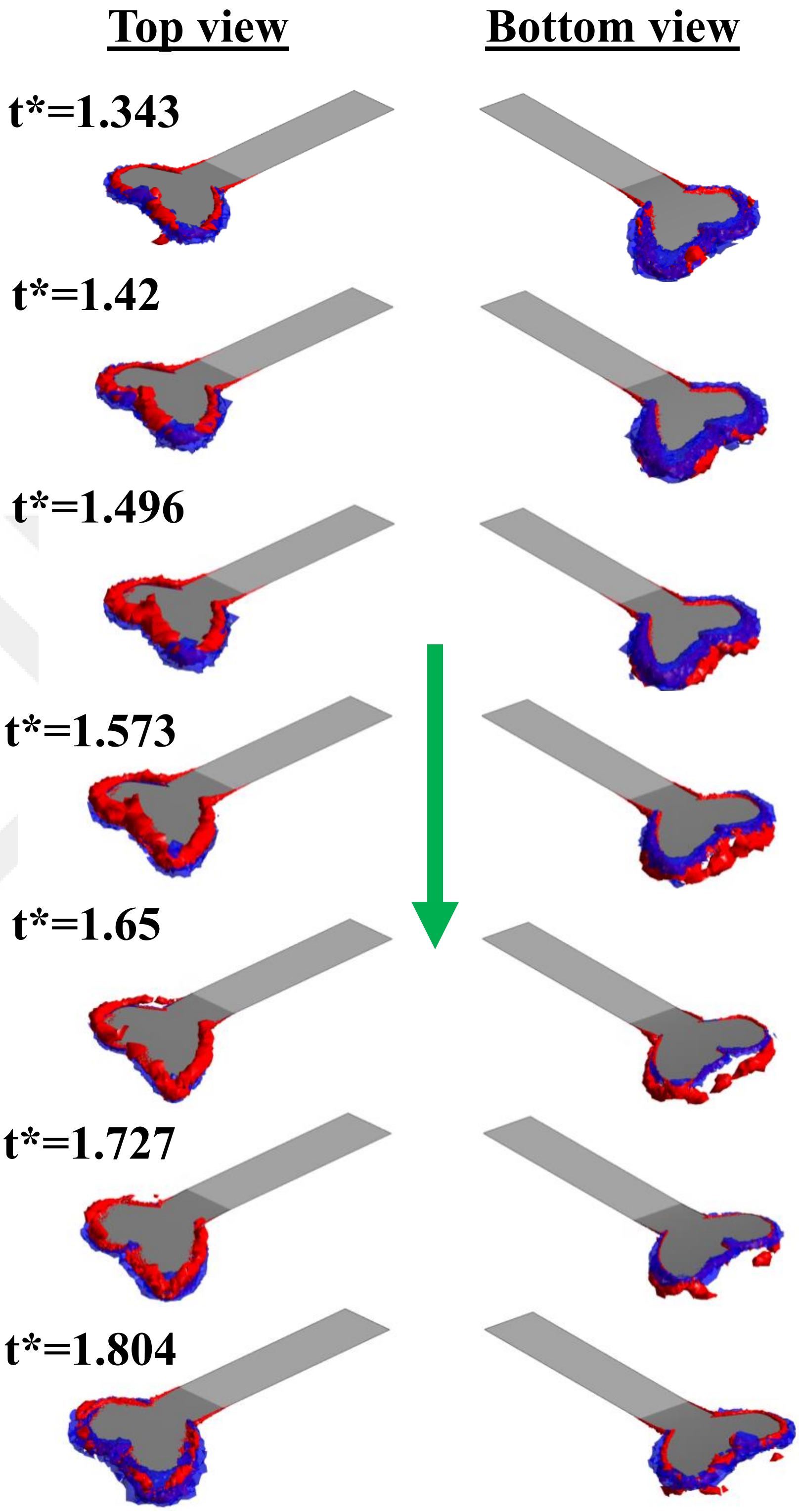

Top view
Bottom view
t*=1.343
t*=1.42
t*=1.496
t*=1.573
t*=1.65
t*=1.727
t*=1.804

b)

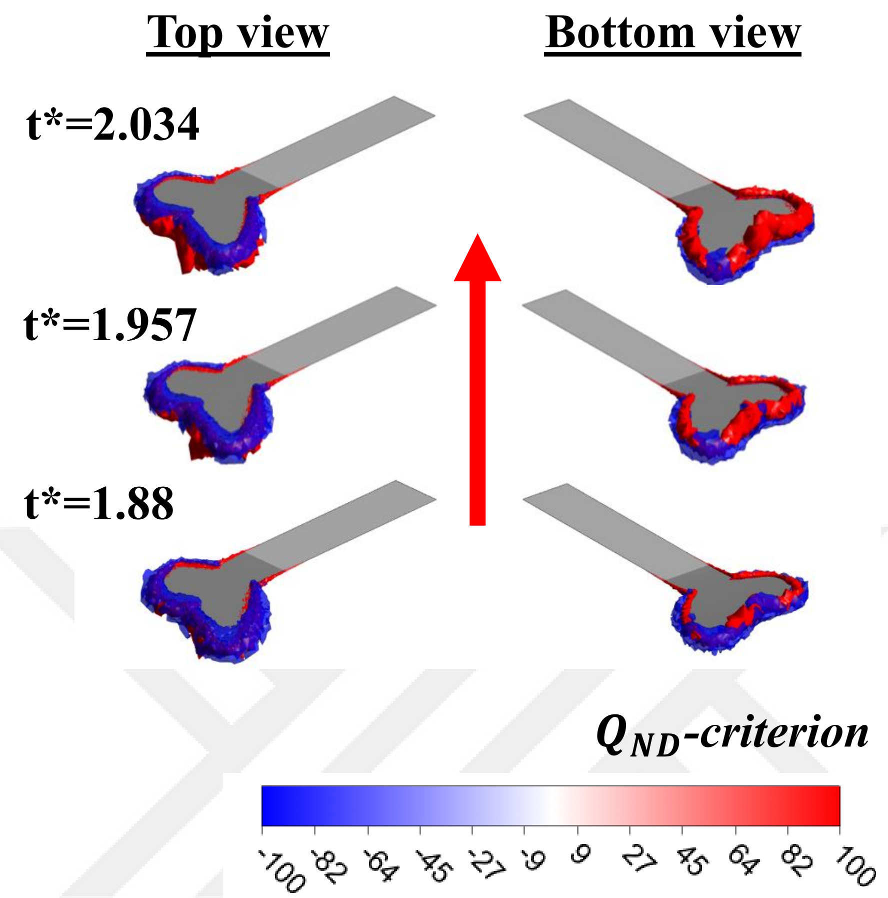

c)

Figure 5.28 Isosurface of non-dimensional Q criterion (colored during one flapping cycle (Monarch butterfly wing, blue: negative, red: positive vortices).

The investigation into force generation in a bio-inspired flapping wing, referred to as one rectangle wing, one Rufous hummingbird wing, and a Monarch butterfly wing, is conducted through a combined utilization of experimental and numerical techniques. The study involved the analysis of aerodynamic and inertial forces contributing to the piezoelectrically actuated flapping wing mechanism.

To accurately capture the dynamic deformations in the flapping wings, Digital Image Correlation (DIC) technology is employed. Subsequently, this dynamic deformation data is integrated into the Computational Fluid Dynamics (CFD) solver to incorporate aeroelastic effects. It's crucial to note that obtaining the dynamic deformation of the wing through experimentation alleviates the need for a complex Fluid-Structure Interaction (FSI) model. Furthermore, leveraging this dynamic deformation data, the calculation of inertial forces acting on the wing is performed, thus considering the flexibility effect in the analysis.

The comparative analysis between the numerical findings (CFD + Inertial) and the experimental outcomes (force sensor/load cell values) is conducted. In essence, the patterns observed in the fluctuations of the forces exhibited similarity between the experimental and numerical data. Notably, a close agreement is evident, especially concerning the forces in the z-direction (vertical forces).

In the z direction of the rectangle wing, the mean aerodynamic force value (depicted in Table 5.3) is 0.0559 gr, similarly, for the Rufous hummingbird wing 0.0433 gr, and the Monarch butterfly wing 0.00082 gr, respectively.

The CFD simulation provides visualization of the formation and progression of vortical structures such as the Leading-Edge Vortex (LEV), Trailing-Edge Vortex (TEV), and Tip Vortex (TV).

During the downstroke, a conspicuous low-pressure region appears on the upper surface of the wing attributed to the LEV, while a relatively uniform high-pressure region forms on the lower surface due to the air's impact. At moments $t^*=t/T = 1.343$ and $t^*=t/T = 1.804$ for rectangle and Monarch butterfly wings, $t^*=t/T = 1.395$ and $t^*=t/T = 1.782$ for Rufous hummingbird wing, the principal extremum values arise primarily from the net pressure distinction between the upper and lower wing surfaces. Given the simulation's condition of zero freestream velocity, the vortical structures are solely advected by self-induction, causing them to adhere near the wing and ultimately generate a complex interference structure around the wing.

In this study, it is imperative to recognize the disparities between experimental and numerical results. Although they show close agreement, these differences could potentially be alleviated by considering more meticulous preparations for experimental conditions and different numerical models.

Table 5.3 Comparison of the rectangle, hummingbird, and Monarch wings.

	Vertical force in CFD
Rectangle	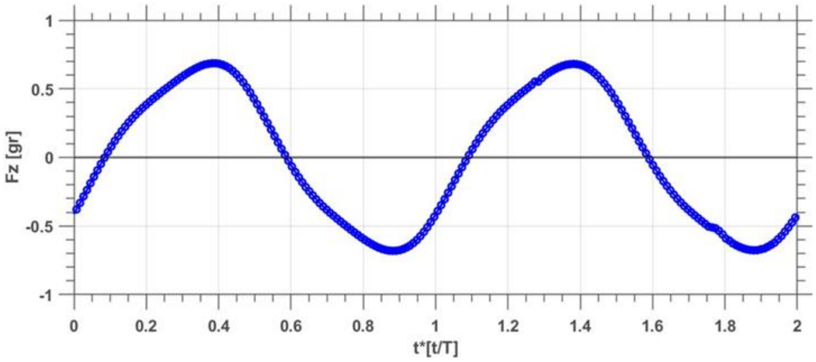
Hummingbird	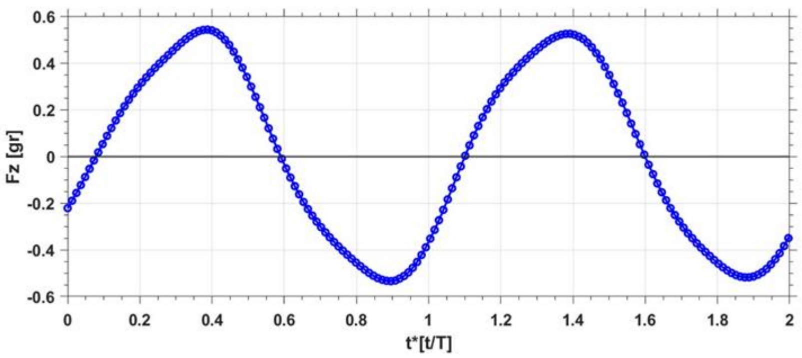
Monarch butterfly	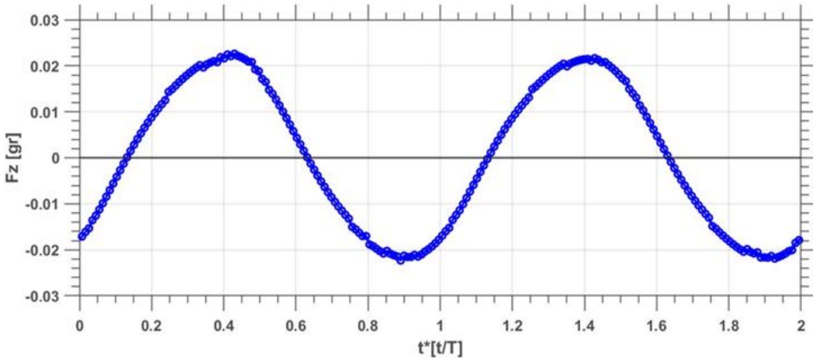

CHAPTER 6

DISSCUSION AND CONCLUSION

6.1 Objective of the Study and the Analysis Tools

This study explores the utilization of bio-inspired flapping wings for piezoelectrically actuated motion in the context of lightweight micro-air vehicle applications. The wing flexibility observed in biological flying creatures, along with their flight kinematics and the interaction of their wing structures' responses with the fluid flow around the wing, has motivated researchers to investigate the study of these creatures.

The tools employed for analyzing the phenomena encompass both numerical simulations and experimental investigations. Numerical simulations utilize a laminar code with a movable grid option. Experimental results are conducted independently using a force measurement sensor setup and Digital Image Correlation (DIC) measurements.

In this study, applying the kinematic pattern from the dynamic deformation data (from DIC) to the wing surface (in CFD) allows for the representation of the wing's deformation during flapping. Consequently, the accuracy of the inertial force calculated from the deformation under actual load conditions is expected to be better than that of other methods.

There is a scarcity of studies in the existing literature that measure the dynamic deformations of flapping wing motion triggered by piezoelectricity using Digital Image Correlation (DIC) and utilize this data as input for Computational Fluid Dynamics (CFD). In this context, this thesis represents a pioneering endeavor, offering exemplary data for future research in this field.

6.2 General Conclusion and Contribution

The purpose of this research is the investigate the unsteady aeroelastic effects on the piezoelectric actuated wings. The investigation into force generation in a bio-inspired flapping wing, referred to as one rectangle wing, one Rufous hummingbird wing, and a Monarch butterfly wing, is conducted through a combined utilization of experimental and numerical techniques. The study involved the analysis of aerodynamic and inertial forces contributing to the piezoelectrically actuated flapping wing mechanism.

At the beginning of the study, the motion generation of the piezoelectric materials (reverse piezoelectric effect) is investigated and employed to actuate the wing models. Subsequently, an experimental test setup is designed to support the piezoelectric-triggered wings for conducting both force and deformation measurements. To accurately capture the dynamic deformations in the flapping motion of the wings, Digital Image Correlation (DIC) technology is employed. In addition, to ensure accuracy in force measurements, a 6-degree-of-freedom (6-DOF) transducer, capable of high precision and able to be affixed to moving surfaces without compromising our work's robustness and size, commonly preferred in robotic studies, has been used. The following points have been obtained:

- The investigation commenced by establishing the flapping frequencies, 9.6 Hz for the piezoelectrically triggered rectangular wing and 12.1 Hz for the hummingbird wing, at which they achieved their maximum displacement.
- Simultaneously, the force values generated by the wings are measured during this acquisition. Upon analyzing these values, it is observed that wings reaching their natural frequency values also generated maximum vertical forces during their maximum wingspan motion.
- The force measurement sensor and DIC system measurements of the wings triggered at different frequencies (0-20 Hz) are conducted simultaneously. As a result, the time-dependent displacement, acceleration, wingtip velocity,

and other information about the wing reaching its natural frequency are analyzed in Chapter 5. This analysis is carried out through post-processing of the image series obtained by the DIC technique.

Obtaining the dynamic deformation of the wing through experimentation alleviates the need for a complex Fluid-Structure Interaction (FSI) model, as these dynamic deformation data are subsequently integrated into the Computational Fluid Dynamics (CFD) solver to incorporate aeroelastic effects. Furthermore, leveraging the experimental dynamic deformation data, the flexibility effect can be acted on the 3D wing in the CFD simulation.

- The vertical displacement curves obtained from the DIC system have been incorporated into the CFD model. The wings execute flapping motion under conditions of zero freestream velocity. Throughout this flapping motion, aerodynamic coefficients are derived from simulations. Specifically, the comparison of vertical aerodynamic forces is presented in Chapter 5 and summarized in Table 5.3.
- The comparative analysis between the numerical findings (CFD + Inertial) and the experimental outcomes (force sensor values) is conducted in Chapter 5. The patterns observed in the forces exhibited similarity between the experimental and numerical data. Notably, a close agreement is evident, especially concerning the forces in the z-direction (vertical forces).

The comparative analysis between experimental and numerical investigations, particularly focusing on the rectangular wing and the hummingbird wing, guided the examination of the Monarch butterfly wing, offering valuable insights into the outcomes.

- Assuming a study conducted under similar experimental conditions and employing the same piezoelectric triggering mechanism, the maximum wing tip displacement ($d_{z,max} = 0.0051\ [m]$), velocity ($v_{z,max} = 0.3018\ [m/s]$), and acceleration ($a_{z,max} = 17.7926\ [m/s^2]$) values of the Monarch butterfly wing are derived based on the DIC data of the rectangular wing. This assumes the wing is under zero pitch angle, zero free stream, and a flapping frequency set to 9.6 Hz.

- After deriving experimental data, the CFD study is similarly conducted, resulting in the acquisition of aerodynamic forces. These forces are compared with those obtained from the rectangular and hummingbird wings.

In addition to the study on the flapping motion of the Monarch butterfly, another numerical analysis has been conducted in a separate chapter (Chapter 4). This analysis involves a comprehensive examination of various angles of attack under different flow conditions. Chapter 4 specifically focuses on the static wing scenario with angles of attack ranging from 0 to 40 degrees, considering a free stream velocity of (U=5 m/s). The outcomes are presented as follows:

- A single wing is used to assess the aerodynamic force predictions in the flow simulation at different angles of attack. The wing is considered a thin plate wing model. The Reynolds number is 9724. The flow computations were performed in the range of angles of attack with 2^o increment between $\alpha=0^o$ and $\alpha=10^o$, and 10^o increment between $\alpha=10^o$ and $\alpha=40^o$.
- Unsteady numerical results for all cases were obtained using ANSYS Fluent solver, and both laminar simulations and Transition SST 4-equations turbulence-transition model were used for the analysis. It is observed that laminar and turbulent flow models have a significant difference at high angles of attack.
- The C_p and C_f distribution at spanwise locations of a Monarch wing shows the effects of the leading-edge vortex, and tip vortex at different angles of attack. Maximum C_L/C_D is obtained at $\alpha=30^o$ among the angles of attack studied in the current study. However, beyond the stall angle, the separation vortex at $\alpha=40^o$ did not reattach to the wing surface, resulting in a decrease in produced lift even while drag continued to rise resulting in a poor wing performance in terms of C_L/C_D ratio.

6.3 Future remarks

The substantial contribution of this research lies in the exploration of the capabilities of piezoelectric actuators when applied to bio-inspired flapping-wing micro aerial vehicles. Furthermore, the experimental exploration of deformations achieved using piezoelectric actuators is a significant aspect of our investigation.

The existing body of literature highlights a significant gap in both experimental setups and computational fluid dynamics (CFD) studies, particularly concerning the acquisition of aeroelastic effect outcomes and force generations, specifically dynamic deformations of flapping wing motion triggered by piezoelectricity. The current literature in CFD modeling lacks a comprehensive representation of aeroelastic effects, neglecting not only curved wing shapes but also non-rigid structures. Additionally, the incorporation of Digital Image Correlation (DIC) for displacement measurements, followed by force measurements, is notably underrepresented in the present research landscape. Hence, concerning the content of the current thesis, this study provides insights into potential avenues of future research.

When considering the entire study, some recommendations for future research can be listed as follows:

- A notable challenge in our investigation lies in the limitation of introducing a pitching angle within the experimental setup. By using technology some new four-bar-like test setups might be manufactured by utilizing the piezoelectric, the amplitudes could be amplified, and pitch angle could be applied to the flapping motion. Thus, different dynamic deformations could be investigated such as both spanwise and chordwise directions by using the advantages of the digital image correlation system (DIC).
- A comparison case might be investigated for experimental study by utilizing fully computational methods namely a three-dimensional fluid-structure interaction (3D FSI) solution of the flapping motion of the wing models.

- Besides the numerical investigation, piezoelectric actuation modeling in the fluid-structure interaction model could enhance the study. The researcher may commence by employing a comparable test setup and comparing various flexible wing models. Subsequently, wing flexibility could be introduced into the system, allowing for comparisons between different flexibility values using the same selected wing model(s). This approach may provide insights into force generation and deformations associated with varying flexibility.
- The examination of inertial forces can be investigated through experiments conducted in a vacuum chamber. Specifically, a specialized vacuum chamber design can be developed for tests involving flapping motion, and corresponding experiments can be carried out.

REFERENCES

[1] Djojodihardjo, H.,2017, Numerical Modelling of Flapping Wing Kinematics and Aerodynamics, President, The Institute for the Advancement of Aerospace Science and Technology, 15419 Jakarta, Indonesia.

[2] Senda, W., Fischer, M., Jebens, K., Mugrauer, R., Nagarathinam, A., and Scharstein F., 2012, Artificial hinged-wing bird with active torsion and partially linear kinematics, in Proceeding of 28th Congress of the International Council of the Aeronautical Sciences.

[3] Holness, A.E., Bruck, H.A, and Gupta, S.K., 2018, Characterizing and modeling the enhancement of lift and payload capacity resulting from thrust augmentation in a propeller-assisted flapping wing air vehicle International Journal of Micro Air Vehicles, Vol. 10(1) 50–69.

[4] Rosen, M.H., Pivain, G. le, Sahai, R., Jafferis, N.T., and Wood, R.J., 2016, Development of a 3.2 g untethered flapping-wing platform for flight energetics and control experiments, in 2016 IEEE International Conference on Robotics and Automation (ICRA), IEEE, pp. 3227–3233

[5] Rose, C. and Fearing, R.S., 2014, Comparison of ornithopter wind tunnel force measurements with free flight, in 2014 IEEE International Conference on Robotics and Automation (ICRA), IEEE, pp. 1816–1821.

[6] Chi, X., Wang, S., Zhang, Y., Wang, X., and Guo, Q., 2018, A tailless butterfly-type ornithopter with low aspect ratio wings, in CSAA/IET International Conference on Aircraft Utility Systems.

[7] Karasek, M., Muijres, F.T., De Wagter, C., Remes, B.D.W., and de Croon G., 2018, A tailless aerial robotic flapper reveals that flies use torque coupling in rapid banked turns, Science 361,1089–1094.

[8] James, J., Iyer, V., Chukewad, Y., Gollakota, S., and Fuller, S.B., 2018, Liftoff of a 190 mg laser powered aerial vehicle: the lightest wireless robot to fly, in 2018 IEEE International Conference on Robotics and Automation (ICRA), IEEE, pp. 1–8.

[9] Ozaki, T. and Hamaguchi, K., 2018, Bioinspired flapping-wing robot with direct-driven piezoelectric actuation and its takeoff demonstration, Robot. Autom. Lett. 3. 4217–4224.

[10] Zou, Y., Zhang, W., Ke, X., Lou, X., and Zhou, S., 2017, The design, and microfabrication of a sub 100 mg insect-scale flapping-wing robot, Micro & Nano Lett. 12, 297–300.

[11] Liu, Z., Yan, X., Qi, M., Zhang, X., and Lin L., 2017, Low-voltage electromagnetic actuators for flapping-wing micro aerial vehicles, Sens. Actuators A Phys. 265, 1–9.

[12] Zou, Y., Zhang, W., and Zhang, Z., 2016, Liftoff of an electromagnetically driven insect-inspired flapping-wing robot, Trans. Robot. 32, 1285–1289.

[13] Ancel, A. O., Eastwood, R., Vogt, D., Ithier, C., Smith, M., Wood, R., and Kovacˇ, M., 2017, Aerodynamic evaluation of wing shape and wing orientation in four butterfly species using numerical simulations and a low-speed wind tunnel, and its implications for the design of flying micro-robots. Interface Focus7:20160087 http://dx.doi.org/10.1098/rsfs.2016.0087.

[14] Aaroh, Zuber M, Md Abdul Khader S, Kalburgi S, Basri EI, Ahmad KA, 2018, Performance of a Monarch Butterfly for Various Flapping Angle, International Journal of Engineering & Technology, 7 (4.25) (2018) 126-130.

[15] Kurtulus, D.F., 2018, Aerodynamic loads of small amplitude pitching NACA 0012 airfoil at Reynolds Number of 1000, AIAA Journal, Vol. 56, No. 8, pp. 3328-3331.

[16] Satapanapituggit, N., Verojporn, K., Tin, D., Chan, L.Y.,and Srigrarom. S.,2015, Flow Field of Flapping Monarch and Swallowtail Butterfly-like Wings. The Journal of Unmanned System Technology Vol. 3, Issue 1, pp. 6-15.

[17] https://en.wikipedia.org/wiki/Lepidoptera (Avaible date : 25.06.2020)

[18] Betts, C.R. and Wootton, R.J., 1988, Wing Shape and Flight Behavior in Butterflies (Lepidoptera: Papilionoidea and Hesperioidea): A Preliminary Analysis, J. exp. Biol. 138, 271-288 (1988).

[19] Park H., Bae K., Lee B., Jeon W-P, and Choi H., 2010, Aerodynamic performance of a gliding swallowtail butterfly wing model. Exp. Mech. 50, 1313–1321.

[20] Dudley, R., 2002, The biomechanics of insect flight: form, function, evolution. Princeton, NJ: Princeton University Press.

[21] Twigg, R., Sridhar, M.K., Pohly, J., Hildebrant, N., Kang, C., Landrum, D. B., Roh, K.H., 2020, Aeroelastic Characterization of Real and Artificial Monarch Butterfly Wings, American Institute of Aeronautics and Astronautics, Inc., AIAA SciTech Forum, 6-10 January 2020, Orlando, FL, 10.2514/6.2020-2002

[22] Senda K., Obara T., Kitamura M., Yokoyama N., Hirai N. and Iima M., 2012, Effects of structural flexibility of wings in the flapping flight of the butterfly, IOP Publishing Bioinspiration & Biomimetics, Bioinspir. Biomim. 7, 025002 (15pp) doi:10.1088/1748-3182/7/2/025002.

[23] Truong T.V., Nguyen Q.V, and Lee H.P., 2017, Bio-Inspired Flexible Flapping Wings with Elastic Deformation Aerospace, 4, 37; doi:10.3390/aerospace4030037.

[24] Nguyen A.T., Han J.H., 2018, Wing flexibility effects on the flight performance of an insect-like flapping-wing micro-air vehicle, Aerospace Science and Technology 79, 468–481.

[25] Yang W., Song B., Wang L., and Chen L., 2015, Dynamic Fluid-Structure Coupling Method of Flexible Flapping Wing for MAV, J. Aerosp. Eng., 28(6): 04015006, DOI: 10.1061/(ASCE)AS.1943-5525.0000490.

[26] Brower, L.P., 2003, Monarchs. Encyclopedia of Insects, Elsevier, pp. 739–743.

[27] Shyy, W., Aono, H., Kang, C., and Liu, H., 2013, An introduction to flapping wing aerodynamics. New York: Cambridge University Press.

[28] Combes, S.A. 2003, Flexural Stiffness in Insect Wings I. calling and the Influence of Wing Venation. Journal of Experimental Biology, Vol. 206, 17, pp. 2979–2987.

[29] Shyy, W., Aono, H., Chimakurthi, S.K., Trizila, P., Kang, C.K., Cesnik, C.E.S., Liu, H., 2010, Recent Progress in Flapping Wing Aerodynamics and Aeroelasticity. Progress in Aerospace Sciences, Vol. 46, Nr. 7 pp. 284–327.

[30] Twigg, R., Sridhar, M.K, Pohly, J., Hildebrant, N., Kang, C., Landrum, D.B., Roh, K.H., and Salzwedel, S., 2020, Aeroelastic Characterization of Real and Artificial Monarch Butterfly Wings, 6-10 January 2020, Orlando, FL 10.2514/6.2020-2002 AIAA SciTech 2020 Forum.

[31] Sridhar, M.K., Kang, C.K., and Landrum, D.B., 2020, Fluid-structure Interaction of Flexible Flapping Wings at High Altitude Conditions at Monarch Butterfly Scale. AIAA SciTech 2020 Forum, 10.2514/6.2020-1781.

[32] Ludwick, D., 2021, Monarch Butterfly, Extension Entomology, Texas A&M AgriLife Extension Service.

[33] Chu, Y.-J. and. Liew, H.-L,2021, Aerodynamics of a wing under figure-of-eight flapping motion: FSI simulations, The Aeronautical Journal, Published by

Cambridge University Press on behalf of Royal Aeronautical Society, pp.1-25, doi:10.1017/aer.2021.35.

[34] Stiles, F.G., Altshuler, D. L., Dudley, R., 2005, Wing Morphology and Flight Behavior of Some North American Hummingbird Species, The American Ornithologists' Union.

[35] ASTM, Designation: E8/E8M – 09, Standard Test Methods for Tension Testing of Metallic Materials, http://www.astm.org/Standards/E8.htm, [Online][Cited: March 2016].

[36] PICMA, Piezo Bender Actuators Multilayer Bending Actuators with Large Displacement, Physik Instrumente (PI). [Online] [Cited: December 2023.] https://www.physikinstrumente.com/en/products/piezoelectric-transducers-actuators/bender-actuators.

[37] ATI Industrial Automation [Online] [Cited: December 2023.] https://www.ati-ia.com/products/ft/ft_models.aspx?id=Nano17.

[38] ARAMIS v6.3, Use Manual, Software and Hardware, aramis-v6-3_1st_en_rev-a, 5 May,2011.

[39] Senda, K., Sawamoto, M., Shibahara, T., and Tanaka, T. (2004) Study on flapping-of-wings flight of butterfly with experimental measurement, AIAA paper no. 2004-5368.

[40] Altizer, S., and Davis, A.K., 2009, Populations of Monarch Butterflies with Different Migratory Behaviors Show Divergence in Wing Morphology, doi:10.1111/j.1558-5646.2009. 00946.x

[41] Winslow, J., Otsuka, H., Govindarajan, B., and Chopra, I., 2018, Basic Understanding of Airfoil Characteristics at Low Reynolds Numbers (104–105). Journal of Aircraft Vol. 55, No. 3.

[42] Dickinson, M.H., Lehmann, F.O., and Sane, S.P., 1999., Wing rotational and aerodynamic basis of insect flight. Science 284(5422): 1954–1960.

[43] Ellington, C.P., van den Berg, C., Willmott, A.P., Thomas, A.L.R., 1996, Leading-edge vortices in insect flight. Nature, Vol. 384. 19/26 pp.626- 630.

[44] Ellington, C.P., 1999, The Novel Aerodynamics of Insect Flight: Applications to Micro-air Vehicles. Nature, The Journal of Experimental Biology 202, pp. 3439–3448.

[45] Gibo, D.L., 1986, Flight Strategies of Migrating Monarch Butterflies (Danaus Plexippus L.) in Southern Ontario. Insect Flight, Berlin: Springer.

[46] White, Frank M., Fluid Mechanics, 8th Edition, Published by McGraw-Hill Education, 2 Penn Plaza, New York, NY 10121. Copyright © 2016 by McGraw-Hill Education.

[47] Hunt, J. C. R., Wray, A. A., Moin, P., "Eddies, stream, and convergence zones in turbulent flows," Report CTR-S88, Center for Turbulence Research, 1988.

[48] Lee, H.K., Jang, J.W., Wang, J.Y, Son, Y.W., and Lee S.H., 2019, Comparison of cicada hindwings with hindwing-less drosophila for flapping motion at low Reynolds number, Journal of Fluids and Structures 87, 1–22.

[49] Agarwal, A., Nolan, K.P., Stafford, J., and Jeffers N., 2017, Visualization of three-dimensional structures shed by an oscillating beam, Journal of Fluids and Structures 70, 450–463.

[50] Helbling, E.F. and Wood, R.J., 2018, A Review of Propulsion, Power, and Control Architectures for Insect-Scale Flapping-Wing Vehicles, Applied Mechanics Reviews by ASME, Vol. 70 / 010801-1.

[51] Piezo Electric Parallel Bimorph Actuator-SMBA4510T05M STEMINC. [Online] [Cited: April 2015.] http://steminc.com/piezo/SMBA4510T05M.asp.

[52] Naeem, N., Fouda, M., Guney, M., Kurtulus, D. F.,2023, Wake patterns and mode switching at low Reynolds numbers, Progress in Computational Fluid

Dynamics, An International Journal, Vol. 23, No.2, pp.87-110. https://doi.org/10.1504/PCFD.2023.129762.

[53] Kurtulus, D.F., 2022, Critical Angle and Fundamental Frequency of Symmetric Airfoils at Low Reynolds Numbers, Journal of Applied Fluid Mechanics, Volume 15, Number 3, May 2022, pp.723-735, 10.47176/JAFM.15.03.33099.

[54] Kurtulus, D. F., 2021, Vortex flow aerodynamics behind a symmetric airfoil at low angles of attack and Reynolds Numbers, International Journal of Micro Air Vehicles, doi 10.1177/17568293211055653, Volume 13: 1–18.

[55] Gunaydinoglu, E., Kurtulus, D.F.,2020, Pressure–velocity coupling algorithm-based pressure reconstruction from PIV for laminar flows, Experiments in Fluids, 61: 5, https://doi.org/10.1007/s00348-019-2831-1.

[56] Durmaz, O., Karaca, H.D., Ozen, G.D., Kasnakoglu, C., Kurtulus, D.F., 2013, Dynamical Modeling of the Flow over a Flapping Wing using Proper Orthogonal Decomposition and System Identification Techniques, Mathematical and Computer Modelling of Dynamical Systems, Volume 19, Issue 2, pp.133-158.

[57] Kurtulus, D.F., Farcy, A., Alemdaroglu N., 2004, Numerical Calculation and Analytical Modelization of Flapping Motion. Proceeding of 1st European Micro Air Vehicle Conference and Flight Competition. Braunschweig, Germany, 13-14 July 2004.

[58] Kurtulus, D.F., Farcy, A., Alemdaroglu, N.,2005, Unsteady Aerodynamics of Flapping Airfoil in Hovering Flight at Low Reynolds Numbers. AIAA-2005-1356, 43rd AIAA Aerospace Sciences Meeting and Exhibit, Reno, Nevada, USA, 10 - 13 Jan 2005.

[59] Kurtulus D.F., David L, Farcy, A., Alemdaroglu, N.,2006a, A Parametrical Study with Laser Sheet Visualization for an Unsteady Flapping Motion. AIAA-2006-3917, 36th AIAA Fluid Dynamics Conference and Exhibit, San Francisco, California USA, 5 - 8 June 2006.

[60] Kurtulus, D. F., David, L., Farcy, A., Alemdaroglu, N., 2006b, Laser Sheet Visualization for Flapping Motion in Hover. AIAA-2006-0254, 44th AIAA Aerospace Sciences Meeting and Exhibit, Reno, Nevada, USA, 9 - 12 Jan 2006.

[61] Senol, G., Arıkan, K.B., Kurtulus D.F., 2017, Experimental and Numerical Results of a Flapping Wing Four Bar Mechanism, 55th AIAA Aerospace Sciences Meeting, AIAA SciTech Forum, AIAA 2017-0498, 9-13 January 2017.

[62] Beker, C., Turgut, A. E., Ozcan, O., Arikan, K. B. and Kurtulus, D. F., 2017, Design of a Novel Foldable Flapping Wing Micro Air Vehicle, AIAC-2017-138, Ankara International Aerospace Conference, 20-22 September 2017, Ankara.

[63] Anılır, B., Kurtulus, D.F. and Platzer, M.F., 2023, Flow Control by Oscillating Trailing-Edge Flaps, AIAA Journal, Vol. 61, No.9, pp.4210-4213.

[64]Yang, X., Song, B., Yang, W., Xue, D., Pei, Y., Lang, X.,2022, Study of aerodynamic and inertial forces of a dovelike flapping-wing MAV by combining experimental and numerical methods, Chinese Journal of Aeronautics, (2022), 35(6): 63–76.

[65] Dong, Y., Song,B., Xue,D., Li,Y.,Yang,W.,2022, Numerical Study of the Aerodynamics of a Hovering Hummingbird’s Wing with Dynamic Morphing, International Journal of Aerospace Engineering, Volume 2022, Article ID 5433184, https://doi.org/10.1155/2022/5433184.

APPENDICES

A. Piezoelectric Actuators Used for Flapping Motion

1. STEMINC - Piezo, Piezoelectric

Table A. 1 Physical properties of the piezoelectric actuator [51].

Piezo Ceramic Bimorph	
Piezo Material	SM311
Dimensions	45* ×10 × 0.5 mm
Resonant frequency (fr*)	2 KHz ± 5%
Maximum Deflection (δ*)	2 mm (min)
Maximum Input Voltage	100 Vpp
Resonant Mode	Deflection
Test Condition	25 ± 2 °C
(δ*) Mounted as a cantilever beam, measured at voltage 100Vpp	
(fr*) Mounted as a cantilever beam, measured by impedance analyze	
*Total length with 40mm ceramic layer length	

Table A. 2 Piezo Ceramic Bimorph Material Properties [51].

Property	**Unit**	**Symbol**	**SM311**
Electromechanical coupling coefficient		K_p	0.65
		K_t	0.37
		K_{31}	0.38
Frequency constant	Hz. m	N_p	1980
		N_t	1950
		N_{31}	1450
Piezoelectric constant	$\times10^{-12}$m/v	d_{33}	600
		d_{31}	-270
	$\times10^{-3}$Vm/N	g_{33}	19.4
		g_{31}	-9.2
Elastic Constant	$\times10^{10}$N/m^2	Y_{33}	5.3
		Y_{11}	7.2
Mechanical Quality Factor	-----	Q_m	80
Dielectric Constant	@1KHz	$\varepsilon T_{33/\varepsilon 0}$	3500
Dissipation Factor	%@1KHz	tan δ	2.5
Temperature	°C	T_c	220
Density	g/cm^3	ρ	7.8

2. PI (Physik Instrumente) PL140 PICMA Bender

Table A. 3 Physical properties of PL140 PICMA Bender [36].

PL140.10	
Piezo ceramic type	PIC 251
Operating Voltage	30 V_{pp}
Displacement	± 1000 µm
Free Length	40 mm
Dimensions	45 ±0.5 ×11 ±0.2×0.55 ±0.1 mm
Blocking force	±0.5 N
Resonant frequency	160 Hz
Operating temperature	-20ºC to 85ºC

Table A. 4 PIC-252/255 Piezo Ceramic Material Properties [36].

Properties	Unit	Symbol	PIC255/PIC2521)
Electromechanical properties			
Coupling factor		k_p	0.62
		k_t	0.47
		k_{31}	0.35
		k_{33}	0.69
		k_{15}	0.66
Piezoelectric charge coefficient	10^{-12} C/N	d_{31}	-180
		d_{15}	400
		d_{33}	550
Piezoelectric voltage coefficient	10^{-3}Vm/N	g_{31}	-11.3
		g_{33}	25
Mechanical properties			
Elastic compliance coefficient	$10^{-12}m^2/N$	S_{11}^E	16.1
		S_{33}^E	20.7
Relative permittivity		C_ε	1.0
Coupling factor		C_K	-1.0
Relative permittivity in the polarization direction		$\varepsilon_{33}T/\varepsilon_0$	1750
Density	g /cm^3	ρ	7.80

3. Piezoelectric Ceramic Electro-Mechanical Relations

s : matrix 6x6 m^2/N: Compliance matrix

c: matrix 6x6 N/m^2: Stiffness coefficients

ε: matrix 3x3 F/m: electric permittivity

d: matrix: 3x6 C/N: piezoelectric coupling coefficients for Strain-Charge form

e: matrix 3x6 C/ m^2: piezoelectric coupling coefficients for Stress-Charge form

[c] is the stiffness matrix calculated previously.

To calculate [e], we need to use the relation [e] = [d]. [c]

$$c_E = s_E^{-1}$$

$$e = d.\,s_E^{-1}$$

$$\varepsilon_S = \varepsilon_T - d.\,s_E^{-1}.\,d^t$$

Linear piezoelectricity is the combined effect of electrical and elastic mechanical behavior. Those behaviors are defined by the following two laws.

- The linear electrical behavior of the material
- Hooke’s law for elastic materials

These relations may be combined into so-called coupled equations, of which the strain-charge form is:

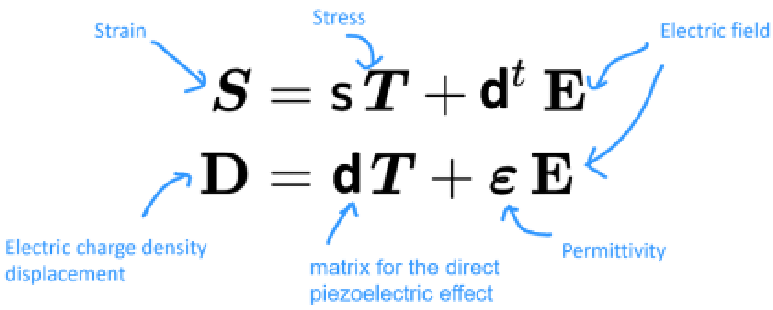

$$\begin{bmatrix} S_1 \\ S_2 \\ S_3 \\ S_4 \\ S_5 \\ S_6 \end{bmatrix} = \begin{bmatrix} s_{11}{}^E & s_{12}{}^E & s_{13}{}^E & 0 & 0 & 0 \\ s_{21}{}^E & s_{22}{}^E & s_{23}{}^E & 0 & 0 & 0 \\ s_{31}{}^E & s_{32}{}^E & s_{33}{}^E & 0 & 0 & 0 \\ 0 & 0 & 0 & s_{44}{}^E & 0 & 0 \\ 0 & 0 & 0 & 0 & s_{55}{}^E & 0 \\ 0 & 0 & 0 & 0 & 0 & s_{66}{}^E \end{bmatrix} \begin{bmatrix} T_1 \\ T_2 \\ T_3 \\ T_4 \\ T_5 \\ T_6 \end{bmatrix} + \begin{bmatrix} 0 & 0 & d_{31} \\ 0 & 0 & d_{32} \\ 0 & 0 & d_{33} \\ 0 & d_{24} & 0 \\ d_{15} & 0 & 0 \\ 0 & 0 & 0 \end{bmatrix} \begin{bmatrix} E_1 \\ E_2 \\ E_3 \end{bmatrix}$$

Where $s_{66}{}^E = 2(s_{11}{}^E - s_{12}{}^E)$

$$\begin{bmatrix} D_1 \\ D_2 \\ D_3 \end{bmatrix} = \begin{bmatrix} 0 & 0 & 0 & 0 & d_{15} & 0 \\ 0 & 0 & 0 & d_{24} & 0 & 0 \\ d_{31} & d_{32} & d_{33} & 0 & 0 & 0 \end{bmatrix} \begin{bmatrix} T_1 \\ T_2 \\ T_3 \\ T_4 \\ T_5 \\ T_6 \end{bmatrix} + \begin{bmatrix} \varepsilon_{11} & 0 & 0 \\ 0 & \varepsilon_{22} & 0 \\ 0 & 0 & \varepsilon_{33} \end{bmatrix} \begin{bmatrix} E_1 \\ E_2 \\ E_3 \end{bmatrix}$$

B. Force/Torque Sensors for Measurements

1. Nano17 IP68 Force Sensor

a) b)

Figure B. 1 a) Nano17 IP68 Force Sensor, b) NANO17 Transducer with Axial Cable and IP68 Protection (3D CAD model e-drawing from ATI web site [36])

Table B. 1 Metric Calibration table (SI) [37].

Calibration	**Fx, Fy**	**Fz**	**Tx, Ty**	**Tz**	**Fx, Fy**	**Fz**	**Tx, Ty**	**Tz**
SI-12-0.12	12 N	17 N	120 Nmm	120 Nmm	1/160 N	1/160 N	1/32 Nmm	1/32 Nmm
	SENSING RANGES				RESOLUTION			

2. Nano17-E Transducer

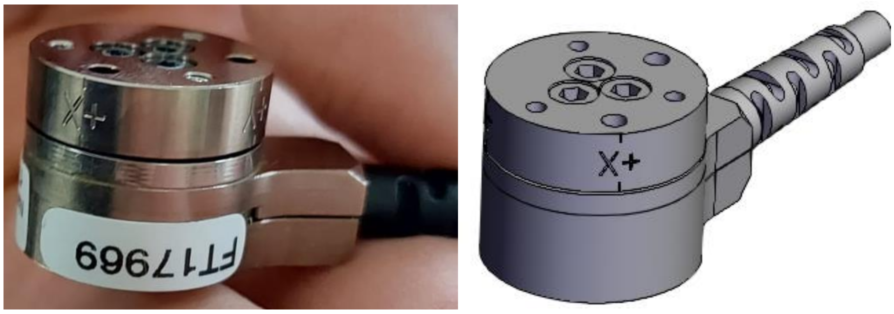

a) b)

Figure B. 2 a) Nano17-E Transducer, b) NANO17-E Transducer with Strain Relieved Cable (3D CAD model e-drawing from ATI web site [36]).

Table B. 2 Calibration [37]

Calibration	**Fx, Fy**	**Fz**	**Tx, Ty**	**Tz**	**Fx, Fy**	**Fz**	**Tx, Ty**	**Tz**
SI-12-0.12	12 N	17 N	120 Nmm	120 Nmm	1/320 N	1/320 N	1/64 Nmm	1/64 Nmm
	SENSING RANGES				RESOLUTION			

C. UDF File for dynamic mesh motion in CFD study

```
/**********************************************************
        deflection equation compiled UDF
**********************************************************/
#include "udf. h"
DEFINE_GRID_MOTION ((wing, domain, dt, time, dtime)
{
Thread *tf = DT_THREAD (dt);
face_t f;
Node *v;
real NV_VEC (disp), NV_VEC(axis), NV_VEC(dx);
real NV_VEC (origin), NV_VEC(rvec);
real sign;
int n;
SET_DEFORMING_THREAD_FLAG(THREAD_T0(tf));
sign = 0.1015*2*3.1416*(9.6) *cos (2*3.1416*(9.6) *time);
NV_S (disp, =, 0.0);
NV_D (axis, =, 0.0, 1.0, 0.0);
NV_D (origin, =, 0.0, 0.0, 0.0);
begin_f_loop(f,tf)
{
f_node_loop(f,tf,n)
{
v = F_NODE(f,tf,n);
if (NODE_X(v) > 0.0 && NODE_POS_NEED_UPDATE (v))
{
NODE_POS_UPDATED(v);
disp[1] = sign * (pow(NODE_X(v)/0.117, 0.5));
NV_VV (rvec, =, NODE_COORD(v), -, origin);
NV_CROSS (dx, disp, rvec);
NV_S (dx, *=, dtime);
NV_V(NODE_COORD(v), +=, dx);
}
}
}
end_f_loop(f,tf);
}
```

D. C_p comparison for flapping wings

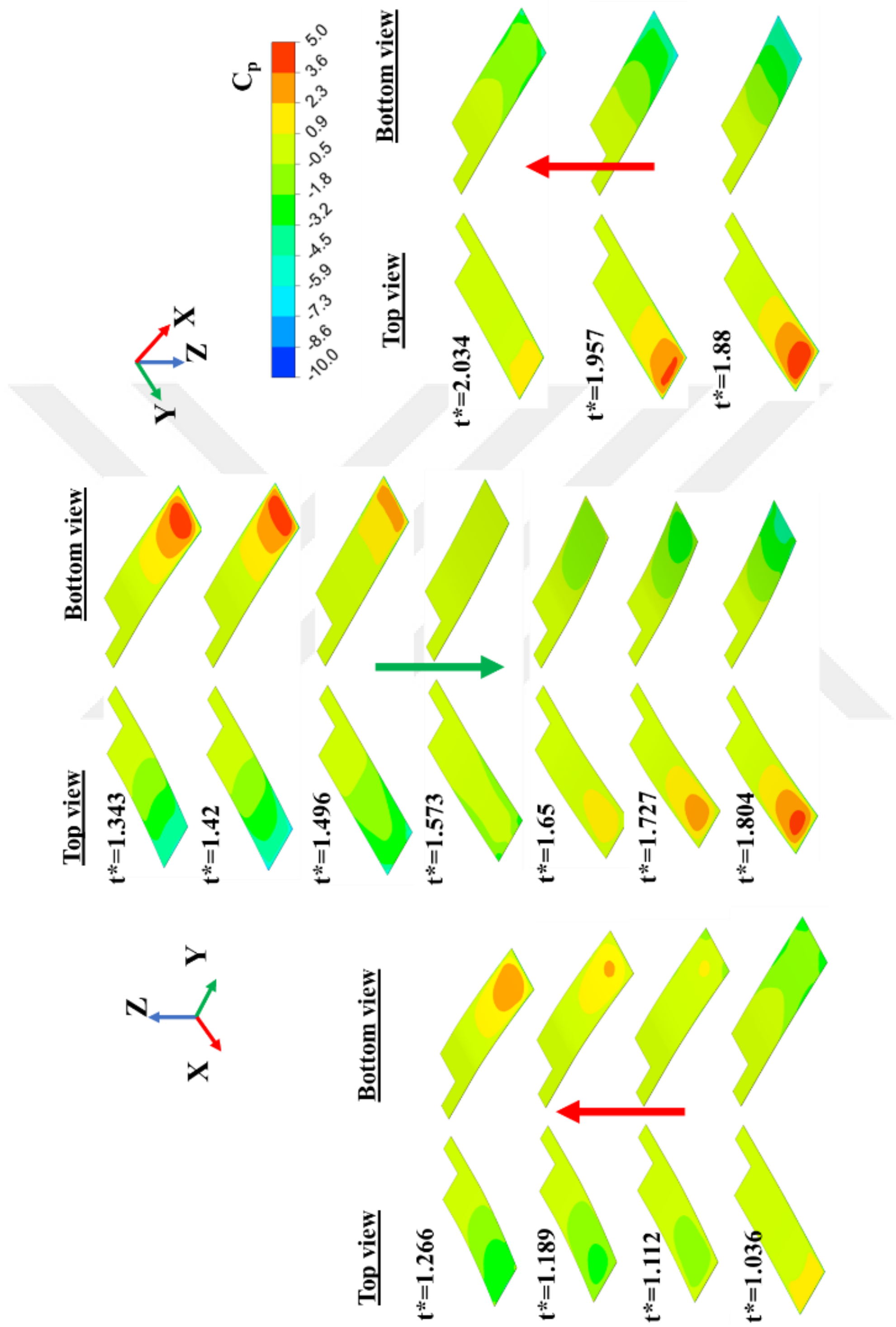

a)

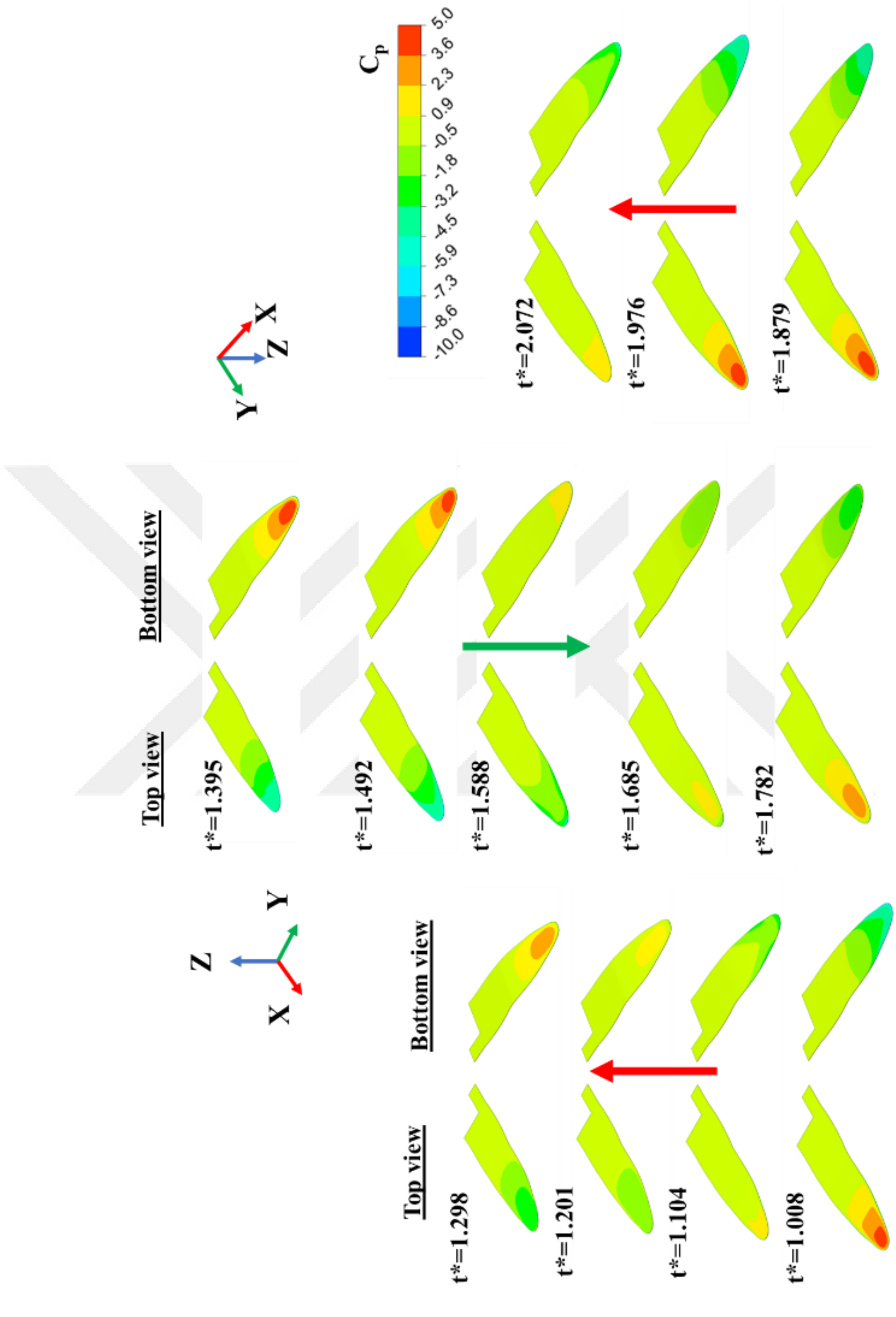
Top view
Bottom view
t*=1.298
t*=1.201
t*=1.104
t*=1.008
t*=1.395
t*=1.492
t*=1.588
t*=1.685
t*=1.782
t*=2.072
t*=1.976
t*=1.879
X
Y
Z
C
5.0
3.6
2.3
0.9
-0.5
-1.8
-3.2
-4.5
-5.9
-7.3
-8.6
-10.0

b)

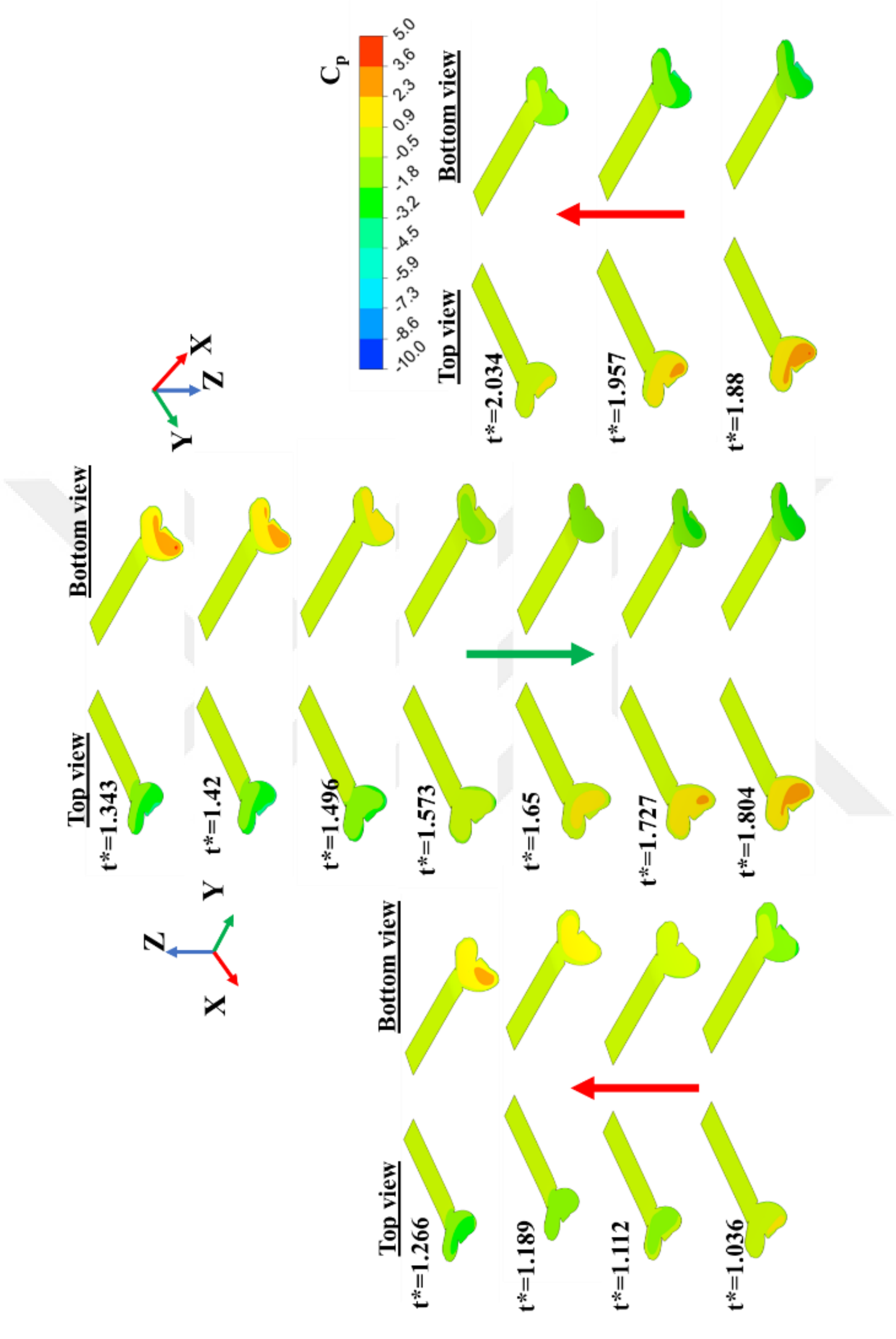

c)

Figure D. 1 Cp comparison for a) Rectangle wing, b) Rufous hummingbird wing, and c) Monarch butterfly wing

CURRICULUM VITAE

PERSONAL INFORMATION

Surname, Name: Çömez Özgün, Fadile Yudum

EDUCATION

Degree	Institution	Year of Graduation
MS	THK University Aeronautical and Mechanical Engineering	2015
BS	Gazi University Mathematics Department	2011
High School	Gölbaşı Anadolu Lisesi, Ankara	2006

WORK EXPERIENCE

Year	Place	Enrollment
2022- present	RUZGEM	Scientific Project Researcher
2021- 2022	TUSAS	Design Engineer
2015- 2018	METU Dept. of Aerospace Eng.	Research Assistant

FOREIGN LANGUAGES

Advanced English

PUBLICATIONS

1. Comez, F.Y., Sengil, N., Kurtulus, D.F., 2023," Three-dimensional Flow Evaluation of Monarch Butterfly Wing", *Progress in Computational Fluid Dynamics, An International Journal*, DOI: 10.1504/PCFD.2023.10058561.

2. Sengil, N., Comez, F.Y., 2019," Application of D2Q5 Pressure Boundary Conditions for Parallel D2Q9 Lattice Boltzmann Method", 31st International Conference on Parallel Computational Fluid Dynamics, ParCFD'2019, May 14-17, 2019, Antalya TURKEY.

3. Comez, F.Y., Kurtulus, D.F., 2018," Effect of Forward Velocity on Rectangular Wings Flapping with Piezoelectric Actuators", ISSA- 2018-20, *International Symposium on Sustainable Aviation 2018*, Rome, Italy, 9-11 July 2018.

4. Sengil, N., Comez, F.Y., 2018," Application of Mass Fluxes for Pressure Boundary Conditions in Lattice Boltzmann Method", *The International Conference on Materials Science, Mechanical and Automotive Engineering and Technology*.

5. Comez, F.Y., Kurtulus, D.F., 2016," Piezoelektrik Eyleyici ile Tetiklenen Güve Böceği Kanadın Aerodinamik Kuvvet Deneysel Olarak Karşılaştırılması", *VI. ULUSAL HAVACILIK VE UZAY KONFERANSI*, Kocaeli Üniversitesi, Kocaeli.

6. Comez, F.Y., Sengil, N., 2016," Channel and Cavity Flow Analysis Using Lattice Boltzmann Solvers Parallelized with Coarray Fortran", *9th International Conference on Computational Fluid Dynamics*.

7. Comez, F.Y., Senol, M.G., Kurtulus, D.F., 2015," Unsteady Aerodynamic Analysis of a Flapping Wing Actuated with PZT Material", *Workshop on Non-Intrusive Measurements for unsteady flows and aerodynamics*, Poitiers, FRANCE.

8. Senol, M.G., Comez, F.Y., Kurtulus, D.F., 2015," Testing of Flapping Wing Four-Bar Mechanis", *Workshop on Non-Intrusive Measurements for unsteady flows and aerodynamics*, Poitiers, FRANCE.